Preprint of

"Effect of chemical disequilibrium during metal-silicate partitioning on the thermal state of the early core".

By Vincent Clesi and Renaud Deguen

This article has been submitted to Advances in Geochemistry and Cosmochemistry.

This version of the text is the version after the first round of reviews, but before acceptance for publication.

Included in this pdf: main text, with the links to code and supplementary material.

Effect of chemical disequilibrium during metal-silicate partitioning on the thermal state of the early core

Vincent Clesi[1,2]✉ Renaud Deguen[2,3]

[1] Insitut für Mineralogie, Münster Universität, Corrensstraße 24, 48149 Münster
[2] Univ Lyon, ENSL, UCBL, UJM, CNRS, LGL-TPE, F-69007 Lyon, France
[3] Univ. Grenoble Alpes, Univ. Savoie Mont Blanc, CNRS, IRD, Univ. Gustave Eiffel, ISTerre, 38000 Grenoble, France

Author contributions: Conceptualization: VC, RD. Methodology: VC. Investigation: VC. Data Curation: VC. Formal analysis: VC. Validation: VC, RD. Writing – original draft: VC. Writing – review & editing: VC, RD.

Supplementary material: https://doi.org/10.5281/zenodo.21771983

Abstract

In this study, we improved a previously published numerical model linking the core composition to the core temperature during accretion by introducing the possibility of chemical disequilibrium during the segregation of the core in the magma ocean phase. Our study shows that at least 60% of the accreting metal needs to be equilibrated in order to obtain a chemically coherent Earth, thus favoring a rapid core formation according to the Hf-W chronometer. The dilution factor of this equilibrated metallic mass needs to be 4 (for 100% of metallic mass equilibrated) to 40 (for 60% of the metallic mass equilibrated) in order to obtain concentrations of major and trace element close to the Bulk Silicate Earth composition. At the minimum degree of equilibrium in metal and silicate phases, the final temperature of the core is increased by a maximum $\sim 250 \pm 40$ K , with an average of $50 - 100 \pm 5K$ compared to the fully equilibrated case (with $T^{is}_{CMB} \sim 3800 \pm 250K$). The chemical disequilibrium could be then one factor favoring the hot core hypothesis, but has to be coupled with other phenomena (gravitational energy dissipation, radiogenic heat production) to produce a hot core.

1 Introduction

The presence of light elements in the core has been demonstrated for a long time (Birch, 1965), and constraining the nature and concentrations of these light elements is important to understand the so-called core density deficit (Dziewonski and Anderson, 1981). The incorporation of light elements in the core has been proposed to happen in a deep magma ocean, where the core-forming metal segregates from the silicate (e.g. Drake and Righter, 2002; Bouhifd and Jephcoat, 2011). This formation at high pressure and high temperature (maximum pressure between 54 and 80 GPa, maximum temperature between 3400 and 4000 GPa Bouhifd and Jephcoat, 2011; Fischer et al., 2015; Rubie et al., 2015) favors the incorporation of light elements in the core, the main light elements being Si and O (Rubie et al., 2015; Fischer et al., 2017; Clesi and Deguen, 2023; Pu et al., 2025). The final composition of the core, and in particular the concentrations of light elements, is dependent on several factors, the main factors being the composition of the building blocks of the Earth and the P-T-f_{O_2} conditions of metal-silicate segregation in a deep magma ocean. Among those conditions, the efficiency of mixing in the magma ocean and the degree of chemical equilibrium is often overlooked, with a majority of models focusing on the end-member with full equilibrium (e.g. Wood et al., 2008; Siebert et al., 2012; Fischer et al., 2015, 2017; Clesi et al., 2016; Clesi and Deguen, 2023; Loroch et al., 2024; Pu et al., 2025). The effect of disequilibrium is complex to apprehend, as two phases are involved (e.g. Rubie et al., 2003; Ulvrová et al., 2011; Gu et al., 2023) with dynamic separation of the two phases that are complex to model (e.g. Samuel, 2012; Deguen et al., 2014; Landeau et al., 2021) with elemental specific equilibrium rates (Clesi et al., 2020). In a previous work (Clesi and Deguen, 2023), we used an accretion model combining the metal-silicate partitioning behavior of different elements and a thermal evolution model of the metallic phase, dependent on the metallic phase composition, to link the thermal evolution of the core to its composition. This model tends to favor the cold core hypothesis, with temperatures ranging from 3500±200 K (Nomura et al.,

2014; Dobrosavljevic et al., 2022) to 4000±200 K (Zhang et al., 2016), particularly if the amount of gravitational dissipation energy going to the metal is low (Monteux et al., 2009; Samuel et al., 2010). The hot core hypothesis ($T_{CMB} \sim 5000 - 6000K$ King and Olson, 2011; Andrault et al., 2017; Driscoll and Davies, 2023), to be true, necessitates other mechanisms than the simple compressional heating used in Clesi and Deguen (2023). One factor that could increase the initial core temperature is the chemical disequilibrium during the metal-silicate segregation process. Indeed, to explain the bulk silicate Earth composition while considering chemical disequilibrium during core mantle segregation, it is necessary to increase the average depth of the magma ocean (going from a maximum extent of $\sim$ 1300-1800 km to depths above 2000 km and up to the CMB Rubie et al., 2003, 2011; Gu et al., 2023). Clesi and Deguen (2023) showed that such an increase in average magma ocean depth translates into higher core temperatures as well as higher concentrations of Si and O. Therefore, in this study, we modify the model of Clesi and Deguen (2023) by introducing various degrees of disequilibrium in the metallic and silicate phase during the accretion process. We used the results to quantify the effect of chemical disequilibrium on the initial core temperature. We showed that a minimum 60% of the metallic phase needs to be equilibrated with the silicate; and that introducing some degree of disequilibrium favors the formation of a hotter core at the end of accretion, but not hot enough to comply with the 'hot core' hypothesis.

2 Description of the thermal model

To determine the heat content and temperature of the core we consider the following steps :

(i) The initial temperature of each addition of metal to the core is set at the bottom of the magma ocean, where the metal is assumed to equillibrate with the silicates. The initial temperature is therefore given by the liquidus of silicate at the pressure of the bottom of the magma ocean, as given by Andrault et al. (2011). The metal

composition is an alloy of Fe-Ni-Co-Si-O-V-Cr whose composition is determined by the chemical equilibrium, see section 3.

(ii) The chemically equilibrated metal is then heated by compression while migrating from the bottom of the magma ocean to the growing core, without changing its composition for a given step of accretion. At each step of accretion its composition is different, and we do not consider any mixing of the core, thus resulting in the formation of a stratified core (as in Jacobson et al. (2017)).

(iii) This metal is further heated by compression due to the growth of the core up to its final size. We use the resulting temperature and density profiles to calculate the heat content of the core.

(iv) We assume that the core is then mixed from the stratified state, and use the previously calculated heat content to get the temperature at the CMB (T^{is}_{CMB}) assuming the core to be isentropic. That the core is mixed at the end of accretion is a somewhat strong assumption (Jacobson et al., 2017), but it has the advantage of allowing to quantify the thermal state of the core with a single parameter (here the CMB temperature), which greatly simplifies the analysis.

The details on the model and the different calculations are described in Clesi and Deguen (2023), but we propose a quick description of the thermal model in the following paragraphs.

The initial temperature of the metal is set to be the liquidus temperature of the silicate from Andrault et al. (2011) at the bottom of the magma ocean where the chemical equilibrium happens. It is given by:

$$T_{eq} = 1940 \pm 70 \left(\frac{P_{eq}}{29 \pm 5} + 1 \right)^{\frac{1}{1.9 \pm 0.14}}, \quad (1)$$

where P_{eq} and T_{eq} are the equilibrium pressure and temperature at the base of the magma ocean, with the error on the parameter written in the equation. This equation is widely used in models of accretion, notably Fischer et al. (2015) from which we took the chemical parametarization, and also the initial study of Clesi and Deguen

(2023). To facilitate the comparisons, we will keep using this equation for the liquidus of silicate, as it is tailored for chondritic compositions that are used in this study. It is important to note that using Fiquet et al. (2010) liquidus curve for peridotitic composition would increase the final temperatures (see Supplementary material, section S.1). The number of solution is roughly the same, as the partitioning behavior of the elements chosen in this study are not very sensitive to pressure (Geßmann and Rubie, 1998). The temperature changes in steps (ii) and (iii) are obtained from:

$$\frac{dT}{T} = \frac{\gamma}{K_s} dP, \tag{2}$$

where γ and K_s are the Gruneisen parameter and isentropic bulk modulus. We use the Murnaghan approximation for the bulk modulus, fitted on the PREM model with an 8% density deficit, for which the rationale is explained in detail in Section 4.1 of Clesi and Deguen (2023),

$$K_s = K_0 + K'P, \tag{3}$$

with $K_0 = 128.49 \pm 3.63$, and $K' = 3.67 \pm 0.1$ the parameters obtained by Clesi and Deguen (2023) to simplify the equation of state. Since the fit is made on (Dziewonski and Anderson, 1981) model, the relative errors are the same as in the PREM model, 4%. This equation yields the following equation of state for the metal:

$$\frac{\rho(P)}{\rho_0} = \left(1 + \frac{K'}{K_0} P\right)^{1/K'}, \tag{4}$$

where ρ denotes density. The value of ρ_0 is varying throughout accretion, depending on the composition of the metal after chemical equilibration (or lack thereof in this study) with the silicates (see Clesi and Deguen (2023) for the details). This is theoretically a problem, as we keep K_0 and K' constant. However, the main driver of change for those parameters is the concentration of sulfur (Sanloup et al., 2000), which is absent from our models. The main light element in our outputs is Si, which does not affect the bulk modulus as much as S (see, Morard et al., 2013,

and references therein). Therefore, keeping K_0 constant does not affect much the output of the model. This problem, and the limitations of interpretation it imposes, is discussed in section 4.1 and 7.1 of Clesi and Deguen (2023)

Following the study of Clesi and Deguen (2023), we use the formalism of Al'Tshuler et al. (1987) for the calculation of the Grüneisen parameter γ given by:

$$\gamma = \gamma_\infty + (\gamma_0 - \gamma_\infty)\left(\frac{\rho_0}{\rho}\right)^\beta, \tag{5}$$

where $\beta = \gamma_0/(\gamma_0 - \gamma_\infty)$, with $\gamma_0 = 1.933$ and $\gamma_\infty = 0.916$ as refitted in Clesi and Deguen (2024b). These values might not be appropriate to get a precise estimate of the core temperature, but the formalism chosen tends to limit the sensitivity of the output to the value chosen introduced by the uncertainty on γ_0 and γ_∞ (Clesi and Deguen, 2024b). The model sensitivity to the Grüneisen parameter will introduce an overall error on the mean value of 6% (determined from the data in Table 4 of Clesi and Deguen, 2024b). The propagation of the error is detailed in Supplementary Section S.5. Nonetheless, the goal of the study is not to determine the precise temperature of the core, but to assess the sensitivity of the thermal model to a specific chemical phenomenon, in this specific instance the dilution and disequilibrium during core/mantle segregation. With this Grüneisen formalism, integrating Equation 2 during the accretion yields:

$$T(P) = T_{eq}\left(\frac{K_0 + K'P}{K_0 + K'P_{eq}}\right)^{\frac{\gamma_\infty}{K'}} \times \exp\left[\frac{\gamma_{0,j} - \gamma_\infty}{\beta}\left(\left(1 + \frac{K'P_{eq}}{K_0}\right)^{-\frac{\beta}{K'}} - \left(1 + \frac{K'P}{K_0}\right)^{-\frac{\beta}{K'}}\right)\right]. \tag{6}$$

where P is the final pressure of the metal in the stratified case (the difference between stratified and mixed core is discussed further in Clesi and Deguen (2023)). The heat content of the core is then calculated as

$$Q = 4\pi \int_0^{R_{core}} \rho(r) C_p T(r) r^2 dr, \tag{7}$$

where R_{core} is the radius of the core, r the distance from the center of the core, and $C_p = 1000 J.kg^{-1}.K^{-1}$ the specific heat capacity of the metal, kept constant throughout the model. The limitation of this choice, governed by the choice to simplify the model, is discussed in Sections 4 and 7 of Clesi and Deguen (2023). The the link between the radius of the core and pressure $P_{core}(r)$ within the core is given by:

$$P_{core}(r) = P_{center} + \left(\frac{P_{CMB} - P_{center}}{R_{core}^2} \right) r^2, \tag{8}$$

where $P_{center} = 360 GPa$ and $P_{CMB} = 136 GPa$ denote pressure at the center of the core and CMB, obtained by derivation of the hydrostatic equation applied to a two-layered body, with the detailed equations in Clesi and Deguen (2023) and references therein. The isentropic temperature profile can then be obtained by integrating

$$\left(\frac{\partial \ln T^{is}}{\partial \ln \rho_{core}} \right)_s = \gamma. \tag{9}$$

where γ is the Grüneisen parameter given in Equation 5. In the final step of calculation we consider a fully mixed core with a constant heat content, which allows us to calculate the temperature at the CMB following:

$$T_{CMB}^{is} = \frac{Q}{4\pi \int_0^{R_c} \rho^{is}(r) C_p T^{is}(r) r^2 dr}, \tag{10}$$

which is evaluated numerically. In the following sections, we will evaluate how T_{CMB}^{is} evolves when applying a chemical disequilibrium at stage (i) of the model, thus changing the composition and density profile of the core. Before describing the chemical model, we must however acknowledge that the initial temperature in

Equation 1is overestimated, both because of the liquidus choice and because we chose to set this temperature at the liquidus. Indeed, it would have been more physically sound to consider the case where metal-silicate equilibrium happens in a mushy zone where some of the silicate is crystallized, as it would slow the metal. With such a mechanism, the temperature would be comprised between the solidus and the liquidus which would translate into a lower initial temperature. As it is standard to set the temperature at the liquidus in metal-silicate partitioning study (among other, Rubie et al., 2003; Siebert et al., 2012; Fischer et al., 2015, 2017; Suer et al., 2021; Gu et al., 2023; Loroch et al., 2024), and we want to be able to compare our results with these studies and the initial study (Clesi and Deguen, 2023), we will keep this overestimation throughout.

3 Description of the chemical model

The thermal model described above is linked to a chemical model of core/mantle segregation. In this section, we present briefly the initial model used in Clesi and Deguen (2023), and the modifications made to it so as to model a chemical disequilibrium during core/mantle segregation.

3.1 Inputs of the models

We tested a whole range of metal-silicate segregation scenario during accretion. In all of the models presented below, the initial conditions of core-mantle segregation are fixed by the pressure of equilibrium, representing the bottom of the magma ocean. The pressure of equilibrium, P_{eq} is parameterized by:

$$P_{\mathrm{eq}}(f) = a_P P_{\mathrm{CMB}}(f) \frac{1 - \mathrm{e}^{-(f/f_c)^{\lambda}}}{1 - \mathrm{e}^{-(1/f_c)^{\lambda}}}, \tag{11}$$

where f is the mass fraction of the Earth accreted, $P_{\mathrm{CMB}}(f)$ is the pressure at the CMB for a given mass fraction accreted and the parameters a_P, f_c and λ are the varying parameters. The average value of P_{eq}, noted $\overline{P_{\mathrm{eq}}}$ in the rest of the text, is

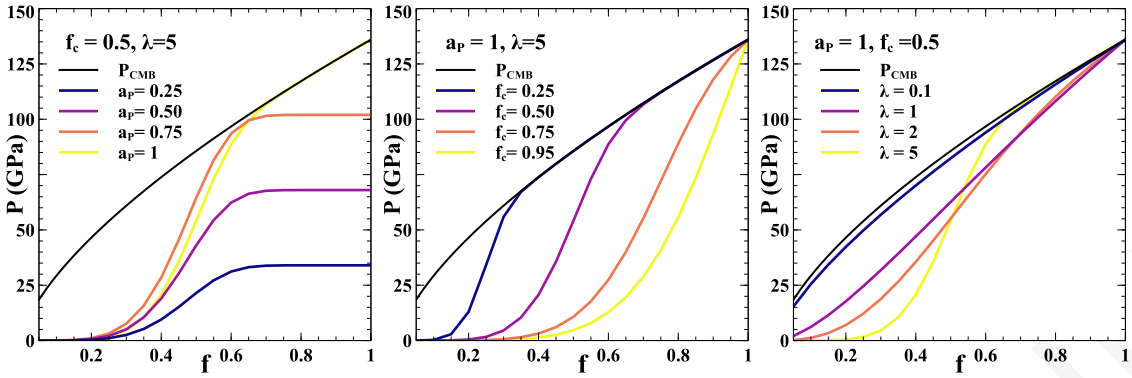

Figure 1: Description of the effect of the parameters used in Equation 11 on the value of P_{eq}. The black line is the pressure at the CMB, $P_{\mathrm{CMB}}(f)$. The left panel shows of P_{eq} with $f_c = 0.5$ and $\lambda = 5$ with variable a_P. The middle panel shows the evolution of P_{eq} for $a_P = 1$ and $\lambda = 5$ with variable f_c. The right panel shows the effect of P_{eq} for $a_P = 1$ and $f_c = 0.5$ with λ variable.

representative of the average depth of equilibrium (Clesi and Deguen, 2023), and as such used preferentially in the interpretations of the results in Section 4. Equation 11 is a convenient equation to span a range of possible scenarios for the evolution of magma ocean depth, and it is not linked to any physical mechanism such as impact/melt scaling (Nakajima et al., 2021). This purely mathematical form can be interpreted roughly as specific scenarios, see Supplementary Figure S.15 in this study, the figures in Clesi and Deguen (2024a) and the section 3.1.2 of (Clesi and Deguen, 2023)

The effect of each parameter on the evolution of the equilibrium pressure P_{eq} is shown in Figure 1. As shown in the left panel of Figure 1, a_P is the parameter controlling the maximum pressure at the end of accretion, with only the examples of a_P = 0.25, 0.50, 0.75 and 1 shown on Figure 1. In the present study, we varied the parameter a_P between 0.05 and 1. Depending on the values of f_c and λ, the pressure of equilibrium approaches $a_P P_{CMB}(f)$ sooner or later during the accretion, but the maximum is set by a_P. For $a_P = 1$, the value of P_{eq} reaches the same value as the pressure at the CMB, for $a_P = 0.5$, P_{eq} will always be lower or equal to half of the CMB pressure at any point of accretion. In the middle panel of Figure 1, we show the effect of the scale parameter f_c on the evolution of the pressure of equilibrium. This parameter sets the moment in accretion when the pressure increases faster,

Elements	Reduced material	Oxidized material
Silicate phase		
SiO_2	51.41	42.19
MgO	37.5	29.40
Al_2O_3	4.62	3.63
CaO	3.75	2.95
FeO	2.24	21.13
NiO (ppm)	10.1	174
CoO (ppm)	5.1	83
Cr_2O_3 (ppm)	4500	6170
V_2O_3 (ppm)	203	164
Metallic phase		
Fe	91.1	89.07
Ni	5.55	10.0
Co	0.26	0.34
Si	2.4	0.0205
Cr (ppm)	6100	870
V (ppm)	9.24	0.775
O	0.04	0.4
Metallic mass fraction of the impactor		
-	0.313	0.165

Table 1: Impactor composition given in Fischer et al. (2015) supplementary material and used in our model. All units are in wt % except where ppm is specified.

especially for high values of λ. It is also when we chose to change the oxidation state of the impactor, and therefore the initial composition of metal and silicate accreted, from a reduced composition to an oxidized composition (see below and Table 1). Finally, the right panel of Figure 1 shows the effect of the shape parameter λ on P_{eq}, determining the shape of the accretion profile. When $\lambda = 0$, Equation 11 becomes $P_{eq}(f) = a_P P_{\mathrm{CMB}}(f)$, i.e. the magma ocean pressure is a fixed fraction of the CMB pressure all along the accretion, as it is classical in several other studies (Wood et al., 2008; Siebert et al., 2012; Bouhifd et al., 2007; Clesi et al., 2016). When $\lambda \to \infty$, the Equation 11 becomes a step function with $P_{eq}(f) = 0$ for $f < f_c$ and $P_{eq}(f) = a_P P_{\mathrm{CMB}}(f)$ for $f > f_c$. As can be seen in Figure 1, using a finite value of λ, varying between 0.1 and 5 in this study, smoothes out the step function, and the transition from a shallow (i.e. low P_{eq}) to a relatively deep magma ocean (i.e. P_{eq} close to the maximum pressure allowed by a_P value).

The scale parameter f_c does not only control the transition of regime for high values of λ, but also the composition of the impacting masses, combining the two transitions being a convenient way of simplifying the model, and is compatible with N-Body simulations results, as argued in Section 3.1.2 and 4 of Clesi and Deguen (2023). We chose a simple model with only two different initial compositions: one reduced and one oxidized. The compositions, taken from Fischer et al. (2015), exhibit CI-chondritic elemental ratios (Wasson and Kallemeyn, 1988) in order to match the refractory lithophile element trend in the Bulk Silicate Earth (McDonough and Sun, 1995). For $f < f_c$, the Earth is accreting the reduced composition presented in Table 1, and for $f > f_c$ the Earth is accreting the oxidized composition presented in Table 1. Accreting reduced material before oxidized material is consistent with N-body simulations of Solar System formation that tend to accrete inner solar system material material (hotter, more reduced and less rich in volatile elements) first and outer solar system material (cooler, more oxidized and rich in volatile elements) at the end of accretion (Morbidelli et al., 2000; Raymond et al., 2009; Izidoro et al., 2021). The parameters and compositions presented in this section are used in all of the models presented in the following subsections, and a schematics of the physical meaning of the model, derived from Clesi and Deguen (2024a), is given in supplementary Figure S.14. The models do not consider a specific Moon-forming impact, as we tried to keep every input parameter independent. As every input parameter is kept independent of the impactor's size (in particular k and Δ), the end results are exactly the same, see Clesi and Deguen (2024a) and supplementary Figures S.2 to S.6. This point is also discussed further in Section 4.

3.2 Reference chemical model description

The core-mantle segregation model we will take as a reference for this study is based on the work of Fischer et al. (2015), with the link to the thermal model being explained in Clesi and Deguen (2023). A qualitative description of the model is given in Figure 2. The model consists of the following steps of calculations:

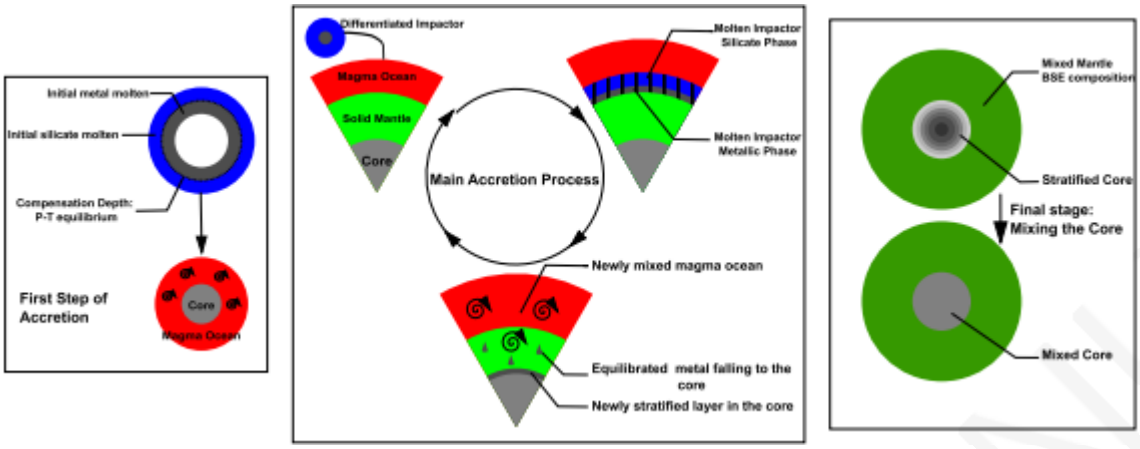

Figure 2: Qualitative description of the model as described in Fischer et al. (2015) and in Section 3.2. The left rectangle described the first step of accretion, setting the initial composition of the planestesimal. The middle rectangle describes the main accretion process: an impactor on a magma ocean is re-equilibrated at the bottom of the magma ocean before segregation of the core and mixing of the whole mantle by vigorous convection. The right rectangle shows the last part of the model: once the mass of the Earth is obtained, we calculate the heat content of a segregated core and calculating the temperature of a mixed core.

i Initialisation of the calculation: we accrete a planetesimal corresponding to 5 % of the Earth mass, and calculate the initial core and mantle composition by equilibrating the entire mass of the metal and silicate at a given pressure. This equate to a single stage model for the first 5% of accretion, which is standard for small bodies (e.g. Grewal et al., 2019, and references therein)

ii Main accretion process: the Earth is growing by adding impactors of 5% of the Earth size. All of the metal in the impactor mass and only the impactor silicate mass are re-equilbrated at the bottom of the magma ocean, which set the pressure and temperature of equilibrium (P_{eq} and T_{eq}). The metal then sinks into the core, adding a chemically different layer on top of the growing core. During the descent, the temperature of the core is increasing from T_{eq} to its final temperature due to compressional heating during the migration of the metal through the mantle, and further compression due to Earth's growth, following Equation 6. It is chemically insulated from the mantle and the other layers of core. Before another impactor is added, the mantle is considered well-mixed. This process continues until the entire Earth mass is accreted.

iii Final stage: at the end of the main process, we get a fully accreted Earth with a stratified core and a well-mixed mantle. We consider that the core is then mixed isentropically to calculate the temperature at the CMB, T^{is}_{CMB}, given by Equation 10.

At each step, the composition of mantle and core is simplified, and we consider the following equilibrium described by Rubie et al. (2011):

$$\begin{gathered}\left[(FeO)_x(NiO)_y(SiO_2)_z(Al_uCa_mMg_p)O + Fe_aNi_bO_cSi_d\right] \\ \updownarrow \\ \left[(FeO)_{x'}(NiO)_{y'}(SiO_2)_{z'}(Al_uCa_mMg_p)O + Fe_{a'}Ni_{b'}O_{c'}Si_{d'}\right]\end{gathered} \tag{12}$$

The equilibrium of Reaction 12 is described by sub-reactions for each element involved, following:

$$MO^{m.o.}_{n/2} + \frac{n}{2}Fe^m \rightarrow M^m + \frac{n}{2}FeO^{m.o.}, \tag{13}$$

where $MO^{m.o.}_{n/2}$ is a given element of valence n in oxide form in the magma ocean phase, and M^m the metallic form of the element in the metallic alloy. The equilibrium of each sub-reaction is set by the exchange partitioning coefficient K_d, which is parameterized by:

$$log_{10}K^M_d = a_M + \frac{b_M}{T_{\text{eq}}} + \frac{c_M P_{\text{eq}}}{T_{\text{eq}}}, \tag{14}$$

where P_{eq} is expressed in GPa, T_{eq} in K, and considering that the activity coefficients of all elements are equal to unity. The coefficients (a_M, b_M and c_M) of equation 14 for each element are the one given in Fischer et al. (2015). For a given element the exchange partitioning coefficient is by definition:

$$K^M_d = \frac{\chi^m_M}{\chi^{m.o.}_{MO_{n/2}}}\left(\frac{\chi^{m.o.}_{FeO}}{\chi^m_{Fe}}\right)^{n/2}, \tag{15}$$

with χ_M^m the molar fraction of element M in the metallic phase, and $\chi_{MO_{n/2}}^{m.o.}$ the molar fraction of the corresponding oxide in the silicate. Combining Equation 12 and equation 15 with the K_d^M value set by equation 14 allows to calculate the final equilibrated composition of both phases with a self-evolving oxygen fugacity. The partitioning of V, Cr and Co are also calculated after the initial equilibrium of reaction 12 using the same method. The main calculation consist in solving the mass balance system of equations:

$$\begin{aligned} x + a &= x' + a' \\ y + b &= y' + b' \\ z + d &= z' + d' \\ x + y + 2z + u + m + p + c &= x' + y' + 2z' + u + m + p + c' \end{aligned} \tag{16}$$

with a, b, c, d, u, m, p, x, y, z, a', b', c', d', x', y', z' the number of moles of the elements involved in reaction 13. This system of equation is combined with the one created by the K_d of Ni, Si and O, with Equation 15 applied for each element. For instance for Ni, an element with a valence of 2, expressing Equation 15 becomes:

$$K_d^{Ni} = \frac{b'}{a' + b' + c' + d'} \times \frac{x' + y' + z' + u + m + p}{y'} \times \left(\frac{x'}{x' + y' + z' + u + m + p} \times \frac{a' + b' + d'}{a'} \right)^{2/2} \tag{17}$$

Combining system 16 with 17 for Ni, Si and O yields a system of 7 equations with 7 unknown (a', b', c', d', x', y', z') that allows for several solutions, only one respecting the constraint that no mass can be negative. The complexity comes from the formula of K_d^O, which is calculated using the formula given in Frost et al. (2010). The valence 3+ elements (V and Cr) are solved after the main calculation, because the system would become harder to solve analytically. It introduces an error in the masses of silicate and metal, but it is limited to a variation of 0.01 to 0.1 %. The detailed method of solving the system of equation calculation is described in the supplementary information of Rubie et al. (2011) and Clesi and Deguen (2023). The number of moles involved in the initial stage of the reaction is calculated using the

mass and composition of the silicate and metal involved in the metal-silicate reaction 12. In the case of the reference model of this study (Fischer et al., 2015; Clesi and Deguen, 2023), the mass of both silicate and metallic phase involved is equal to the silicate and metal in the impactor (Figure 2). The composition of each phase involved is also the composition of the impactors, given in Table 1. The number of mole for element in the metal M is therefore:

$$\mathcal{N}_M^{met} = \frac{m_{metal}^{impactor} X_M^{m,imp}}{\mathcal{M}_M}, \tag{18}$$

where $\mathcal{N}_M^{met}$ is the number of mole of M (a,b,c or d in Reaction 12), $m_{metal}^{impactor}$ is the mass of metal in the impactor, $X_M^{m,imp}$ the mass fraction of element M in the metallic phase of the impactor and $\mathcal{M}_M$ the molar mass of element M. As for the silicate, the number of mole of an oxide $MO_{n/2}$ is given by:

$$\mathcal{N}_{MO_{n/2}}^{sil} = \frac{m_{silicate}^{impactor} w_{MO_{n/2}}^{sil,imp}}{\mathcal{M}_{MO_{n/2}}}, \tag{19}$$

with $\mathcal{N}_{MO_{n/2}}^{sil}$ the number of mole of $MO_{n/2}$ (x, y, z, u, m, p in Reaction 12), $m_{silicate}^{impactor}$ the mass of silicate in the impactor, $w_{MO_{n/2}}^{sil,imp}$ the mass fraction of $MO_{n/2}$ in the silicate phase of the impactor and $\mathcal{M}_{MO_{n/2}}$ the molar mass of oxide $MO_{n/2}$.

Since only the impactors are equilibrated, the bulk composition at a given mass fraction is given by:

$$w_{i,\text{bulk}}^{s+}(f) = \frac{w_i^s(f) m_{\text{accreted}}^s(f) + w_{i,\text{bulk}}^{s-} M_{\text{mantle}}^-}{M_{\text{mantle}}^+}, \tag{20}$$

where $w_{i,\text{bulk}}^{s-}(f)$ and $w_{i,\text{bulk}}^{s+}(f)$ are the bulk concentrations (in % wt) before and after each addition of mass, and M_{mantle}^- and M_{mantle}^+ the masses of the mantle before and after the impact ($M_{\text{mantle}}^+ = M_{\text{mantle}}^- + m_{\text{accreted}}^s(f)$). When properly calculated at each step of accretion then for f=1, Equation 20 yields the bulk composition of the mantle. The same equation can be applied to the core, only by replacing the masses of silicate and mantle by the masses of metal and core respectively.

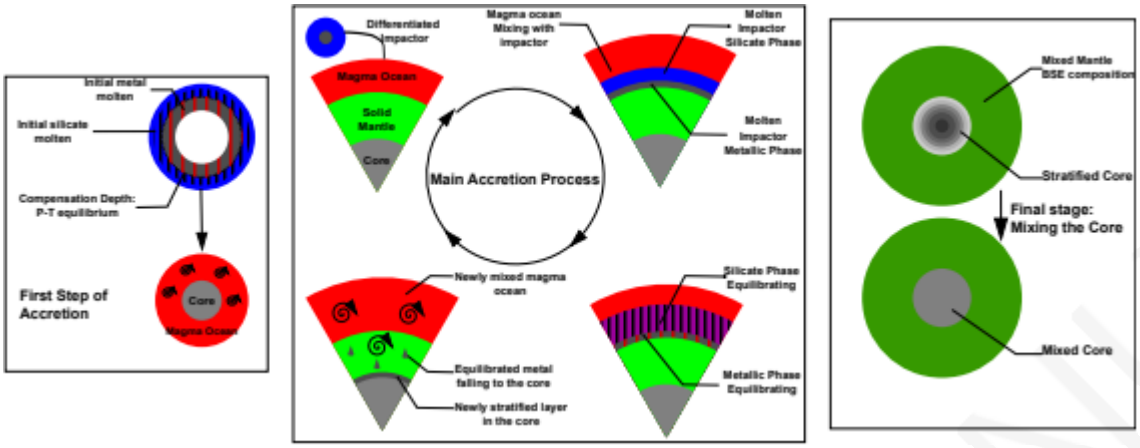

Figure 3: Schematic of the model of disequilibrium used in this study. In all steps only a part of the metal and the silicate is considered to have reacted, even at the first initiation stage. The vertical striped areas represent the amount of metal and silicate reacting. For readability, we considered $k = 1$ (all metal reacted) and an arbitrary value of Δ. Compared to Figure 2, a mixing step has been added before the actual reaction. The amount of silicate equilibrated is colored purple with black stripe in the main accretion stages, and is calculated on the fully mixed magma ocean before reacting with the metal. Once the purple part composition is changed, the magma ocean is fully mixed before the subsequent impact. The last part of the model (re-mixing of the core and mantle) is the same as in the reference model. The display of equilibrated silicate and metal in layers has been chosen to simplify the visualization of the masses and does not represent the actual physical reality of the equilibrium process and subsequent mixing.

3.3 Modeling of disequilibrium

Now that the reference model is described, we used the calculation technique of Deguen et al. (2014) to model the disequilibrium between the phases. Since the model is not a time-resolved model, the degree of equilibrium is approximated by the amount of reacting silicate (black stripes) and reacting metal (red stripes) that are equilibrated. To simplify the calculation of these masses at each step, we considered that the silicate impactor is mixed with the previous mantle before reacting.

We therefore define, following Deguen et al. (2014), two parameters that are used to model this phenomenon: k, a parameter describing the amount of metal that is equilibrated and Δ, the degree of dilution of the metal, i.e. the amount of silicate that is equilibrated. The parameter k is defined by:

$$k = \frac{m_{eq}^{met}}{m_{total}^{met}}; \tag{21}$$

where m_{eq}^{met} is the mass of metal that is equilibrated, and m_{total}^{met} is the total mass of the metal added from the impactor. The parameter Δ is defined by :

$$\Delta = \frac{m_{eq}^{sil}}{m_{eq}^{met}}; \tag{22}$$

where m_{eq}^{sil} is the amount of silicate equilibrated, and m_{eq}^{met} is the amount of metal equilibrated given by equation 21. This way of defining the degree of equilibrium links the amount of equilibrium in the silicate to the amount of equilibrium in the metallic phase, therefore not treating the equilibrium in each phase as independent parameters. Therefore, direct comparison with studies such as Gu et al. (2023) cannot be performed as the amount of silicate equilibrated for a given value of Δ varies first with the value of k (see Equation 22) and varies also within the accretion model (in particular the parameter f_c, see Figure S.16), since the total amount of metal added depends on the moment of accretion, the mass added being lower for the oxidized part of the accretion process (see Section 3.1). For the higher values of Δ ($\sim$ 90 to 100, depending on the value of k), the entire mantle is equilibrated (see Figure S.16 for the actual percentage of mantle equilibrated). We tested the models for k ranging between 0.05 and 1, and for Δ ranging between 1 and 500. The values higher than $\Delta = 100$ are redundant since 99.9 to 100 % of the mantle is equilibrated, but serves as control of the stability of the model.

3.4 Definition of a solution and reference model

In equation 11 we varied the parameters as follows: the parameter a_P takes 20 values between 0.05 and 1 (0.05 steps), the parameter f_c also 20 values between 0.05 and 1, and the parameter λ takes 50 values between 0.1 and 5 (0.1 steps). All the combinations within those values are tested, thus yielding 20 000 models. For a discussion on the choice of bounds for those values, see Clesi and Deguen (2023), section 3.1.1. For each (k, Δ) couple we tested these 20 000 combinations. In these 20 000 models, the outputs mantle compositions are not necessary close to the Bulk Silicate Earth (BSE) composition. Therefore, we consider a model

given by a (a_P, f_c, λ) triplet to be a solution if all the elemental concentrations are within an acceptable range relatively to the BSE as defined in McDonough and Sun (1995). All major elements concentrations are considered solutions if their values are within a 10 % range of the values of the BSE: $w_{SiO_2}^{mantle} = 45.18 \pm 4.52$ $\%wt$, $w_{Al_2O_3}^{mantle} = 4.47 \pm 0.45$ $\%wt$, $w_{FeO}^{mantle} = 8.10 \pm 0.81$ $\%wt$, $w_{MgO}^{mantle} = 38.03 \pm 3.80$ $\%wt$ and $w_{CaO}^{mantle} = 3.56 \pm 0.36$ $\%wt$. For the trace elements, the concentrations are considered solutions if their values are within 15% of the values of the BSE: $w_{NiO}^{mantle} = 2509 \pm 376$ ppm, $w_{CoO}^{mantle} = 134 \pm 20$ ppm, $w_{V_2O_3}^{mantle} = 121 \pm 18$ ppm and $w_{Cr_2O_3}^{mantle} = 3859 \pm 579$ ppm. In this work, the reference model solutions to which everything will be compared is the model described in Section 3.2 and Figure 2 for which the filter described above has been applied. This differs from Clesi and Deguen (2023) in which we used a weighted method that tends to yield more solutions by allowing some elements concentrations, in particular V and Cr, to be outside the 15% range of the BSE concentration. This effect of threshold choice is discussed in Supplementary Section S.3, Figure S.7 to S.8. Increasing the threshold to 20% for Ni, Co, V and Cr increases the number of solutions and widen the range of output values, but does not change the average values significantly. Overall, the trends highlighted in Clesi and Deguen (2023) (correlation between light elements concentration in the core, core temperature and mean pressure of equilibrium) are the same, with less points (see Figure S.15). Some of the models with high values (40 to 50 GPa) of $\overline{P_{eq}}$, and therefore higher concentrations of Si and O in the core (w_{Si+O}^{core} above 6% wt), are removed from the dataset. A comparison between the solution from Clesi and Deguen (2023) and the reference we use in this study (also used in Clesi and Deguen, 2024a, under the name C20) is presented in Figure S.15. This shows that the kind of filter applied to define a solution does affect to some extent the output of the models. Several other filters could have been used for instance using the mean quadratic difference like in Rubie et al. (2015) or using uniquely the N-body simulation results combined with a sensitivity study as in Gu et al. (2023). In any case, the trends we highlighted in Clesi and Deguen (2023) would yield correlations

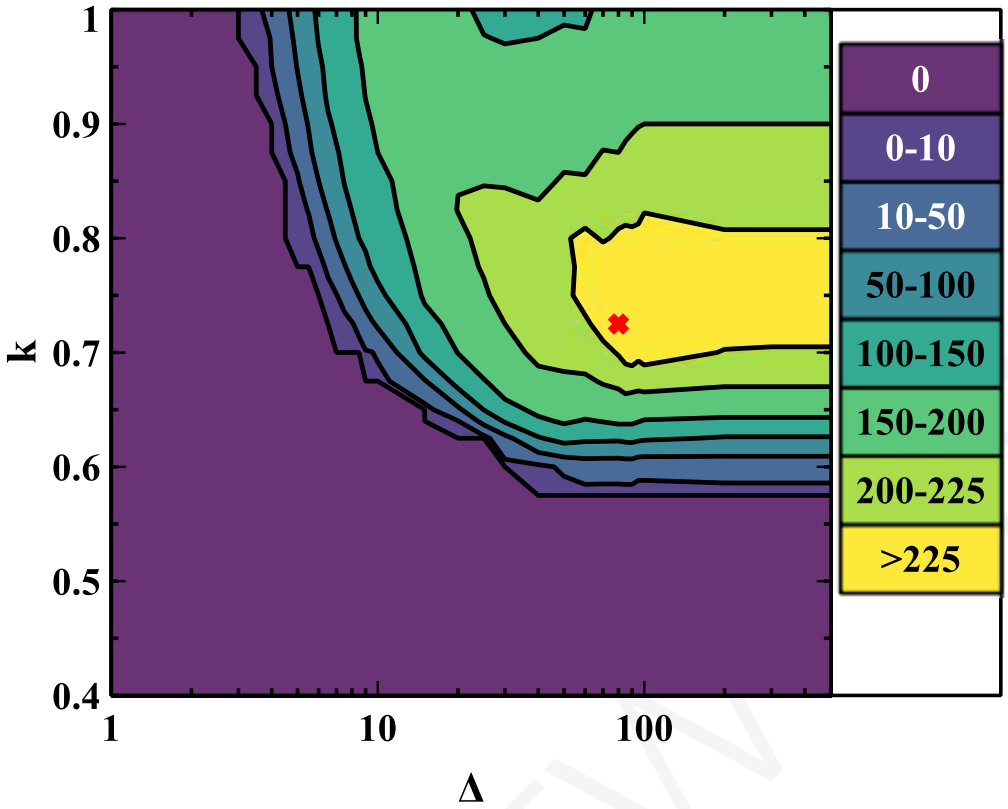

Figure 4: Number of solutions yielded by the model for different values of k (fraction of metal equilibrated, Eq. 21) and Δ (silicate mass equilibrated, see Eq 22). x-axis is in logarithm scale, y-axis in linear scale. The red cross marks the maximum value (n = 241) at k = 0.725 and Δ = 80.

in the same order of magnitude, as evidenced by the comparison of two methods for selecting a solution provided in Figure S.15. The effect of filter width, or rather its low effect, in relation to the BSE model is discussed more in details in supplementary Section S.3.

4 Results of the calculations and their implications

4.1 Number of solutions and implications for the Hf-W chronometer

For the range of k and Δ tested (i.e. the prior distribution described in Section 3.4, the models yield between 0 and 241 solutions. This success rate ranges between 0 and 1%, which is comparable to the efficiency of implantation of 0.07% given in Walsh et al. (2011), and comparable to the success rate of Raymond et al. (2009) for N-Body simulations able to produce a Mars-sized planet. The maximum absolute

number of 241 successful scenarios is in line with the number of simulations used in the similar study of Gu et al. (2023), where 201 Earth analog are taken out 765 N-body simulations (numbers from their Table 1). As for N-body simulations, these numbers are dependent on the limits imposed of the filters for solutions, see Section 3.4 and Supplementary Material S.3. This number of solution defines a likelihood under the uniform prior distribution described in Section 3.4. This likelihood is barely changed with increasing the sampling range, see Supplementary Section S.4 and Figure S.12 to S.13 . As shown in Figure 4, most of the disequilibrium models do not yield any solution: for any value of k below 0.6 and for any value of Δ below 4, no model will yield a BSE-like mantle. This shows the need to have at least some equilibration in both phases. For dilution factors Δ superior to 100, the number of solutions for a given value of k does not change, indicating that the full mantle is equilibrated during the entire time of accretion (see also Figure S.15). Figure 4 also shows that the maximum number of solutions is not reached for full equilibration of both phases: the optimum is obtained when 70 to 80 % of the metallic mass is equilibrated with a dilution factor between 55 and 100. Higher equilibrium degrees in the metal or in the silicate do not increase the number of solutions, and even tend to decrease the number of solutions in the case of the values of k. This indicates that it is easier to model the accretion of the BSE with some moderate disequilibrium in the metal, at least with the chondritic material we used in these models. Finally, the number of solutions drastically decreases for $k < 0.7$ and for $\Delta < 30$. Therefore, while it is easier to produce a BSE mantle with moderate disequilibrium, it is highly improbable to form the Earth with a low degree of equilibrium in the silicate or metallic phase.

The results laid out in Figure 4 shows that the minimum amount of equilibrium is 60%, higher than the model of Rudge et al. (2010) who proposed a minimum value of 36 % for a similar definition of k, thus allowing comparison with our study. This value is a minimum as applying more precise filters tends to only decrease the number of solution (see Figure S.4 in Clesi and Deguen (2023)). This point is even clearer

as we tried different filters on the current model (See Supplementary Section S.3). Increasing the filter size increases the number of solutions, but also the distance to the BSE composition (See Figure S.4 to S.6 of Clesi and Deguen (2024a) and Figures S.9 to S.11 of the present study). Decreasing the limits decreases the overall number of solutions and moves the minimums of k and Δ towards higher values. Since the initial filters are the upper bounds given by **?** for the BSE, the threshold of $k = 0.6$ and $\Delta = 4$ are strong minimum values if the model to be fitted is the BSE as presented in **?**. More details on this subject can be found in Supplementary Section S.3 and Figure S.7 to S.11. The discrepancy between our study and Rudge et al. (2010) could be explained by the fact that our parameterization of metal/silicate partitioning is the same as Fischer et al. (2015), while Rudge et al. (2010) used Wood et al. (2008) and Wade and Wood (2005) for moderately siderophile elements. Furthermore, their initial starting material is also different than the one used in the present study, and because disequilibrium is an extensive phenomena, even using the same parameterization of metal-silicate partitioning would yield different results. The lowest value of Δ that yields a consistent BSE composition is found to be smaller than found from Deguen et al. (2014): for $k = 1$ we find the minimum value of Δ to be 4, while they propose $\Delta = 17$. This value of 17 is obtained in Deguen et al. (2014) by focusing on the tungsten (W) partitioning in the case of a small magma ocean relatively to the size of the metallic impactor's core.

We can further note two things:

- Our limited number of elements for which we calculate the Earth's composition might not be selective enough to constrain the degree of equilibrium, and adding other elements (among them W or S, for instance) would change the domain of possibility presented in Figure 4
- Applying a constant value of k and Δ throughout the entire process of accretion is a rough estimation of the degree of disequilibrium, and more precise results would be achieved by including dynamical element to the model (relative size of metallic particles, entrainment coefficient in particular, see Deguen et al. (2014)).

In summary, the most probable values of k for our model is comprised between 0.7 and 0.8, which, according to the Hf-W chronometer developed by Rudge et al. (2010) will favors rapid formation of the core: between 20 and 50 Myrs (for two-stage or exponential model of accretion, respectively). Further developments of the model need to include more elements, including W, and to take into account the dynamical element of metal-silicate segregation so as to further constrain the time scale of core formation with the degree of equilibrium of metal and silicate.

4.2 Chemical equilibrium control on the accretion scenarios

In this section we present how the degree of equilibrium affects the type of model that can yield coherent chemical solutions.

4.2.1 Effect of silicate dilution

On Figure 5 are presented the evolutions of the different input parameter values that yield chemically coherent solutions as a function of the amount of equilibrium in the silicate (Δ) for $k = 0.6$, $k = 0.75$ and $k = 1$. Other plots, in the same fashion but for the other elements composing the mantle and the core, are presented in supplementary Figures S.17 to S.32. No effect of silicate dilution can be seen on the parameter f_c, which controls the redox state of the impactor: the f_c range is between 0.8 and 1, with mean values close to 0.75 for every model, including the reference model. Therefore, the amount of disequilibrium during core-mantle segregation does not affect the redox state significantly: most of the accretion has to be from reduced impactors (more than 80 %) with the more oxidized impactors arriving at the end. For most of the values of Δ, some models can yield chemically coherent Earth mantles for a fully reduced accretion. However,it is impossible to accrete chemically coherent Earth for a fully reduced accretion at very low values of Δ ($\Delta \sim 4-7$, Figure 5, panels h. and i.). This effect is enhanced for low values of k (Figure 5, panel g.), which indicates it is impossible not to accrete oxidized material if the degrees of equilibrium in both phases are very low. This effect is common to Δ and k and is discussed further in the following subsection.

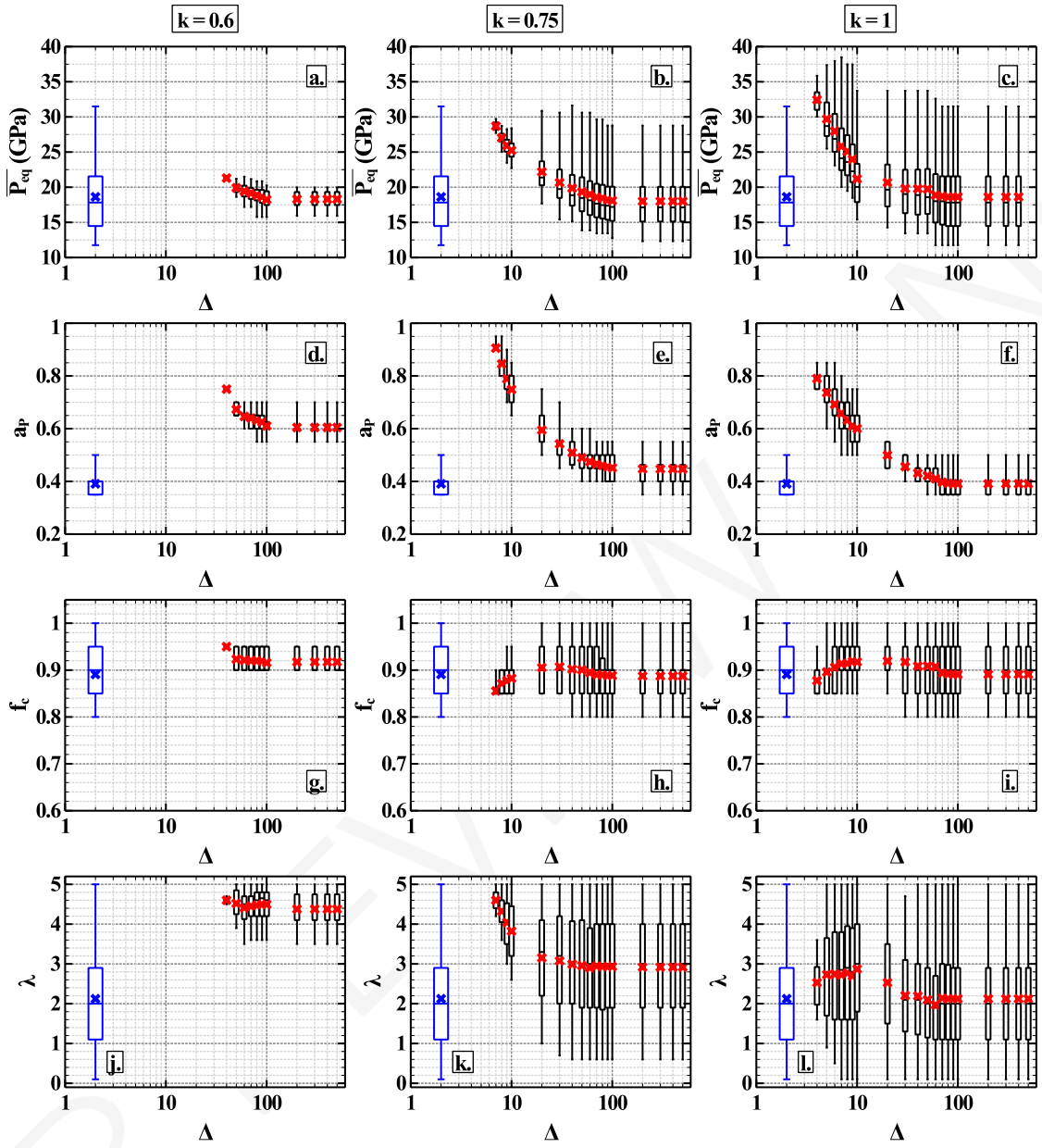

Figure 5: Effect of the silicate dilution Δ on the input parameters controlling the output composition of the model mantle for different values of k. First row, panels a. to c.: $\overline{P_{eq}}$ in GPa. Second row, panels d. to f.: a_P. Third row, panels g. to i.: f_c. Fourth row, panels j. to l.: λ. The left, middle and right column shows the evolution of the parameters values for $k = 0.6$, $k = 0.75$ and $k = 1$, respectively. In each panel the entire solutions range are presented as boxplots, with the red cross being the mean value of the parameter, the white box delimiting the 1st and 3rd quartile, the horizontal line the median value and the vertical lines the minimum and maximum values. The reference model dataset is presented in blue with the same type of plot for comparison at x = 2.

The effect of silicate disequilibrium on the type of solution obtained is the same for each value of k: as Δ is lowered, the mean pressure of equilibrium during accretion is increased in order to get chemically coherent solutions. This effect is more visible on panels b. and c. of Figure 5: for $k = 0.75$ and $\Delta = 100$, the mean value of $\overline{P_{eq}}$ is 18 GPa, while for $\Delta = 7$ the mean value of $\overline{P_{eq}}$ is 28 GPa; and for $k = 1$ the mean value of $\overline{P_{eq}}$ varies between 33 GPa and 18 GPa for Δ varying from 4 to 100, respectively. These values can appear low, as they are mean values throughout the accretion process. However, the final pressures of equilibrium are always higher, since it is the moment of accretion when Ni and Co abundances are set. The issue of interdependence between the different input parameters and the value of $\overline{P_{eq}}$ is discussed in Clesi and Deguen (2023), precisely in Section 5.2, Figures 3 and 4 and Section 6.2, Figure 6.

The parameter a_P, which controls the maximum extent of the magma ocean is likewise increased as Δ decreases: for $k = 1$, the mean value of a_P increases from 0.4 to 0.8 for Δ decreasing from 100 to 4. This mean that when the degree of equilibrium is low, the magma ocean is twice as deep as when the entire magma ocean is equilibrated, thus leading to higher mean pressure of equilibrium during accretion. The final pressures of equilibrium considering the cases presented in Figure 5 range between 30 and 95% of the final CMB pressure, which translate to 40 to 130 GPa for the final pressures of equilibrium. The final depth of the magma ocean ranges between $\sim$ 1000 km at the minimum (high equilibrium degree scenarios, $\Delta \sim 100$ and $k = 1$) to $\sim$ 2700 km at the maximum (low equilibrium degree scenarios, $\Delta \sim 10$, and $k = 0.75$)

The parameter λ, which controls the style of accretion (stable depth of the magma ocean relatively to the size of the planet or sharp transition from shallow to deep magma ocean) is also affected by the silicate dilution imposed on the model. As shown in panels j., k. and l. of Figure 5, the reference model spans the entire range of λ values tested, while it is not the case for the disequilibrated model, especially at low values of k and low values of Δ. Indeed, for $k = 0.75$ the mean value of λ

519 decreases from 4.9 to 3.1 for Δ increasing from 7 to 100. Furthermore, the range
520 of λ values that provides chemically coherent solutions gets narrower as the amount
521 of silicate equilibrated decreases: for $k = 0.6$, the range of λ values is comprised
522 between 3.5 and 5 for all Δ values that yield solutions; for $k = 0.75$, the range varies
523 from 4.2 to 5 for $\Delta = 7$ and from 0.2 to 5 for $\Delta = 100$; and for $k = 1$ the range
524 varies from 1.8 to 3.6 for $\Delta = 4$ and between 0.1 and 5 for $\Delta = 100$. This indicates
525 that when the silicate is not fully equilibrated, the only scenarios of accretion that
526 can yield chemically coherent Earth analogs are the ones that tend to have very
527 shallow magma oceans during most of their accretion process followed by a dramatic
528 increase of magma ocean depth toward the end of accretion.

529 ### *4.2.2 Effect of metal equilibrium*

530 In Figure 6 are shown the evolutions of input parameters values as functions of the
531 metal degree of equilibrium k for $\Delta = 10$, $\Delta = 50$ and $\Delta = 100$. Other plots,
532 focusing on the other elements composing the core and mantle, are presented in
533 supplementary Figures S.17 to S.32.

534 Like the silicate dilution effect, the disequilibrium of the metallic phase has little
535 effect on the acceptable f_c values, with all ranges of solution between 0.8 and 1,
536 and mean values of f_c around 0.88 for all values of Δ. This confirms that in order
537 to get chemically consistent Earth's mantles, accretion scenarios need to include at
538 least 80% of reduced material and less than 20 % of oxidized material at the end
539 of accretion, with some solutions possible for 0% of oxidized accreted material. A
540 noticeable trend on the value of this parameter is that as the values of k and Δ get
541 lower, the range of f_c values gets narrower. For the lowest values of k and Δ that
542 yields solutions, no solution can be found for 100% reduced accretion. This effect is
543 only valid for the minimum values of k (between 0.6 and 0.7 depending on Δ) and
544 the minimum values of Δ (4 to 7 depending on the value of k). This indicate that
545 very low degree of equilibrium during accretion render the accretion of some oxidized
546 material necessary in order to obtain a chemically coherent Earth.

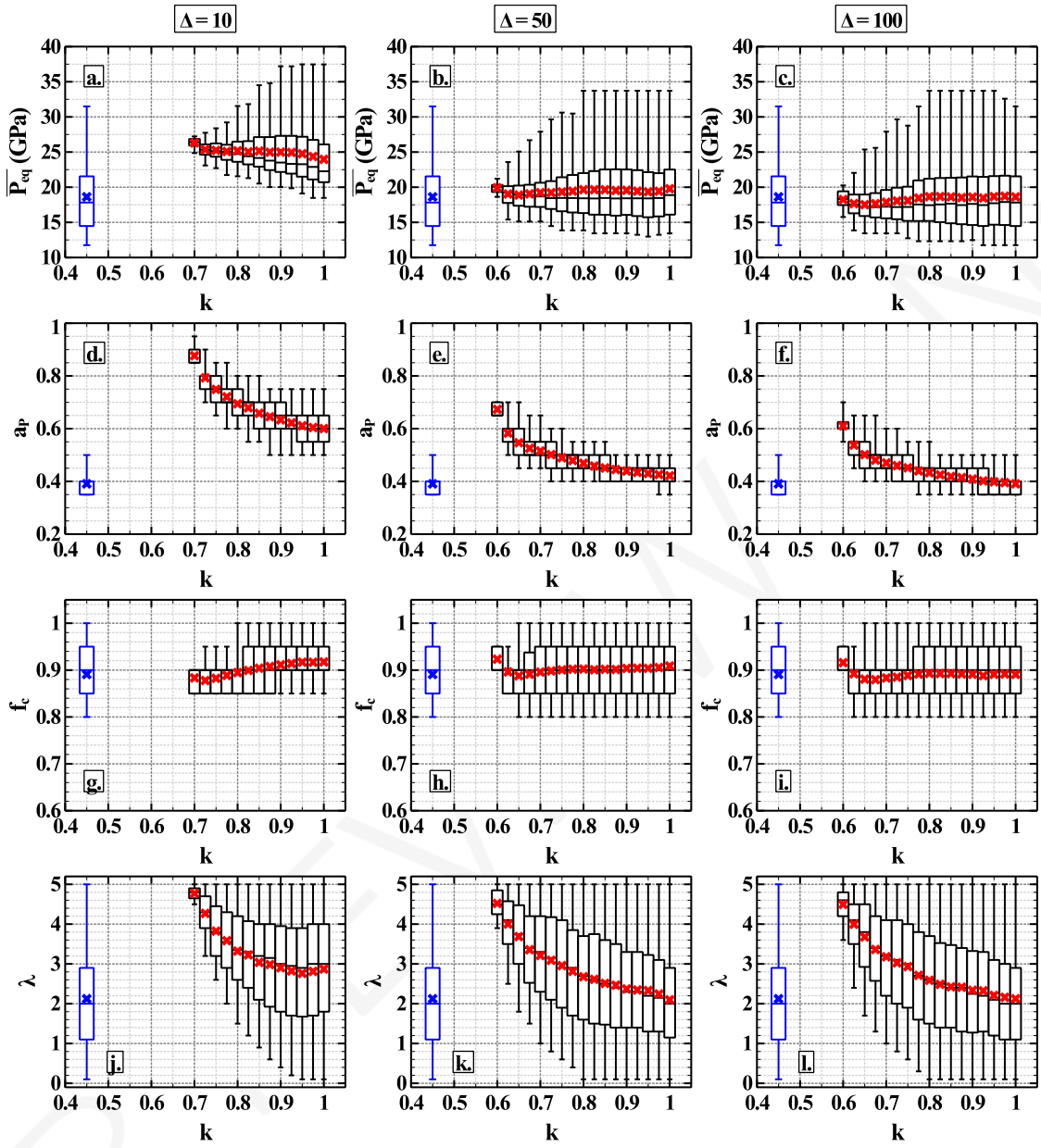

Figure 6: Effect of metal equilibrium k on the input parameters controlling the output composition of the model mantle for different values of Δ. First row, panels a. to c.: $\overline{P_{eq}}$ in GPa. Second row, panels d. to f.: a_P. Third row, panels g. to i.: f_c. Fourth row, panels j. to l.: λ. The left, middle and right column shows the evolution of the parameters values for $\Delta = 10$, $\Delta = 50$ and $\Delta = 100$, respectively. In each panel the entire solutions range are presented as boxplots, with the red cross being the mean value of the parameter, the white box delimiting the 1st and 3rd quartile, the horizontal line the median value and the vertical lines the minimum and maximum values. The reference model dataset is presented in blue with the same type of plot for comparison at x = 2.

The parameter k affects the value of λ in the same way as Δ: decreasing the degree of equilibrium tends to select higher values of λ in order to get a solution. For instance, for $\Delta = 50$ (Figure 6, panel k.), the range of λ that yield solutions is comprised between 3.9 and 5 (mean at 4.5) for $k = 0.6$, and is comprised between 0.1 and 5, *i.e.* the entire range of λ values tested, for $k = 1$. This shows that decreasing the amount of metal equilibrated during accretion favors models where the magma ocean is shallow at first, turning into a deep magma ocean dramatically at the end of accretion. More metal and silicate equilibration tends to favor on the other hand a more steady increase in the magma ocean depth.

The effect of k on $\overline{P_{eq}}$ and a_P is comparable to the effect of Δ: as the amount of metal equilibrated is lowered, the mean pressure of equilibrium is increased in order to get a chemically coherent Earth. This effect is enhanced by lowering the value of Δ: for $\Delta = 100$ (Figure 6, panel f.), the mean value of a_P decreases from 0.61 to 0.4 (i.e. final pressure varying from 83 to 54.4 GPa and final magma ocean depths varying from 1820 to 1280 km) when k increases from 0.6 to 1 ; for $\Delta = 10$ (Figure 6, panel d.), the mean value of a_P decreases from 0.83 to 0.6 (i.e. final pressure from 113 to 82 GPa, and final depth from 2390 to 1800 km), when k increases from 0.7 to 1 . This effect is comparable to the effect Δ has on a_P. This shows that the maximum extent of the magma ocean at the end of accretion is significantly affected by the degree of equilibrium both in the silicate and metallic phases: for low equilibrium degree ($k \sim 0.6$) the final magma ocean extent almost to the CMB ($\sim$ 2700 km), for higher equilibrium degree ($k \sim 1$) the final magma ocean can be more shallow (1000 to 1500 km). However, the clear effect of Δ on the mean pressure of equilibrium during accretion $\overline{P_{eq}}$, shown in the previous section, is less visible, though still present, when plotting the values of $\overline{P_{eq}}$ as a function of k. Indeed, lower k values tend to yield higher mean values (and mostly median values) of $\overline{P_{eq}}$ than higher values of k: for instance for $\Delta = 10$ (Figure 6, panel a.), the mean value of $\overline{P_{eq}}$ is 26 GPa for $k = 0.7$and $\overline{P_{eq}} = 24$ GPa (the median value being 22 GPa) for $k = 1$. This effect is not as clear as the effect of k on a_P, because increasing k

tends to widen the range of $\overline{P_{eq}}$, in particular because the maximum value of $\overline{P_{eq}}$ increases with increasing k. For instance, for $\Delta = 100$ (Figure 6, panel c.), the maximum value of $\overline{P_{eq}}$ increases from 20 GPa for $k = 0.6$ to 32.6 Gpa for $k = 1$ and reaching a maximum at 33.75 GPa for k between 0.7 and 0.95. This discrepancy in the effect of k on a_P and $\overline{P_{eq}}$ which are highly correlated shows that the degree of metal equilibrium controls more the maximum extent of the magma ocean at the end of accretion (which is the physical meaning of the a_P parameter, Figure S.14) than the overall pressure necessary to get a chemically coherent mantle, which is more controlled by the degree of equilibrium in the silicate.

4.3 Chemical equilibrium effect on temperature and core composition

In this section we present how the degree of equilibrium affects the temperature and composition of the Earth's core.

4.3.1 Effect of silicate dilution

The main output of our model is the composition of the core, in particular the Si and O contents, and the heat content (T^{is}_{CMB}) it correlates with. In Figure 7 are presented the evolution of this three properties of the core as a function of Δ for $k = 0.6$, $k = 0.75$ and $k = 1$. The more silicate phase equilibrated, the lower the heat content of the core, especially if a large portion of the metal is equilibrated (see panels a. and c. on Figure 7). For instance, when $k = 1$ (panel c., Figure 7), the mean value of T^{is}_{CMB} decreases from 4050 K to 3970 K when Δ increases from 4 to 100. This relates to the effect Δ has on the input parameters: the more the silicate is equilibrated, the lower $\overline{P_{eq}}$ needs to be to yield a chemically coherent mantle, and therefore the temperature of the metal accreted to the core is lower. However, this effect on mean values is low, with a decrease of only 100 K for $k = 1$, and 50 K for $k = 0.6$, between the minimum equilibrium possible and a full magma ocean equilibration. The effect of k, i.e. metal equilibrium, seems to be more important on the heat content and core temperature (see the range of T^{is}_{CMB} on panels a., b. and c. of Figure 7), which is more discussed in the following section.

Because lowering Δ tends to increase $\overline{P_{eq}}$ during accretion, the output core compositions tend to integrate more light elements as the degree of silicate equilibrium decreases. This is true for both Si and O, with the effect being more important for O than Si. Indeed, the mean values of w_{Si}^{core} for $k = 1$ decreases from 4.8 % wt to 3.9 % wt when Δ increases from 4 to 100 (Figure 7, panel f.); while the mean values of w_{O}^{core} for $k = 1$ (Figure 7, panel i.) decreases from 1.47 to 0.27 % wt when Δ increases from 4 to 100. This shows that the oxygen content of the core is more affected by the mean pressure and type of accretion (higher values of $\overline{P_{eq}}$, a_P and λ for lower Δ, see Figure 5) than Si, despite both reacting the same way to the lack of equilibrium in the silicate phase. This is mainly due to the selection by the models of f_c values between 0.8 and 1, i.e. the majority of accretion process is reduced, thus tends to prevent O from entering the core. This low concentration of O is linked to the parameterization used (Frost et al., 2010; Fischer et al., 2015) which tends to prevent the accretion under oxidizing conditions (as proposed by Siebert et al., 2013). There is also an effect of the law of mass action: O is less available to react than Si even in oxidizing conditions, thus Si tends to enter the core and exclude O. This effect is illustrated in Figure S.2 of Clesi and Deguen (2023). Since the overall concentration of O is low because of it, and the partitioning of O dependent on pressure (Frost et al., 2010), increasing the average pressure of equilibrium counteracts the effect of the reducing conditions. The relative variations in oxygen concentrations appear more clearly as the initial O concentration is lower than Si concentration. Overall, these results show that there is a positive correlation between the heat content and the light elements concentrations in the core that is mediated by the mean pressure of equilibrium during the metal/silicate segregation phase. The mean pressure of equilibrium is inversely proportional to the silicate equilibrium, and therefore decreasing the amount of silicate equilibrated tends to increase both the heat content and light elements content of the core.

4.3.2 Effect of metal equilibrium

The effect of metal equilibrium k on T^{is}_{CMB}, w^{core}_{Si} and w^{core}_{O} for fixed values of Δ (10, 50 and 100) is presented in Figure 8. This figure shows that all the output of the model are less sensitive to the amount of metal equilibrated than the amount of silicate equilibrated (see Figure 7 for comparison). The trends in Figure 8, especially on the mean and median values, are not as clear as the trends that emerges when plotting the same parameteer as a function of Δ. However, one can note that for $\Delta = 10$, increasing k from 0.7 to 1 lead to a decrease of the mean value of w^{core}_{O} from 0.97 to 0.65 % wt (Figure 8, panel g.). This decrease is less important than the one observed when varying Δ for $k = 1$ (Figure 7, panel j.), thus indicating a lower sensitivity of Earth's core oxygen content to the metallic equilibrium than to the silicate equilibrium.

Most of the effect of k lies mostly in the range of possible output: as more metal equilibrates, it is possible to obtain different core compositions and heat contents and still be chemically coherent with the BSE. Indeed, the range of possible T^{is}_{CMB} values widen from a 50 K range (3920 to 3970 K) to a 230 K range (3891 to 4120 K) when k increases from 0.6 to 0.925 and $\Delta = 100$ (Figure 8, panel c.). This widening of the range of solutions is mostly borne by the higher temperature (and concomitantly higher Si and higher O) solutions rather than lower temperature solutions. This relates to the selection in input parameters presented in Figure 6: increasing the value of k allows for solution to happen for lower values of λ, thus increasing the average $\overline{P_{eq}}$ during accretion and consequently the values of T^{is}_{CMB}, w^{core}_{Si} and w^{core}_{O} are increased. Increasing the metal equilibrium therefore allows for models with a steady increase of the magma ocean depth throughout accretion (lower values of λ) to yield chemically coherent models, those models yielding then higher temperatures for their cores. Decreasing the metallic equilibrium tends to select lower temperature solutions. The difficulty of isolating an effect of k on the core composition is due to two competitive phenomenon:

- Decreasing k tends to necessitate an increase in a_P (maximum pressure of equilibrium, see Figure 6) to obtain the right mantle composition, which in turn tends to increase the concentration of Si and O in the core.
- Decreasing k means, by definition, to increase the amount of metal that does not react with the mantle and keeps the same initial composition. Because the initial concentrations of Si and O in the metal are very low, this tends to lower the concentration of Si and O in the core

From our data, it is not possible to distinguish which of the two phenomena takes over. As the range of possibility increases with the values of Δ, which phenomena takes over might be very specific to the value of Δ, a_P and λ. Untangling this question would necessistate further study beyond the scope of this one.

4.4 Quantitative relationship between temperature and chemical equilibrium

Figure 9 shows that the values of CMB temperature decrease with the logarithm of Δ, an effect that is counterbalanced linearly when increasing the value of k. This effect is easier to see for $\overline{T^{is}_{CMB}}$ (middle panel Figure 9), with the highest value of $\overline{T^{is}_{CMB}}$ on the top left corner of the solution space (high k, low Δ) and the lowest values on the bottom right corner of the solution (low k, high Δ). Therefore it is possible to quantify the evolution of the primitive core temperature as a function of Δ and k. In Figure 9, we can summarize the effect of k and Δ to the following equation:

$$T_x = a_x log_{10}\Delta + b_x log_{10} k + c_x \tag{23}$$

where, T_x stands for the minimum, mean or maximum value of T^{is}_{CMB} and a_x, b_x are the fitted parameter (in K) for each temperature, and c_x is the maximum temperature for each dataset, reached for $k = 1$ and $\Delta = 4$, with the error propagated following Supplementary Section S.5. The results of the fit are presented in Table 2. The core temperature dependency with the silicate dilution Δ is higher when most of the metal is equilibrated. This is partly due to the lack of solutions, which tends to skew the value of temperature towards higher Δ values, but is also an effect of

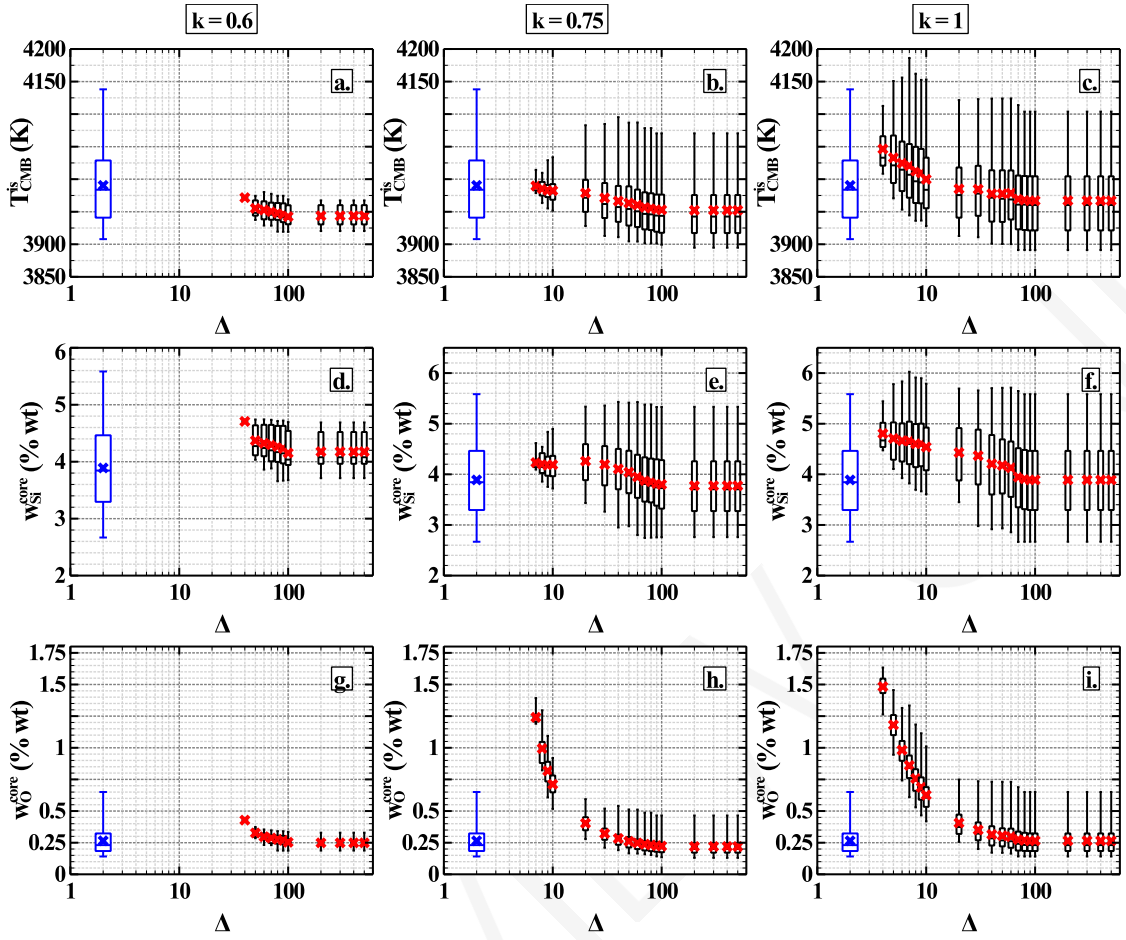

Figure 7: Effect of the silicate dilution Δ on the core properties (isentropic temperature at the CMB, light element content) for different values of k. First row, panels a. to c.: T^{is}_{CMB} in K. Second row, panels d. to f.: w^{core}_{Si} in % wt. Third row, panels g. to i.: w^{core}_{O} in % wt. The left, middle and right column shows the evolution of the parameters values for $k = 0.6$, $k = 0.75$ and $k = 1$, respectively. In each panel the entire solutions range are presented as boxplots, with the red cross being the mean value of the parameter, the white box delimiting the 1st and 3rd quartile, the horizontal line the median value and the vertical lines the minimum and maximum values. The reference model dataset is presented in blue with the same type of plot for comparison at x = 2.

Table 2: Results of the fit for Equation 23 for different values of k. The logarithmic dependency of the different temperature on the Δ and k values is quite clear for the minimum and mean temperature, and less obvious for the maximum temperature.

T_x	a_x	b_x	c_x	R^2
T^{is}_{CMB} min	-73.78 ± 1.16	1.2×10^{-15} ± 16	4033 ± 291	0.76
$\overline{T^{is}_{CMB}}$	-38.74 ± 0.38	143.63 ± 5.35	4046 ± 292	0.96
T^{is}_{CMB} max	-18.68 ± 2.65	753.8 ± 37.42	4186 ± 302	0.53

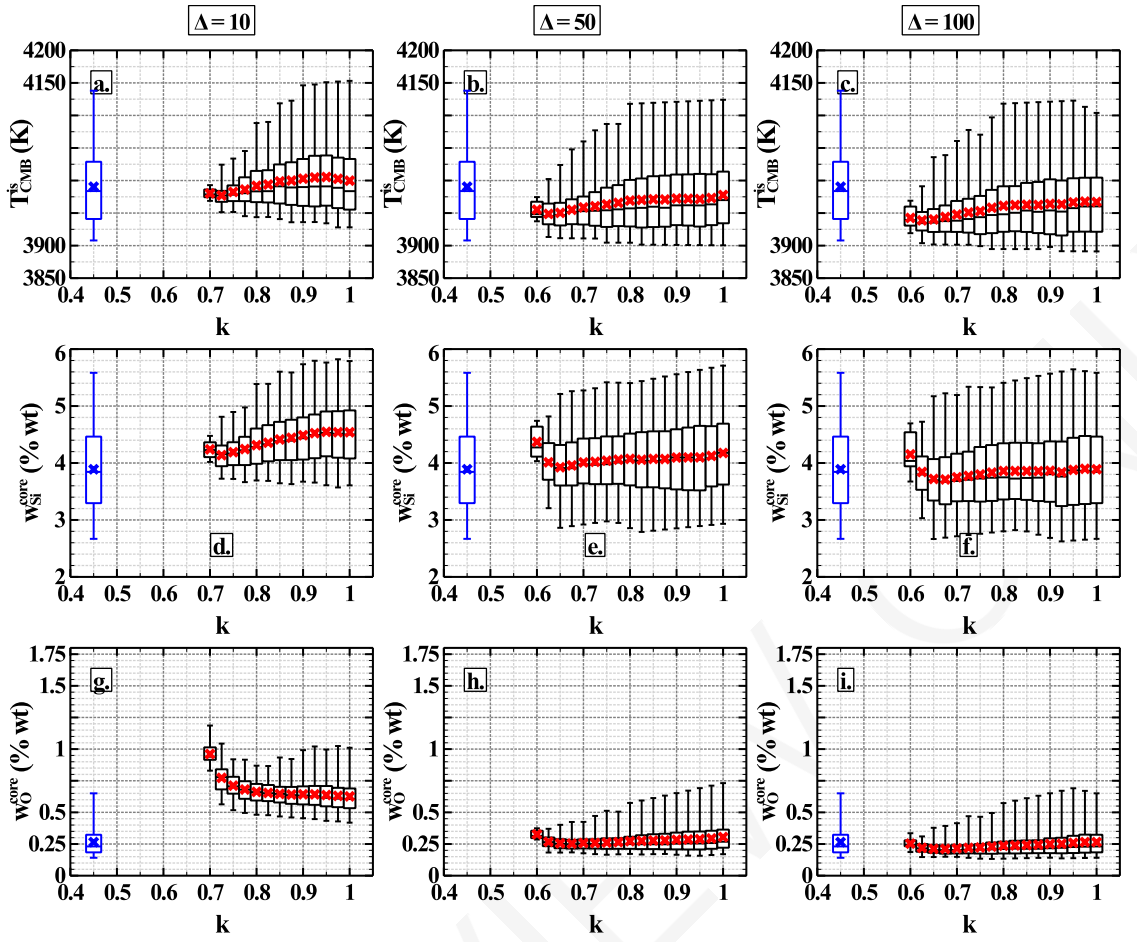

Figure 8: Effect of metal equilibrium k on the core properties (isentropic temperature at the CMB, light element content) for different values of Δ. First row, panels a. to c.: T^{is}_{CMB} in K. Second row, panels d. to f.: w^{core}_{Si} in % wt. Third row, panels g. to i.: w^{core}_{O} in % wt. The left, middle and right column shows the evolution of the parameters values for $\Delta = 10$, $\Delta = 50$ and $\Delta = 100$, respectively. In each panel the entire solutions range are presented as boxplots, with the red cross being the mean value of the parameter, the white box delimiting the 1st and 3rd quartile, the horizontal line the median value and the vertical lines the minimum and maximum values. The reference model dataset is presented in blue with the same type of plot for comparison at x = 2.

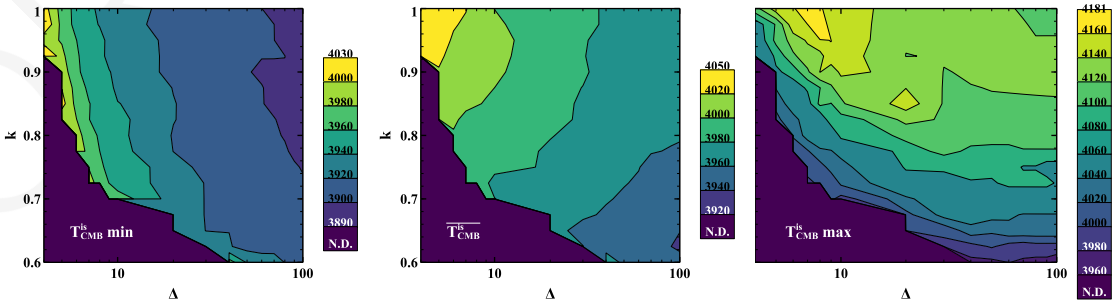

Figure 9: Evolution of minimum (left, $T^{is}_{CMB}min$), mean (center, $\overline{T^{is}_{CMB}}$) and maximum (right, $T^{is}_{CMB}max$) temperature at the CMB after isentropic mixing as a function of k (linear scale) and Δ (log scale). The color scale is changing from panel to panel to account for the different range of values (larger range for the maximum value, narrrower range for mean and minimum values).

the disequilibrium in the metal: as the k is lowered, the temperature decreases but the number of solutions decreases with it. The values given in Table 2 can yield a first approximation on the thermal state of the core for a given model is affected by disequilibrium. Indeed, most partitioning models assume equilibrium of the silicate on large scale (among other examples Rubie et al., 2011; Jacobson et al., 2017; Grewal et al., 2019; Suer et al., 2021; Loroch et al., 2024), due to fast convecting mantle silicate (Höink et al., 2006; Deguen et al., 2014) reacting with falling metallic spheres. These types of models will imply a lower temperature of the primitive core, thus favoring the cold core hypothesis of Nomura et al. (2014), Davies et al. (2015) or Dobrosavljevic et al. (2022) (CMB temperature of $\sim$ 3500 - 4000 K). Studies focusing on the Hf/W partitioning and the moon forming impact (Rudge et al., 2010; Nimmo et al., 2010; Fischer and Nimmo, 2018) tend to yield lower values of metal equilibrium, with values of $k \sim 0.3 - 0.6$, to account for the large size of the last impact. The value of $k = 0.3$ is also taken as a reference value for the sensitivity study of Gu et al. (2023). According to our results, these models will tend to favor also a cold core at the end of accretion: with $k = 0.6$ (higher end of the range proposed by Nimmo et al., 2010), the maximum temperature will be $\sim$ 4000 K for low silicate equilibrium ($\Delta \sim 4$, supposing a solution exists) and $\sim$ 3980 K for full mantle equilibrium according to equation 23. If we consider the mean temperature and not the maximum possible for k=0.6, Equation 23 yields $\overline{T^{is}_{CMB}} \sim 3940$ K for full silicate equilibrium, and $\overline{T^{is}_{CMB}} \sim 3990$ K, even closer to the cold core hypothesis.

On the other hand, some models favor the hot core hypothesis, for instance Andrault et al. (2017) or Driscoll and Davies (2023) (CMB temperatures above 5000 K); and some models tends to favor higher core temperatures right after accretion, for instance King and Olson (2011) who proposed a mechanism allowing a higher intake of gravitational dissipation energy by the metallic phase, thus leading to a hot core right after accretion.

While the cold core hypothesis is easy to explain with classical accretion scenarios such as proposed in this paper, the hot core hypothesis necessitates more hypothesis:

715 if we take the parameters in Table 2, and assume the temperature at the CMB
716 after accretion is the same as the temperature estimated by Andrault et al. (2017,
717 $T_{CMB} = 5000K$), for $k = 1$, no value of Δ can yield this temperature. The
718 closest one are for Δ ranging from 6 and 50 to reach 4000 K at the CMB. Getting
719 high temperatures by disequilibrium alone is therefore not possible, and necessitates
720 other mechanisms which can add more heat to the core: for instance gravitational
721 dissipation energy intake (King and Olson, 2011; Clesi and Deguen, 2023), radiogenic
722 element partitioning (Faure et al., 2020), or a combination of several mechanisms
723 (Driscoll and Davies, 2023). However, what our results show, is that in order to
724 obtain a hot core at the end of accretion, the amount of additional heat added to
725 the core by these processes is lower if there is some chemical disequilibrium, yielding
726 higher concentrations of light elements into the core.

727 ### 4.5 Moon-forming impact: a limitation of the model

728 Our model does not take into account the Moo-forming impact, which is supposed
729 to induce higher disequilibrium degree (Nimmo et al., 2010). Indeed, several models
730 showed that the Moon-forming impact between Theia and the accreting Earth might
731 have lead to extensive melting of the mantle but with a core-merging event, therefore
732 no equilibrium between metal and silicate (Canup, 2004). In a previous study with
733 the same model, we showed that accounting for a Moon-forming impact in the
734 discretization process with full equilibrium does not affect the results of the model
735 (Clesi and Deguen, 2024a). Here, we tested this type of discretization for a few
736 cases, still applying an *a priori* fixed value of k and Δ. The results of those tests
737 are presented in Supplementary section S.2, and Figure S.2 to S.6. For the cases
738 we ran, there are also no effect whatsoever on the output of the model. This means
739 that the conclusion of Clesi and Deguen (2024a) applies alsa for equilibrium rates:
740 as long as k or Δ are not linked to the size of impactors, the results are not changed.
741 This is a limitation of our model: the a *a priori* fixing of parameters tends to erase
742 the specifity of each impactors. A way to improve the model would be to use N-body

simulation results (Rubie et al., 2015), coupled with scaling law for melting (Nakajima et al., 2021), and scaling law for chemical equilibrium (Henningsen et al., 2025, and references therein). This will lead to a better determination of the Moon-forming impact effect on temperature, than the rough approximation presented in this study.

4.6 Advection regimes and decoupling of thermo-chemical equilibrium

As a final note, these results are dependent on the hypothesis that there is a thermal equilibrium of the metal at the bottom of the magma ocean, but not a chemical equilibrium. Indeed, advection regime tends to affect the chemistry and the temperature in the same way (e.g. Deguen et al., 2014; Wacheul and Le Bars, 2018; Clesi et al., 2020, and references therein); it is an equalizing force between the two phenomena. If the advective regime is vigorous and leads to a strong mixing, both temperature and composition will be equilibrated, and diffusion is not the driver of equilibrium. If the advection is less vigorous, and does not mix metal and silicate efficiently, then the difference between diffusion coefficients will make a difference between thermal and chemical equilibrium. Within this scenario, two cases can occur: either the diffusion of temperature happens fast enough to get to full equilibrium, but the chemical diffusion is too slow to reach equilibrium; or the diffusion of temperature happens to slow to compensate for the lack of mixing and then both chemical and thermal equilibrium are fully decoupled. This model assumes mixing is not vigorous enough for to mix both temperature and compositions, and therefore diffusion is the controlling factor. In such a case, the thermal equilibrium is faster than the chemical one. Given that the thermal diffusivity within metallic alloys falls into the range of $\sim 10^{-6}$ $m^2.s^{-1}$ (Monaghan and Quested, 2001; Wilthan et al., 2015); and the chemical diffusivity of the elements within a metallic alloy ranges between $\sim 10^{-9}$ $m^2.s^{-1}$ for Si or O (Posner et al., 2017a,b) to 10^{-8} $m^2.s^{-1}$ for self diffusion of Fe (Dobson, 2002). Therefore, it should be 100 to 1000 times slower than the thermal equilibrium.

5 Conclusions

To conclude, we used a previously developed method to quantify the effect of chemical disequilibrium on the thermal state of the core at the end of accretion. Our model shows that at least 60% of the accreting metallic phase needs to be in equilibrium with the silicate phase. Depending on the amount of metal equilibrated, the dilution factor of the metal in the silicate needs to be >4 if $k = 1$ and >40 if $k = 0.6$. This minimum value of $k = 0.6$ implies a rapid formation of the Earth's core, up to ~50 millions years, according to the Hf-W chronometer's dependency on k as defined by Rudge et al. (2010).

As the degree of equilibrium, in particular in the silicate, is decreased, the average pressure of equilibrium in the magma ocean needs to be increased to obtain a chemically coherent BSE. This increase in the average pressure of equilibrium translates directly into a higher initial core temperature. However, the maximum temperatures obtained from the minimum equilibrium ($T^{is}_{CMB} \sim 4200K$) is not enough to account for the hot core hypothesis, with 800 to 1000 K unaccounted for. Other mechanisms increasing the core temperature are needed to produce a hot core, in particular gravitational heat dissipation.

Further studies are needed in order to fully comprehend the accretion process and the thermal evolution of the early core. In particular, the thermal model must be enhanced to account for more element and better equation of state for the metal.

Enhancing the model, and in particular the implications for the Hf-W age of core formation, will necessitate to link the degree of disequilibrium to the dynamic of metal-silicate segregation throughout the entire process of accretion.

Acknowledgments

This work was supported by the European Research Council (ERC) under the European Unions Horizon 2020 research and innovation programme (grant number 716429). ISTerre is part of Labex OSUG@2020 (ANR10 LABX56).

Data, code, and outputs availability

The initial code used to generate the model from Clesi and Deguen (2023) can be accessed freely at the following link: https://doi.org/10.5281/zenodo.7661374. A tutorial on the chemical part is accessible in the supplementary material of Clesi and Deguen (2024a) (open access) at the following link https://doi.org/10.1016/j.chemgeo.2024.122104. The code used to generate the rest of the figures is available at the following links: https://doi.org/10.5281/zenodo.18940615 and https://doi.org/10.5281/zenodo.21771983. The data used for the figure and the source file for the figures are provided in the supplementary material.

Competing interests

The authors declare no competing interests.

Licence agreement

References

Al'Tshuler, L., Brusnikin, S. and Kuz'Menkov, E. (1987). Isotherms and Grüneisen functions for 25 metals. Journal of Applied Mechanics and Technical Physics 28: 129–141.

Andrault, D., Bolfan-Casanova, N., Bouhifd, M., Boujibar, A., Garbarino, G., Manthilake, G., Mezouar, M., Monteux, J., Parisiades, P. and Pesce, G. (2017). Toward a coherent model for the melting behavior of the deep earth's mantle. Physics of the Earth and Planetary Interiors 265: 67–81.

Andrault, D., Bolfan-Casanova, N., Nigro, G. L., Bouhifd, M. A., Garbarino, G. and Mezouar, M. (2011). Solidus and liquidus profiles of chondritic mantle: Implication for melting of the Earth across its history. Earth and planetary science letters 304: 251–259.

Birch, F. (1965). Energetics of core formation. Journal of Geophysical research 70: 6217–6221.

Bouhifd, M. and Jephcoat, A. (2011). Convergence of Ni and Co metal–silicate partition coefficients in the deep magma-ocean and coupled silicon–oxygen solubility in iron melts at high pressures. Earth and Planetary Science Letters 307: 341–348.

Bouhifd, M. A., Gautron, L., Bolfan-Casanova, N., Malavergne, V., Hammouda, T., Andrault, D. and Jephcoat, A. (2007). Potassium partitioning into molten iron alloys at high-pressure: Implications for Earth's core. Physics of the Earth and Planetary Interiors 160: 22–33.

Canup, R. M. (2004). Simulations of a late lunar-forming impact. Icarus 168: 433–456.

Clesi, V., Bouhifd, M., Bolfan-Casanova, N., Manthilake, G., Fabbrizio, A. and Andrault, D. (2016). Effect of H2O on metal–silicate partitioning of Ni, Co, V, Cr, Mn and Fe: Implications for the oxidation state of the Earth and Mars. Geochimica et Cosmochimica Acta 192: 97–121.

Clesi, V. and Deguen, R. (2023). Linking the core heat content to earth's accretion history. Geochemistry, Geophysics, Geosystems 24: e2022GC010661. doi:https://doi.org/10.1029/2022GC010661.

Clesi, V. and Deguen, R. (2024a). Effect of discretization choices when modeling the thermo-chemical history of the accreting core. Chemical Geology 657: 122104.

Clesi, V. and Deguen, R. (2024b). Grüneisen parameter formalism in the study of the earth's core formation: a sensitivity study. Geophysical Journal International 237: 1275–1284.

Clesi, V., Monteux, J., Qaddah, B., Le Bars, M., Wacheul, J.-B. and Bouhifd, M. A. (2020). Dynamics of core-mantle separation: Influence of viscosity contrast and metal/silicate partition coefficients on the chemical equilibrium. Physics of the Earth and Planetary Interiors 306: 106547.

Davies, C., Pozzo, M., Gubbins, D. and Alfe, D. (2015). Constraints from material properties on the dynamics and evolution of earth's core. Nature Geoscience 8: 678–685.

Deguen, R., Landeau, M. and Olson, P. (2014). Turbulent metal–silicate mixing, fragmentation, and equilibration in magma oceans. Earth and Planetary Science Letters 391: 274–287.

Dobrosavljevic, V. V., Zhang, D., Sturhahn, W., Zhao, J., Toellner, T. S., Chariton, S., Prakapenka, V. B., Pardo, O. S. and Jackson, J. M. (2022). Melting and phase relations of fe-ni-si determined by a multi-technique approach. Earth and Planetary Science Letters 584: 117358.

Dobson, D. P. (2002). Self-diffusion in liquid fe at high pressure. Physics of the Earth and Planetary Interiors 130: 271–284.

Drake, M. J. and Righter, K. (2002). Determining the composition of the Earth. Nature 416: 39–44.

Driscoll, P. and Davies, C. (2023). The "new core paradox:" challenges and potential solutions. Journal of Geophysical Research: Solid Earth : e2022JB025355.

Dziewonski, A. M. and Anderson, D. L. (1981). Preliminary reference Earth model. Physics of the earth and planetary interiors 25: 297–356.

Faure, P., Bouhifd, M. A., Boyet, M., Manthilake, G., Clesi, V. and Devidal, J.-L. (2020). Uranium and thorium partitioning in the bulk silicate Earth and the oxygen content of Earth's core. Geochimica et Cosmochimica Acta 275: 83–98.

Fiquet, G., Auzende, A., Siebert, J., Corgne, A., Bureau, H., Ozawa, H. and Garbarino, G. (2010). Melting of peridotite to 140 gigapascals. Science 329: 1516–1518.

Fischer, R. A., Campbell, A. J. and Ciesla, F. J. (2017). Sensitivities of earth's core and mantle compositions to accretion and differentiation processes. Earth and Planetary Science Letters 458: 252–262.

Fischer, R. A., Nakajima, Y., Campbell, A. J., Frost, D. J., Harries, D., Langenhorst, F., Miyajima, N., Pollok, K. and Rubie, D. C. (2015). High pressure metal–silicate partitioning of Ni, Co, V, Cr, Si, and O. Geochimica et Cosmochimica Acta 167: 177–194.

Fischer, R. A. and Nimmo, F. (2018). Effects of core formation on the hf–w isotopic composition of the earth and dating of the moon-forming impact. Earth and planetary science letters 499: 257–265.

Frost, D. J., Asahara, Y., Rubie, D. C., Miyajima, N., Dubrovinsky, L. S., Holzapfel, C., Ohtani, E., Miyahara, M. and Sakai, T. (2010). Partitioning of oxygen between the Earth's mantle and core. Journal of Geophysical Research: Solid Earth 115.

Geßmann, C. K. and Rubie, D. C. (1998). The effect of temperature on the partitioning of nickel, cobalt, manganese, chromium, and vanadium at 9 gpa and constraints on formation of the earth's core. Geochimica et Cosmochimica Acta 62: 867–882.

Grewal, D. S., Dasgupta, R., Sun, C., Tsuno, K. and Costin, G. (2019). Delivery of carbon, nitrogen, and sulfur to the silicate Earth by a giant impact. Science advances 5: eaau3669.

Gu, J. T., Fischer, R. A., Brennan, M. C., Clement, M. S., Jacobson, S. A., Kaib, N. A., O'Brien, D. P. and Raymond, S. N. (2023). Comparisons of the core and mantle compositions of earth analogs from different terrestrial planet formation scenarios. Icarus 394: 115425.

Henningsen, E. L., Korenaga, J. and Marchi, S. (2025). Impact-driven redox stratification of earth's mantle. Journal of Geophysical Research: Solid Earth 130: e2024JB030817.

Höink, T., Schmalzl, J. and Hansen, U. (2006). Dynamics of metal-silicate separation in a terrestrial magma ocean. Geochemistry, Geophysics, Geosystems 7.

Izidoro, A., Bitsch, B. and Dasgupta, R. (2021). The effect of a strong pressure bump in the Sun's natal disk: terrestrial planet formation via planetesimal accretion rather than pebble accretion. The Astrophysical Journal 915: 62.

Jacobson, S. A., Rubie, D. C., Hernlund, J., Morbidelli, A. and Nakajima, M. (2017). Formation, stratification, and mixing of the cores of Earth and Venus. Earth and Planetary Science Letters 474: 375–386.

King, C. and Olson, P. (2011). Heat partitioning in metal-silicate plumes during Earth differentiation. Earth and Planetary Science Letters 304: 577–586.

Landeau, M., Deguen, R., Phillips, D., Neufeld, J. A., Lherm, V. and Dalziel, S. B. (2021). Metal-silicate mixing by large Earth-forming impacts. Earth and Planetary Science Letters 564: 116888.

Loroch, D., Hackler, S., Rohrbach, A., Berndt, J. and Klemme, S. (2024). Accretion and core formation of earth-like planets: Insights from metal–silicate partitioning of siderophile and volatile elements. Geosciences 14: 281.

McDonough, W. and Sun, S.-S. (1995). The composition of the Earth. Chemical geology 120: 223–253.

Monaghan, B. and Quested, P. (2001). Thermal diffusivity of iron at high temperature in both the liquid and solid states. ISIJ international 41: 1524–1528.

Monteux, J., Ricard, Y., Coltice, N., Dubuffet, F. and Ulvrova, M. (2009). A model of metal–silicate separation on growing planets. Earth and Planetary Science Letters 287: 353–362.

907 Morard, G., Siebert, J., Andrault, D., Guignot, N., Garbarino, G., Guyot, F. and Antonangeli, D.
908 (2013). The Earth's core composition from high pressure density measurements of liquid iron
909 alloys. Earth and Planetary Science Letters 373: 169–178.

910 Morbidelli, A., Chambers, J., Lunine, J., Petit, J.-M., Robert, F., Valsecchi, G. and Cyr, K. (2000).
911 Source regions and timescales for the delivery of water to the Earth. Meteoritics & Planetary
912 Science 35: 1309–1320.

913 Nakajima, M., Golabek, G. J., Wünnemann, K., Rubie, D. C., Burger, C., Melosh, H. J., Jacobson,
914 S. A., Manske, L. and Hull, S. D. (2021). Scaling laws for the geometry of an impact-induced
915 magma ocean. Earth and Planetary Science Letters 568: 116983.

916 Nimmo, F., O'brien, D. and Kleine, T. (2010). Tungsten isotopic evolution during late-stage accretion:
917 constraints on earth–moon equilibration. Earth and Planetary Science Letters 292: 363–370.

918 Nomura, R., Hirose, K., Uesugi, K., Ohishi, Y., Tsuchiyama, A., Miyake, A. and Ueno, Y. (2014). Low
919 core-mantle boundary temperature inferred from the solidus of pyrolite. Science 343: 522–525.

920 Posner, E. S., Rubie, D. C., Frost, D. J. and Steinle-Neumann, G. (2017a). Experimental
921 determination of oxygen diffusion in liquid iron at high pressure. Earth and Planetary Science
922 Letters 464: 116–123.

923 Posner, E. S., Rubie, D. C., Frost, D. J., Vlček, V. and Steinle-Neumann, G. (2017b). High p–t
924 experiments and first principles calculations of the diffusion of si and cr in liquid iron. Geochimica
925 et Cosmochimica Acta 203: 323–342.

926 Pu, C., Gao, X., Wu, Z., Du, Z. and Jing, Z. (2025). Metal-silicate partitioning of si, o, and mg at
927 high pressures and high temperatures: Implications to the compositional evolution of core-forming
928 metallic melts. Geochemistry, Geophysics, Geosystems 26: e2024GC011940.

929 Raymond, S. N., O'Brien, D. P., Morbidelli, A. and Kaib, N. A. (2009). Building the terrestrial planets:
930 Constrained accretion in the inner Solar System. Icarus 203: 644–662.

931 Rubie, D., Frost, D., Mann, U., Asahara, Y., Nimmo, F., Tsuno, K., Kegler, P., Holzheid, A. and
932 Palme, H. (2011). Heterogeneous accretion, composition and core–mantle differentiation of the
933 Earth. Earth and Planetary Science Letters 301: 31–42.

934 Rubie, D., Jacobson, S., Morbidelli, A., O'Brien, D., Young, E., Vries, J. de, Nimmo, F., Palme, H.
935 and Frost, D. (2015). Accretion and differentiation of the terrestrial planets with implications for
936 the compositions of early-formed Solar System bodies and accretion of water. Icarus 248: 89–108.

Rubie, D., Melosh, H., Reid, J., Liebske, C. and Righter, K. (2003). Mechanisms of metal–silicate equilibration in the terrestrial magma ocean. Earth and Planetary Science Letters 205: 239–255.

Rudge, J. F., Kleine, T. and Bourdon, B. (2010). Broad bounds on earth's accretion and core formation constrained by geochemical models. Nature Geoscience 3: 439–443.

Samuel, H. (2012). A re-evaluation of metal diapir breakup and equilibration in terrestrial magma oceans. Earth and Planetary Science Letters 313: 105–114.

Samuel, H., Tackley, P. and Evonuk, M. (2010). Heat partitioning in terrestrial planets during core formation by negative diapirism. Earth and Planetary Science Letters 290: 13–19.

Sanloup, C., Guyot, F., Gillet, P., Fiquet, G., Mezouar, M. and Martinez, I. (2000). Density measurements of liquid Fe-S alloys at high-pressure. Geophysical Research Letters 27: 811–814.

Siebert, J., Badro, J., Antonangeli, D. and Ryerson, F. J. (2012). Metal–silicate partitioning of Ni and Co in a deep magma ocean. Earth and Planetary Science Letters 321: 189–197.

Siebert, J., Badro, J., Antonangeli, D. and Ryerson, F. J. (2013). Terrestrial accretion under oxidizing conditions. Science 339: 1194–1197.

Suer, T.-A., Siebert, J., Remusat, L., Day, J. M., Borensztajn, S., Doisneau, B. and Fiquet, G. (2021). Reconciling metal–silicate partitioning and late accretion in the earth. Nature Communications 12: 2913.

Ulvrová, M., Coltice, N., Ricard, Y., Labrosse, S., Dubuffet, F., Velímskỳ, J. and Šrámek, O. (2011). Compositional and thermal equilibration of particles, drops and diapirs in geophysical flows. Geochemistry Geophysics Geosystems 12: 1–11.

Wacheul, J.-B. and Le Bars, M. (2018). Experiments on fragmentation and thermo-chemical exchanges during planetary core formation. Physics of the Earth and Planetary Interiors 276: 134–144.

Wade, J. and Wood, B. J. (2005). Core formation and the oxidation state of the earth. Earth and Planetary Science Letters 236: 78–95.

Walsh, K. J., Morbidelli, A., Raymond, S. N., O'Brien, D. P. and Mandell, A. M. (2011). A low mass for mars from jupiter's early gas-driven migration. Nature 475: 206–209.

Wasson, J. T. and Kallemeyn, G. W. (1988). Compositions of chondrites. Philosophical Transactions of the Royal Society of London. Series A, Mathematical and Physical Sciences 325: 535–544.

966 Wilthan, B., Schützenhöfer, W. and Pottlacher, G. (2015). Thermal diffusivity and thermal
967 conductivity of five different steel alloys in the solid and liquid phases. International Journal of
968 Thermophysics 36: 2259–2272.

969 Wood, B., Wade, J. and Kilburn, M. (2008). Core formation and the oxidation state of the Earth:
970 Additional constraints from Nb, V and Cr partitioning. Geochimica et Cosmochimica Acta 72:
971 1415–1426.

972 Zhang, D., Jackson, J. M., Zhao, J., Sturhahn, W., Alp, E. E., Hu, M. Y., Toellner, T. S., Murphy,
973 C. A. and Prakapenka, V. B. (2016). Temperature of Earth's core constrained from melting of Fe
974 and Fe0. 9Ni0. 1 at high pressures. Earth and Planetary Science Letters 447: 72–83.

Supplementary information to "Determining the core temperature at the end of accretion: effect of chemical disequilibrium during metal-silicate partitioning"

Vincent Clesi[1,2] **and Renaud Deguen**[2,3]

[1]**Insitut für Mineralogie, Münster Universität, Correnstraße 24, 48149 Münster**
[2]**Univ Lyon, ENSL, UCBL, UJM, CNRS, LGL-TPE, F-69007 Lyon, France**
[3]**Univ. Grenoble Alpes, Univ. Savoie Mont Blanc, CNRS, IRD, Univ. Gustave Eiffel, ISTerre, 38000 Grenoble, France**

ABSTRACT

This is the supplementary figures for the paper entitled 'Determining the core temperature at the end of accretion: effect of chemical disequilibrium during metal-silicate partitioning'. Most of the figure are the final concentrations of each element in the mantle and the core (Fig. S4 to S19). Five sections has been added to tests the limits of the model: effect of liquidus temperature (S.1), effect of Moon-forming impact (S.2), sensitivity of the number of solution to the definition of a solution (S.3), sensitivity of the number of solutions to the number of scenarios tested (S.4), estimation of the error on the final temperature (S.5)

Keywords: Accretion model, Core temperature, metal silicate partitioning

S.1 CHOICE OF LIQUIDUS TEMPERATURE

The liquidus temperature is that of Andrault et al. (2011), as it was used in the original study of Fischer et al. (2015) whose parameterization has been used in our chemical model. This liquidus is calibrated for chondritic composition, which we used in the model. Therefore, this liquidus seems to be appropriate for our models, especially that it allows for comparison with our previous study (Clesi and Deguen, 2023), and other studies that use the same liquidus (e.g., Boujibar et al., 2014; Fischer et al., 2015). However, as the liquidus temperature is the first temperature anchoring the subsequent evolution, chosing another liquidus or a temperature between solidus and liquidus will change the absolute values. A proper study of this effect is necessary, and this section is a first attempt to give hint on how this study should look like. Indeed, we did try to use the Fiquet et al. (2010) liquidus instead, so as to estimate the effect from the other side of the spectrum. This new temperature is given by equation:

$$T_{eq} = 2803 \pm 432 \left(\frac{P_{eq}}{35 \pm 44} + 1 \right)^{\frac{1}{2.41 \pm 0.99}} \tag{S.1}$$

which is the same as Equation (1) in the main text, with slightly different parameter. Unfortunately, running test with this temperature of equilibrium did not yield any results for k = 1, 0.6, 0.5 and 0.1 (all Δ tested). This indicates that choosing the liquidus for the magma ocean cannot be made without taking into account the parameterization of partitioning. Indeed, the parameterization used for this study has been calibrated for compositions and temperatures that are close to the Andrault et al. (2011) liquidus, and therefore makes it possible to obtain solutions. As soon as a hot liquidus has been chosen, the parameterization became

invalid (no solutions could be found). Therefore, studying the effect of equilibrium temperature needs to be coupled with studying the effect of the parameterization to be impactful. Nonetheless, since we did not obtain chemically coherent solutions with the liquidus presented in Eq. (S.1), and still wanted to analyze the effect of changing the initial temperature on the final results, and especially how the relationship between T^{is}_{CMB} and k, Δ variations are affected, we calculated the compositions using Andrault et al. (2011) (Equation (1) in the main text) and the temperature using as initial temperature of the metal given by Equation (S.1). This lead to a decoupling of the chemical and thermal part of the model, but do allow for an estimation of the effect of the initial temperature on the final heat content. We tested this for $k = 0.6$, 0.75 and 1 and the full range of Δ. The results compared to the main text are presented in Figure S.1.

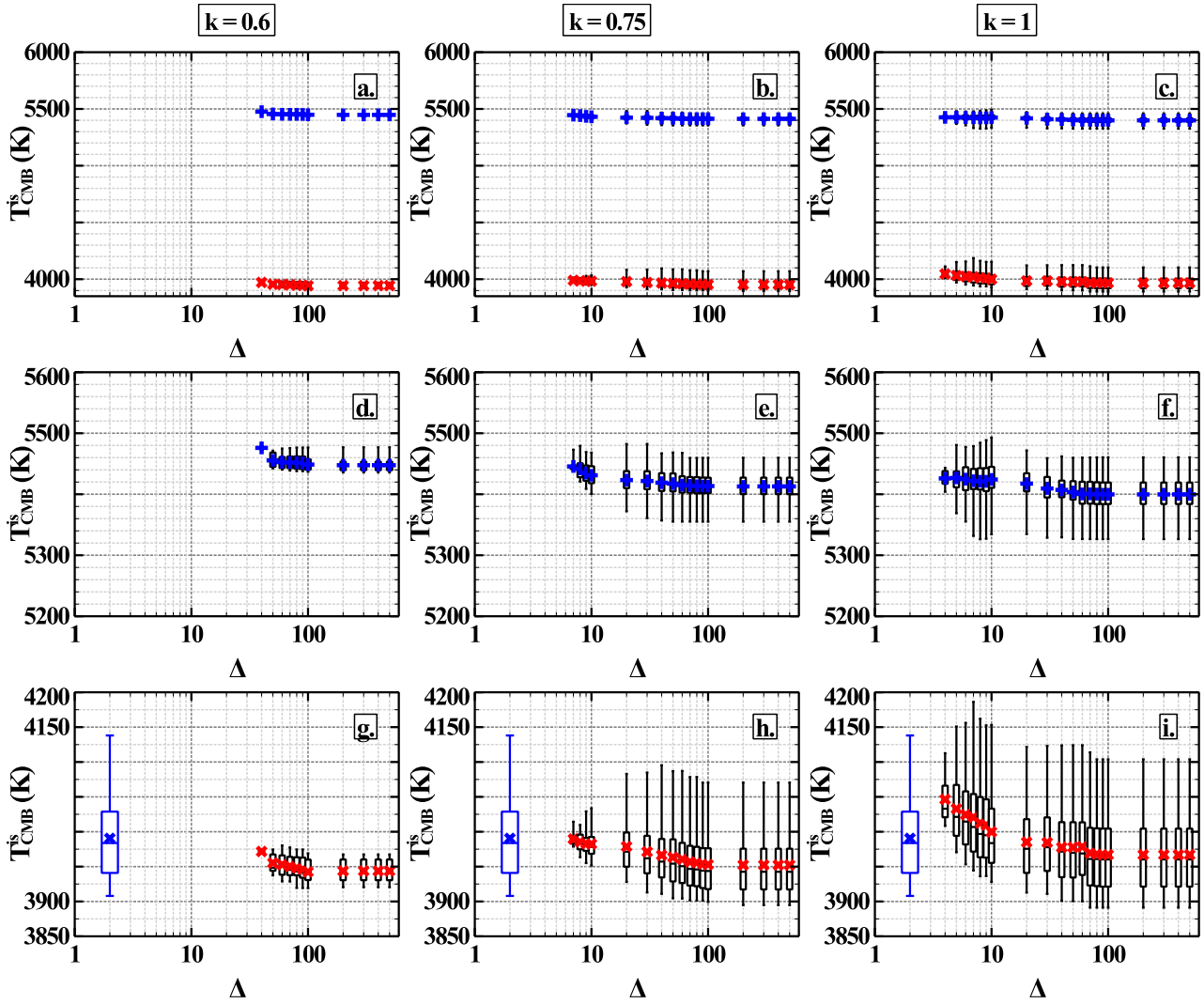

Figure S.1. Temperature output (T^{is}_{CMB}) using Fiquet et al. (2010) liquidus (blue cross) and using Andrault et al. (2011) liquidus (red crosses) for different values of k. Panels a to c: comparison of the results on the same plot. Panels d to f: Results only with Fiquet et al. (2010) liquidus. Panels g to i: Initial results presented in the main text.

These figures shows that increasing the initial temperature of the metal tends to transpose the results to higher temperature, but with a similar effect of at least Δ, and most probably k (only 3 values were tested,

but the trend is similar to that of Figure 7 and 8 in the main text). The range of output is within 400 K for both liquidus models, and the variability is lower for Fiquet et al. (2010) liquidus. However, this is for a decoupled chemical and thermal model, meaning the initial temperature is very high and the subsequent compression is not realistic and small since it is calibrated for a lower liquidus, thus inducing less changes in the temperature of the metal, and therefore explaining the flatter trend observed here. There is still a trend, the high values of Δ tend to yield lower mean values than lower values of Δ: this is particularly visible in panel f of Figure S.1.

To conclude on this matter: the initial temperature does not change the trend of variability with k or Δ, but changes the absolute values of T^{is}_{CMB}, all things kept equal. Unfortunately, keeping the link between temperature and composition will necessitate to not keep things equal, and therefore change the initial composition of impactor, the parameterization of partitioning and the overall outputs. A proper study of this effect will have to take be performed to properly estimate the effect of T_{eq} on the final T^{is}_{CMB}.

S.2 MOON-FORMING IMPACT MODELING

To model the Moon-forming impact, we modified the discretization of our model to match the model C20+T described in Clesi and Deguen (2024a). With this modification, the last 10% of accretion happen in one step, thus modeling the mass accreted by a Moon-forming impact (Canup, 2004). We did not include a specific parameterization of the value of k and Δ, using existing parameterization for giant-impacts(Deguen et al., 2014; Landeau et al., 2016; Nakajima et al., 2021; Landeau et al., 2021). We also did not add a specific model of thermo-chemical accretion for Theia, which would have change both composition and thermal state of Theia's core. In the case of the core-merging scenarios (Landeau et al., 2016; Zhou et al., 2022), both variables should change the final temperature and composition of the core. With these caveats in mind, we ran the models using the C20+T discretization to compare in a first-approximation what would be the effect of a final giant impact for k = 0.6, 0.75 and 1 and all values of Δ. The number of solutions is roughly the same (a little bit below those presented in the main text). The average values of inputs Parameters (a_P,f_c,λ) and the average value of the resulting $\overline{P_{eq}}$ are presented for $\Delta = 100$ in Figure S.2 and for $\Delta = 50$ in Figure S.3, in comparison with the initial model presented in the main text. The output temperatures T^{is}_{CMB}, Si and O concentrations of the core are presented in Figure S.4 and Figure S.5 for $\Delta = 100$ and $\Delta = 50$, respectively. Finally, the effect of Δ on the temperature for Theia-like discretization for k=0.6, 0.75 and 1 is presented in Figure S.6.

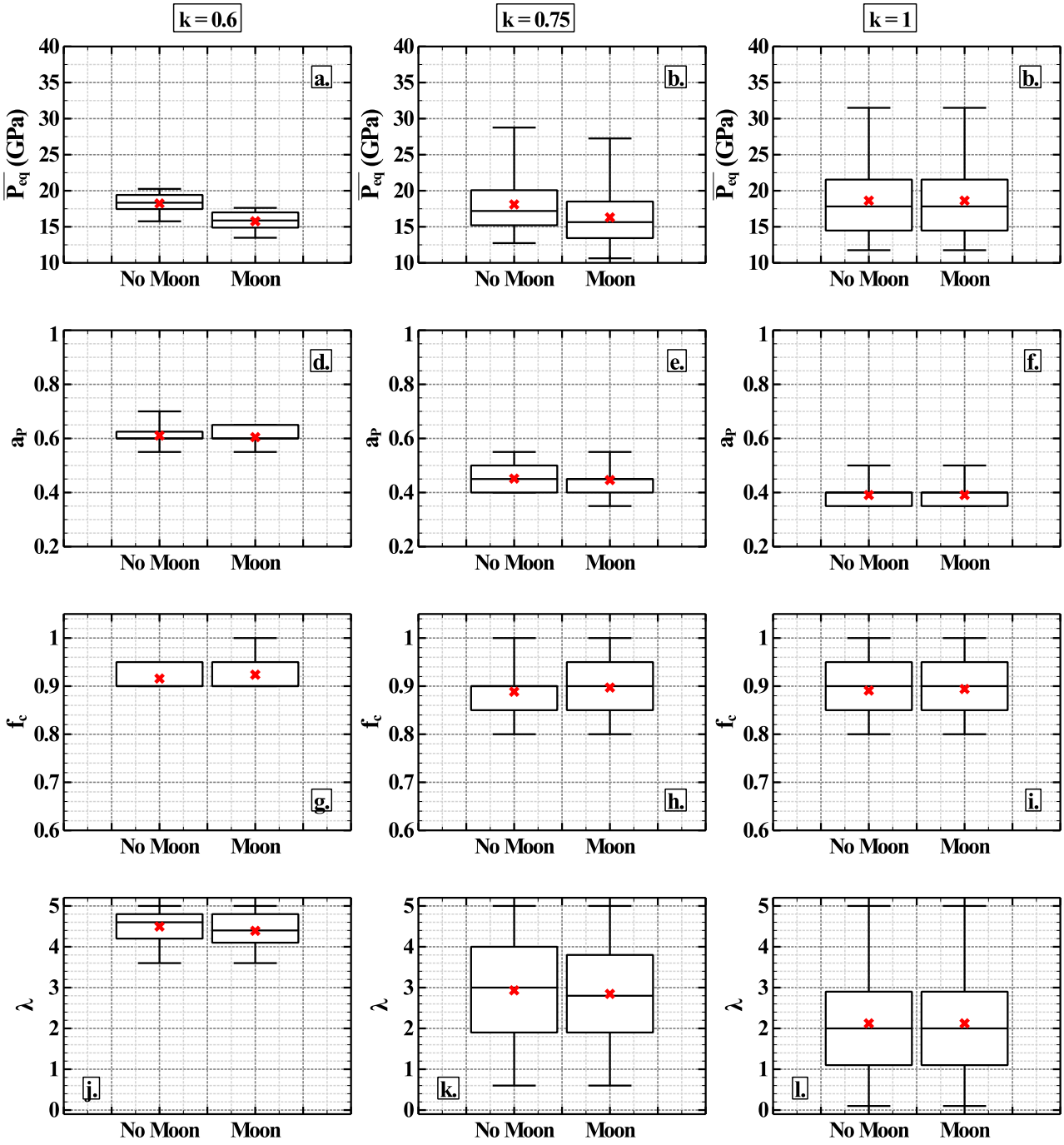

Figure S.2. Comparison of input parameters between the main text model, and the model including a Moon-forming impact (No Moon and Moon) for $\Delta = 100$ and $k = 0.6$ (panels a., d., g. and j.), 0.75 (panels b., e., h. and k.) and 1 (panels c., f., i. and l.)

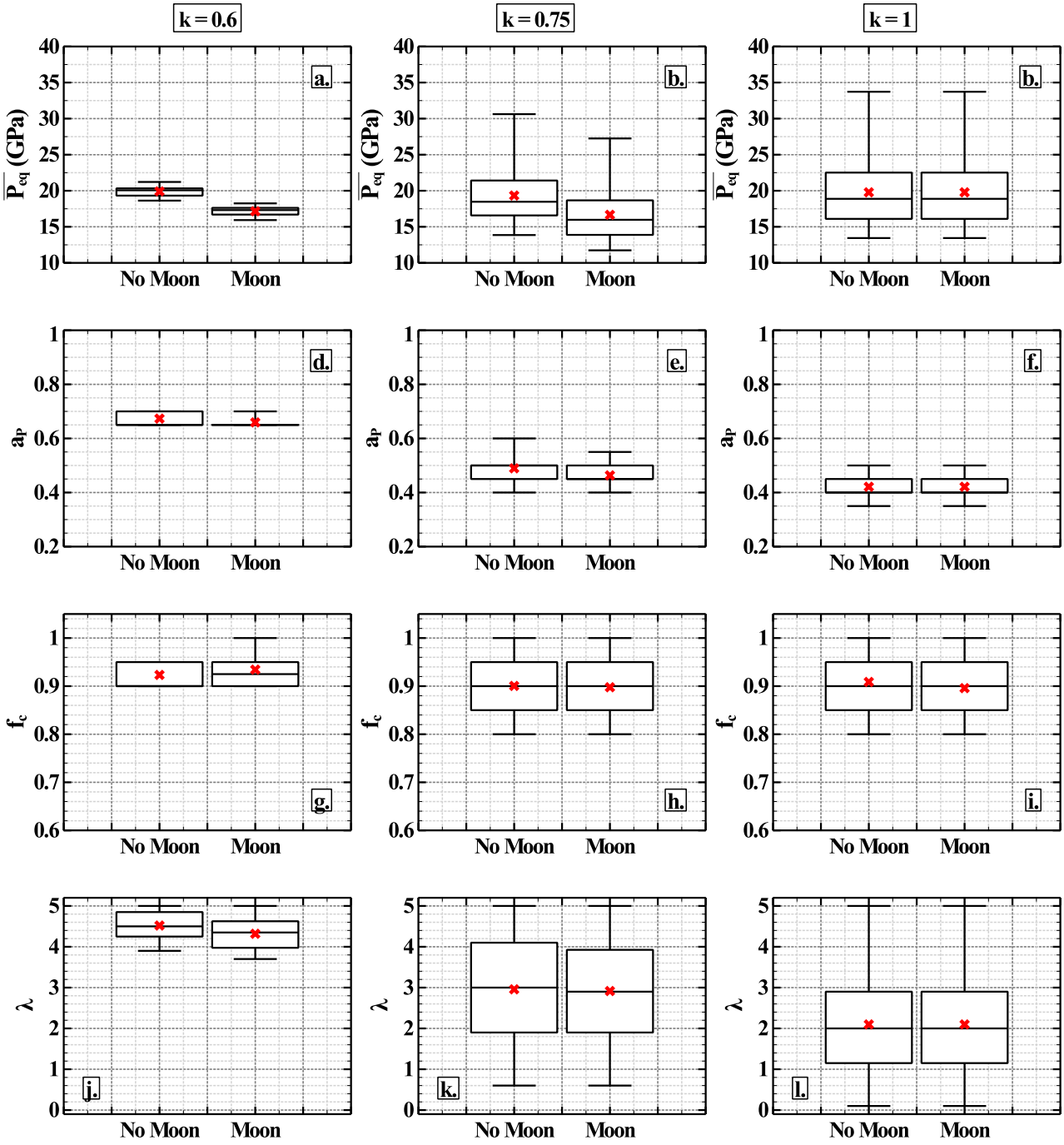

Figure S.3. Comparison of input parameters between the main text model, and the model including a Moon-forming impact (No Moon and Moon) for $\Delta = 50$ and $k = 0.6$ (panels a., d., g. and j.), 0.75 (panels b., e., h. and k.) and 1 (panels c., f., i. and l.)

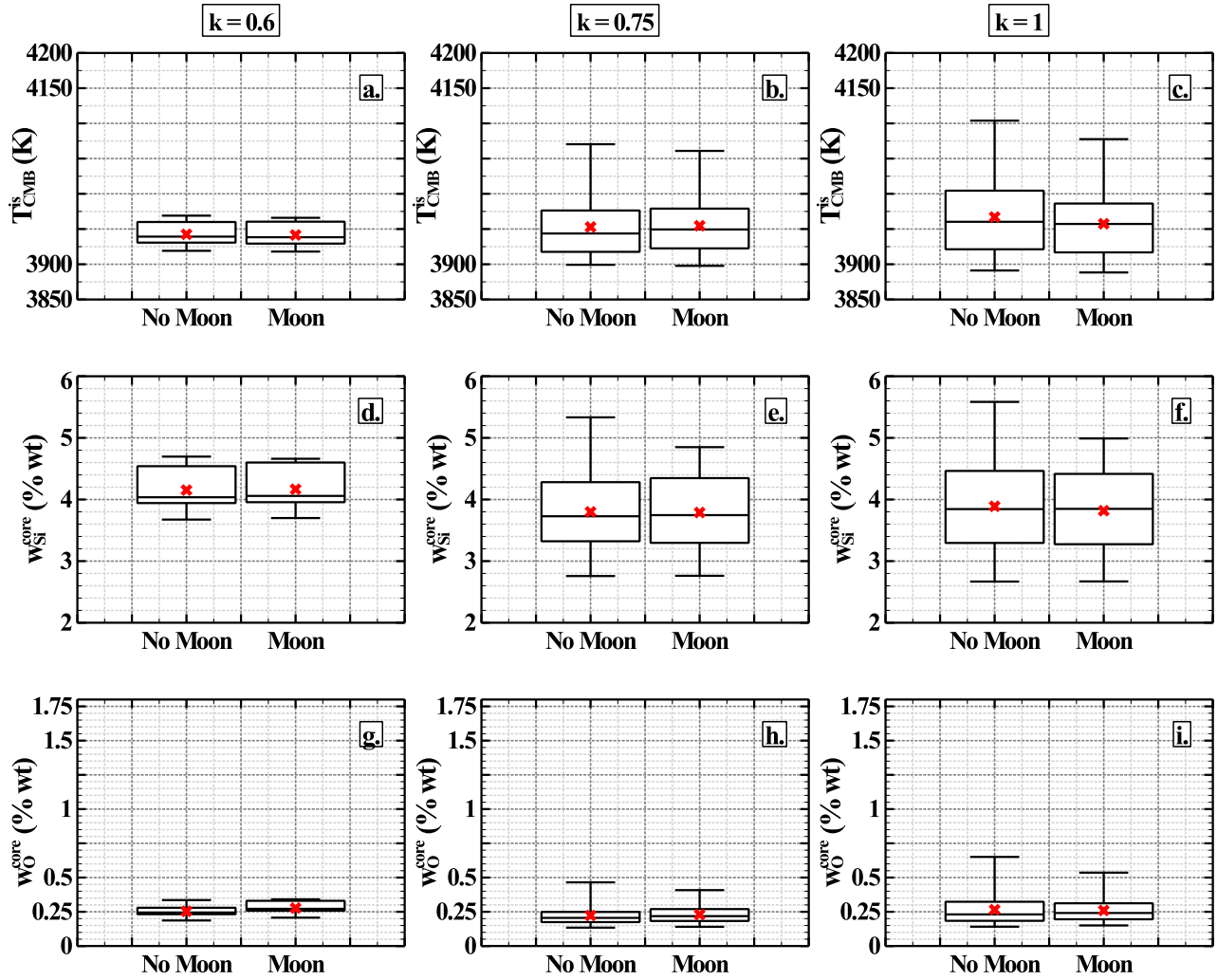

Figure S.4. Comparison of output parameters between the main text model, and the model including a Moon-forming impact (No Moon and Moon) for $\Delta = 100$ and $k = 0.6$ (panels a., d. and g.), 0.75 (panels b., e. and h.) and 1 (panels c., f., i).

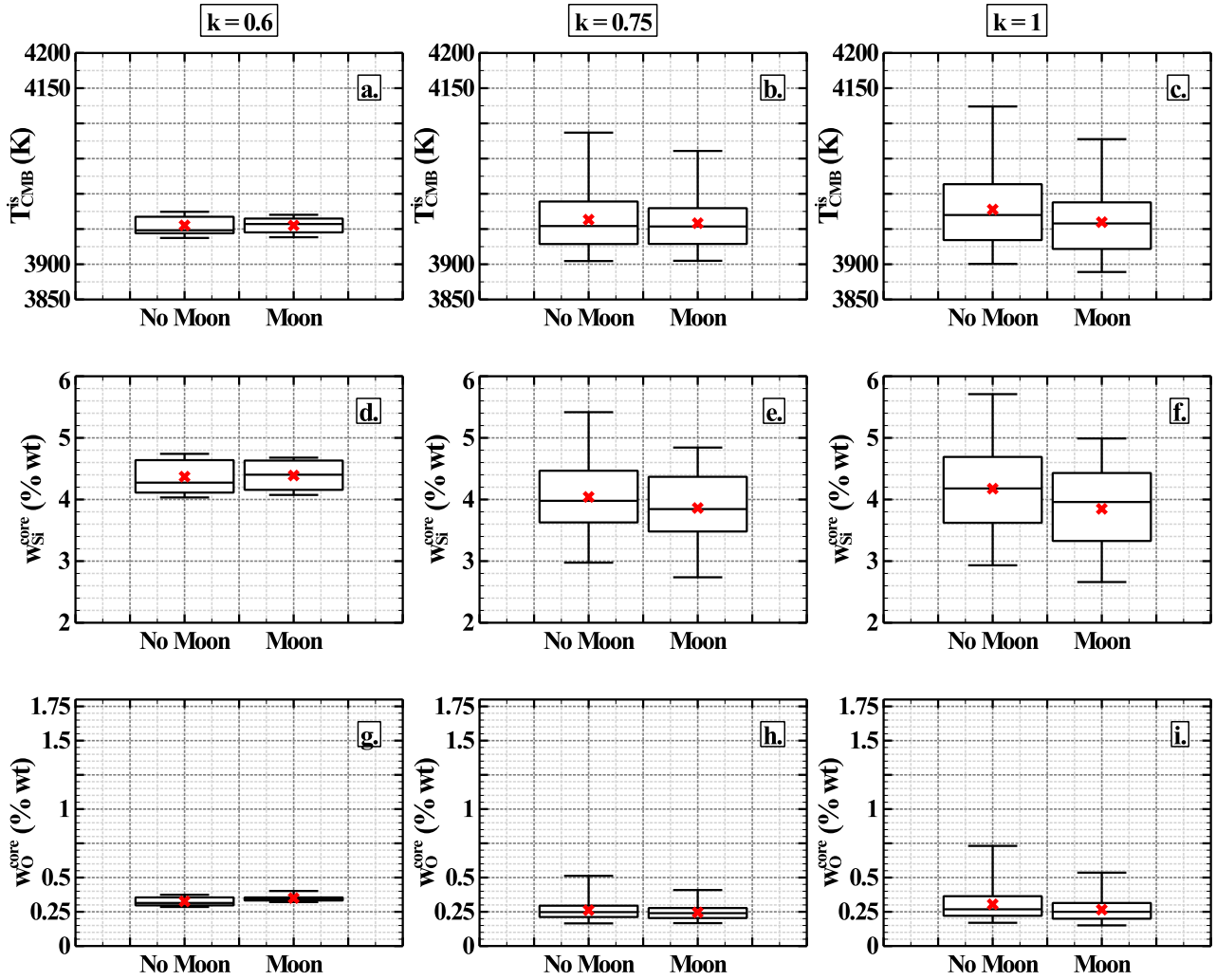

Figure S.5. Comparison of output parameters between the main text model, and the model including a Moon-forming impact (No Moon and Moon) for $\Delta = 50$ and $k = 0.6$ (panels a., d. and g.), 0.75 (panels b., e. and h.) and 1 (panels c., f., i).

As can be seen on Figures S.2 to S.6, the effect of varying the discretization and nothing else does not change the output of the models significantly: the maximum T^{is}_{CMB} is 50 K below the initial model, but average and minimum are unchanged. The trend of increasing temperature with decreasing equilibrium rate is unchanged (Figure S.6).

This confirms the result of Clesi and Deguen (2024a) that discretization by itself does not change the results of accretion model as long as at least 10 steps are taken into account.

A proper way of improving the model would be:

- Link the discretization to scaling law for melting (Nakajima et al., 2021)
- Calculate the value of k and Δ for each impact (Deguen et al., 2014; Landeau et al., 2021)
- In parallel, model the thermo-chemical evolution of Theia, and define its effect, for instance core-merging (Landeau et al., 2017; Canup et al., 2023; Zhou et al., 2022)

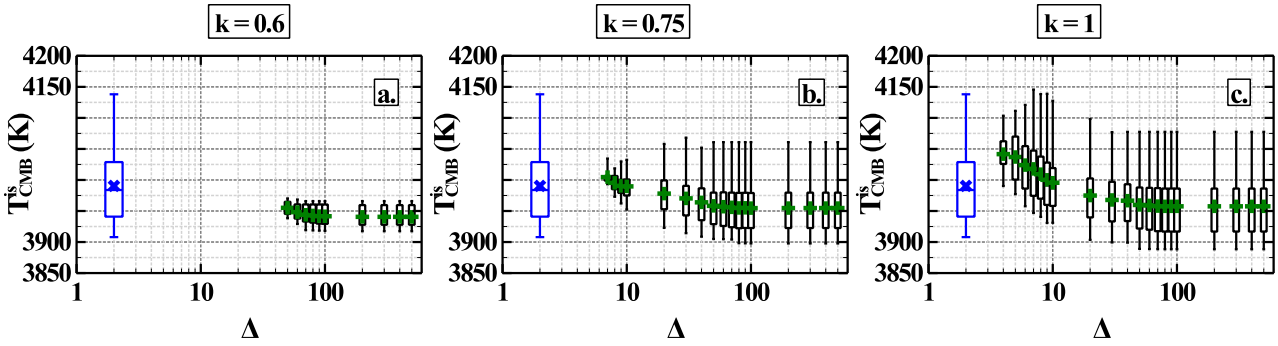

Figure S.6. Effect of Δ on output temperature T^{is}_{CMB} for k = 0.6, 0.75 and 1 (panels a, b and c, respectively). The blue box at x=2 is the reference model as defined in the main text. The green cross shows the mean values.

- Link the discretization to a variation in the composition of the impactor:for instance: small impactor masses with less metal and more reduced composition, and bigger impactor masses being both more oxidized and oxidizing (Henningsen et al., 2025)
- Apply all the previous step to a successful N-body simulation (Jacobson et al., 2017; Rubie et al., 2015)

In the end, our model does correctly predict the BSE composition and can be used as first estimation of the thermo-chemical evolution of the Earth, but does not accurately model the strong impact that the Moon formation is believed to have on core formation (Nimmo et al., 2010; Rudge et al., 2010).

Therefore the values of k and Δ proposed in our stud should serve as a general approximation of the average degree of equilibrium throughout the accretion necessary to obtain the BSE, but do not apply to a specific part of the accretion process.

S.3 EFFECT OF FILTER SIZE ON THE MODEL'S OUTPUTS

In Figure 4 of the main text, we show that no solution exists for $k < 0.6$, thus increasing the accepted minimum equilibrium degree of the metal derived from Hf-W study of $k \sim 0.3$ (Rudge et al., 2010; Gu et al., 2023). This should be sensitive to how we define a solution: indeed, if we change (precisely, widen) the concentration range for the different elements present in the model, the number of solutions should increase (see supplementary material of, Clesi and Deguen, 2024a, especially for the low degree of discretization). However, the tolerance for the concentrations is not chosen randomly: in McDonough and Sun (1995), the major element error is 10%, Ni and Co are at 10% and V and Cr at 15%. With our threshold at 15 % for Ni, Co, V and Cr, we actually overestimate the number of solutions.

A full out sensitivity study being beyond the scope of the present study, but we tested a few scenarios with different limits, and compared the input parameters which yield a solution. In those tests, we defined the concentration range around the BSE concentrations (see main text for the values) within a predefined range for each element. These limits are explicitly described in Table S.1.

In Figure S.7 and S.8, are presented the number of solutions obtained in these sensitivity studies as a function of Δ (absolute number and relative success rate, respectively). For $k = 0.59$, we get solutions only if the ranges tested are higher than 20% for the trace elements. The numbers stays below 400 for 20 000 scenarios (success rate below $\sim$ 2%, Figure S.8). In Figure S.9, are presented the range of input parameters ($\overline{P_{eq}}$, a_P, f_c, λ) yielding solutions for different thresholds on major and trace elements, k of

Name	Major elements range (%)	Ni and Co range (%)	V and Cr range (%)	Comment
8-15	8	15	15	Major element range narrower than main text
8-20	8	20	20	Major element narrower and trace wider than main text
10-15	10	15	15	Same as main text
10-10-15	10	10	15	Ranges given in McDonough and Sun (1995)
10-20	10	20	20	Trace element range wider than main text

Table S.1. Name of the models tested for k = 0.59, 0.6, 0.75 and 1. The temperature was not calculated, as we focused on the number of solutions. These names are used in Figure S x to Sy.

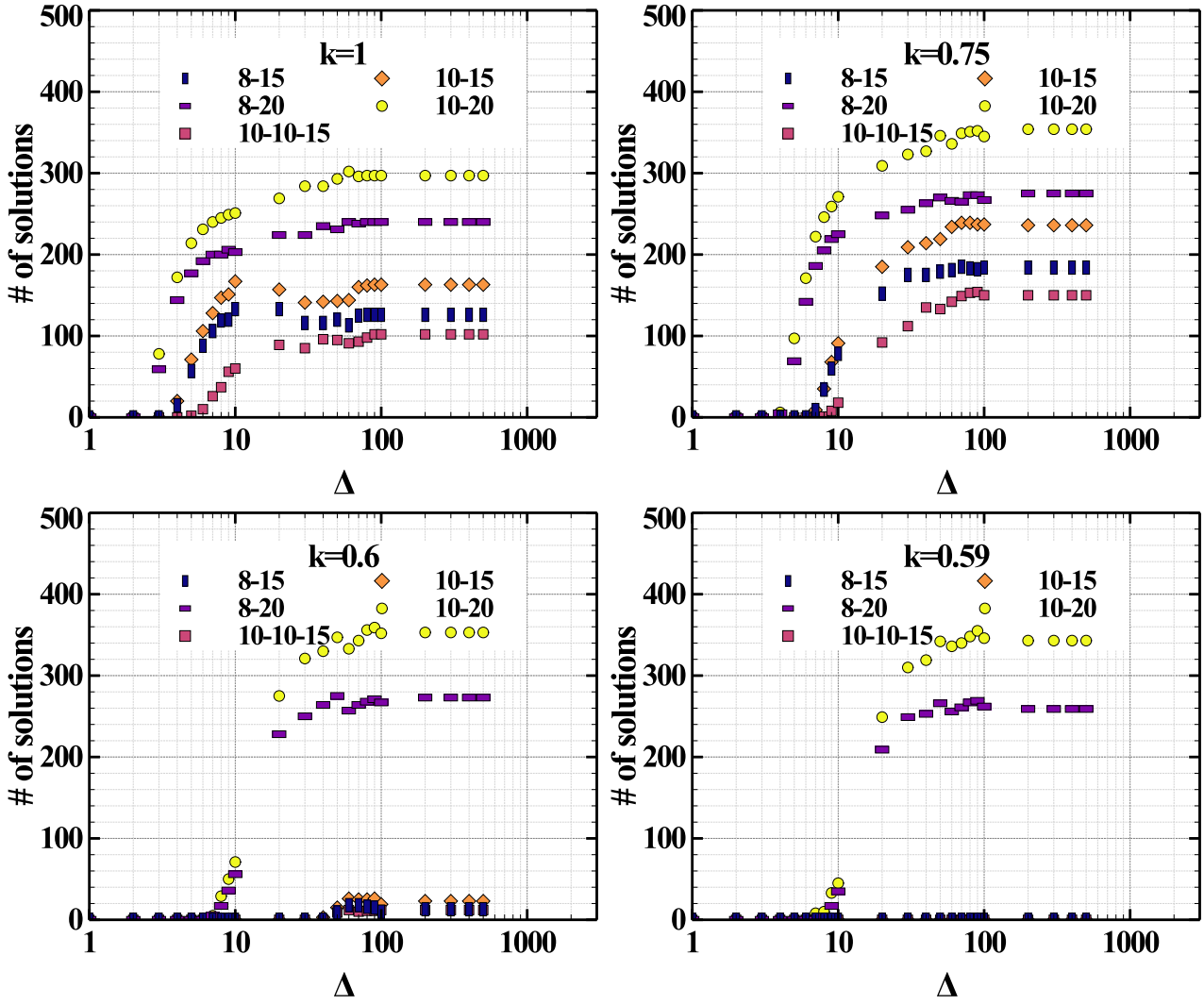

Figure S.7. Number of solutions yielded by the different models defined in Table S.1 as a function of Δ, for k = 1 (top left), 0.75 (top right), 0.6 (bottom left) and 0.59 (bottom right)

0.6, 0.75 and 1, and Δ = 100. This figure shows the input parameter ranges are a bit wider when the trace elements range for concentration are wider, but the values are comparable to what we observe in the main study (model 10-15). Therefore, the temperature range should be relatively comparable to the one presented in the main text of this article. In any case the range of concentrations in core and mantle are comparable, as evidenced by Figure S.10 focusing on NiO and CoO in the mantle. As expected, the

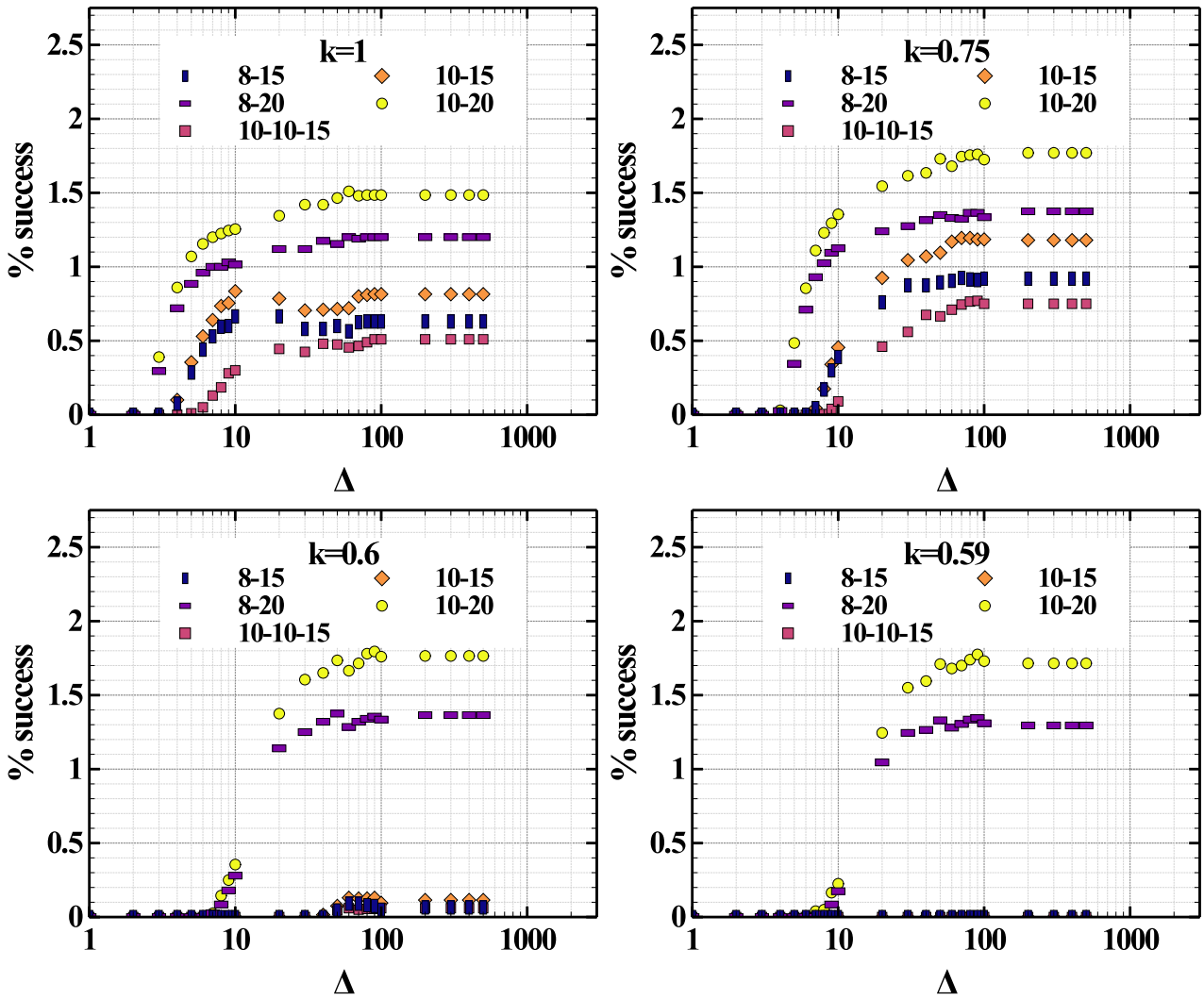

Figure S.8. Success rate (number of solution/20 000 scenarios), expressed in percentage, yielded by the different models defined in Table S.1 as a function of Δ, for k = 1 (top left), 0.75 (top right), 0.6 (bottom left) and 0.59 (bottom right)

mean values are the same, increasing the range of solution only add composition further from the BSE composition. Figures S.7 to S.10 show that widening the threshold for a solution will tend to lower the minimum values of k and Δ, but as argued in the following text, this comes with the cost of accepting models that are less representative of the Bulk Silicate Earth.

As the trace elements are the limiting factor for the number of solutions (see main text and supplementary materials of Clesi and Deguen, 2023, 2024a), we used the case of $k = 0.55$ and $k = 0.3$, with $\Delta = 100$ in both cases, to find what is the minimum range that will yield solution for at least one case where $k < 0.6$. For $\Delta = 100$, this range has to be 18% minimum for $k = 0.55$ and 23% for $k = 0.3$, which is a significant increases compare to what is accepted as the standard error on the BSE as given in McDonough and Sun (1995) (between 80% and 130 % increase for Ni and Co, between 20% and 55% for V and Cr). If anything, the standard error of the BSE is lower than the one given in McDonough and Sun (1995) (as hinted in McDonough, 2003). The BSE compositions obtained by wider range of concentrations tend to

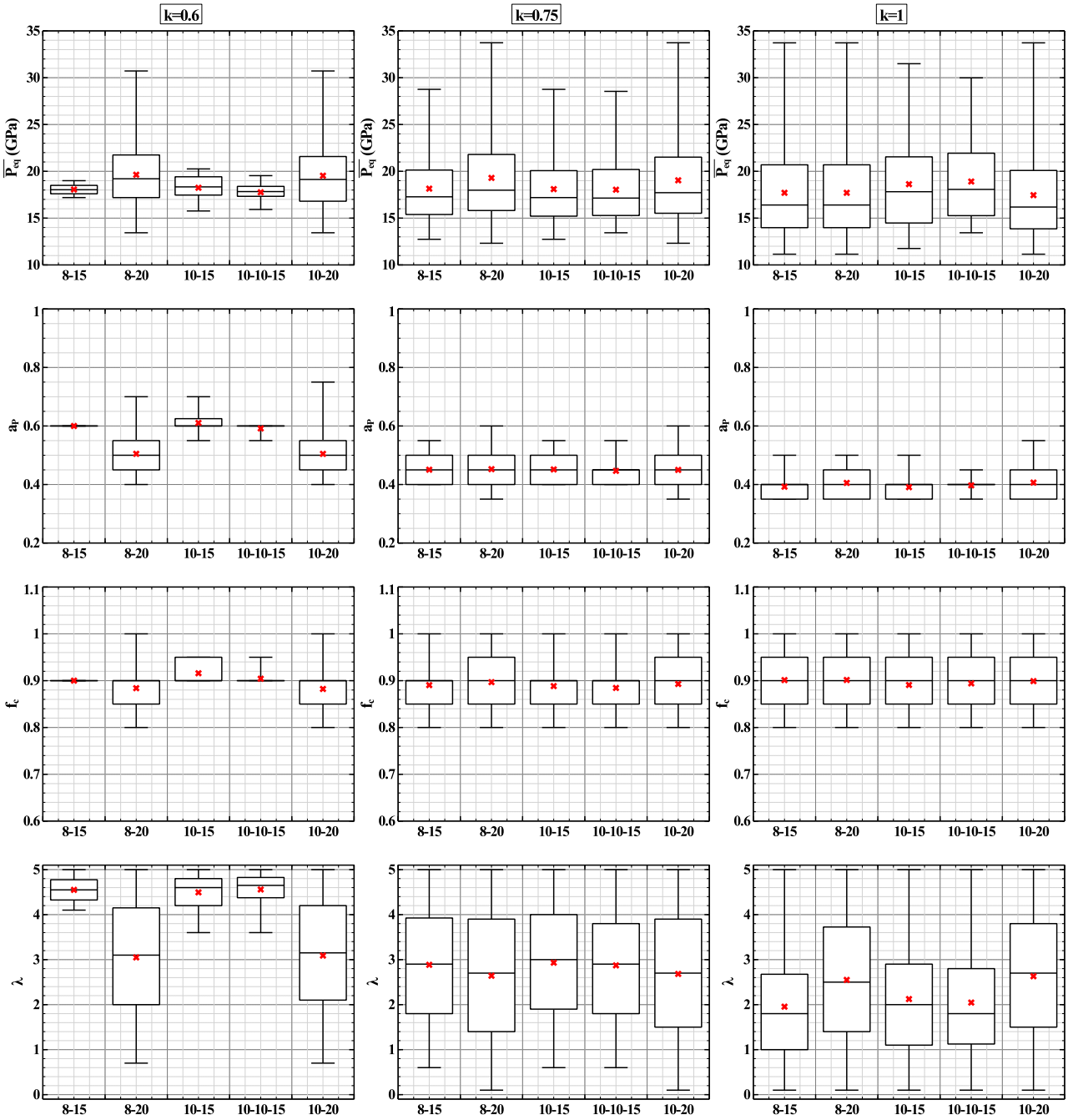

Figure S.9. Solutions ranges for $\Delta = 100$ and the different thresholds for solutions defined in Table S.1. First row: $\overline{P_{eq}}$ (GPa) for k=0.6 (left), 0.75 (middle) and 1 (right). Second row: a_P solutions range for the same values of k. Third row: f_c solution range. Bottom row: λ solution range.

scatter the output compositions away from what is expected in the BSE. In Figure S.11, an example of this phenomenon is plotted for $k = 0.6$, $\Delta = 100$, and the 4 trace elements (NiO, CoO, V_2O_3 and Cr_2O_3) for the models 8-15 and 8-20. For this value of k and Δ, the number of solution is low enough that it is possible to see the complexity induced by increasing the threshold in the definition of a solution. Indeed,

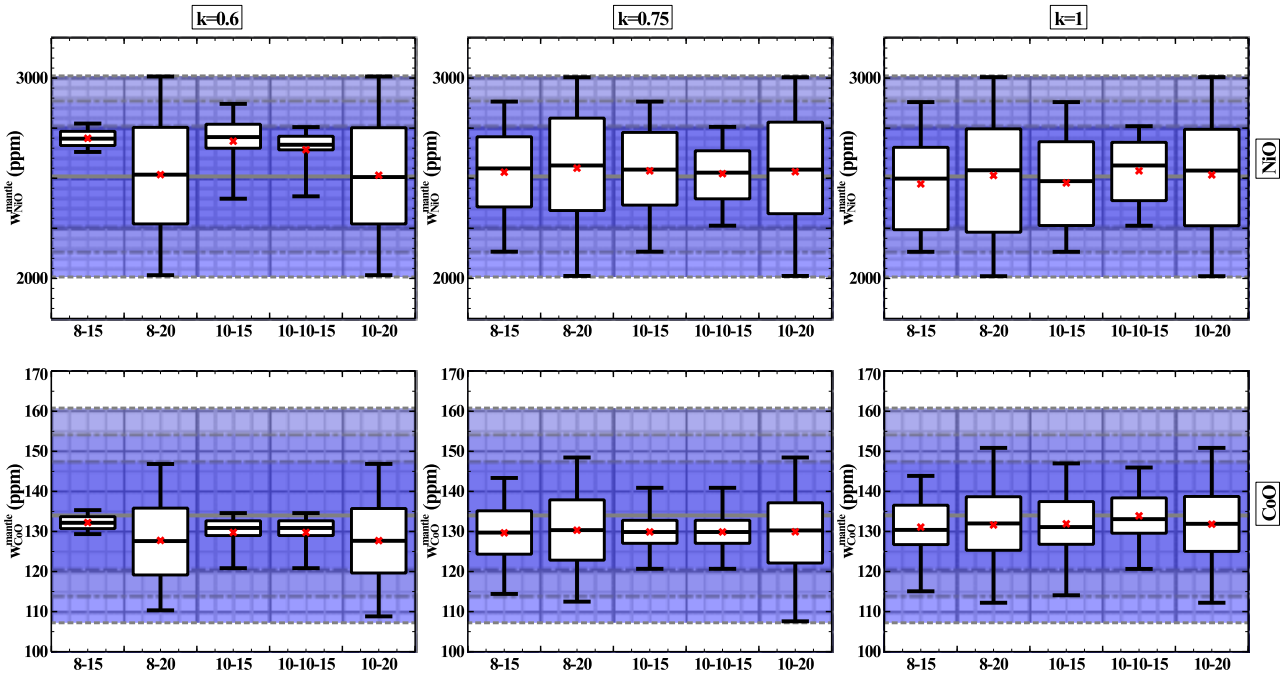

Figure S.10. Output concentrations range of NiO (top row) and CoO (bottom row) for the different models defined in Table S.1, $\Delta = 100$ and $k = 0.6$ (left column), 0.75 (middle column) and 1 (right column). The BSE concentration from McDonough and Sun (1995) is figured by the gray full line. The blue area and the dashed and dotted gray lines of different shading represent the different ranges (10, 15 and 20%) around the BSE value used in the study to define a solution.

for a threshold at 15% of the BSE value, the number of solutions is quite low, but all are close to the BSE, in particular Ni and Co. Increasing the thresholds tends to produce more solutions which are closer to the BSE for V and Cr, but these solutions tends to move the values of Ni and Co away from their expected BSE value. The same effect exists in reverse: scenarios with Ni and Co concentrations closer to the BSE value tends to yield V and Cr concentrations which are further away from their expected BSE values.

This result is dependent on the BSE model, so the value of $k = 0.6$ is valid only if we consider the BSE chondritic model as given in McDonough and Sun (1995) (which is the standard in most studies) to be realistic. Using other BSE models as reference (Allegre et al., 1995; Javoy et al., 2010; Korenaga, 2009) might lead to other results, but it is highly unlikely as their proposed composition all fall within a range of 10% of each other for the elements used in this study: Allegre et al. (1995) and McDonough and Sun (1995) are for instance very close. As for Javoy et al. (2010), they lower the amount of FeO in the mantle compared to the previously cited models (6.5%$\pm$ 1 % which overlaps with the 8% $\pm$ 0.8% we used in our study), but the concentrations of the other elements proposed in their study are very close and overlapping with the BSE model we used.

All of this tends to support the conclusions of the main text that at least 60 % of the metal needs to be equilibrated on average, all things kept equal, and in the optics of fitting a relatively chemically coherent Earth with the BSE standard composition. Changing the initial composition (number of elements, parametrization of partitioning, temperature of equilibrium) and/or BSE compositional model might change this number, but a proper study would have to be conducted separately.

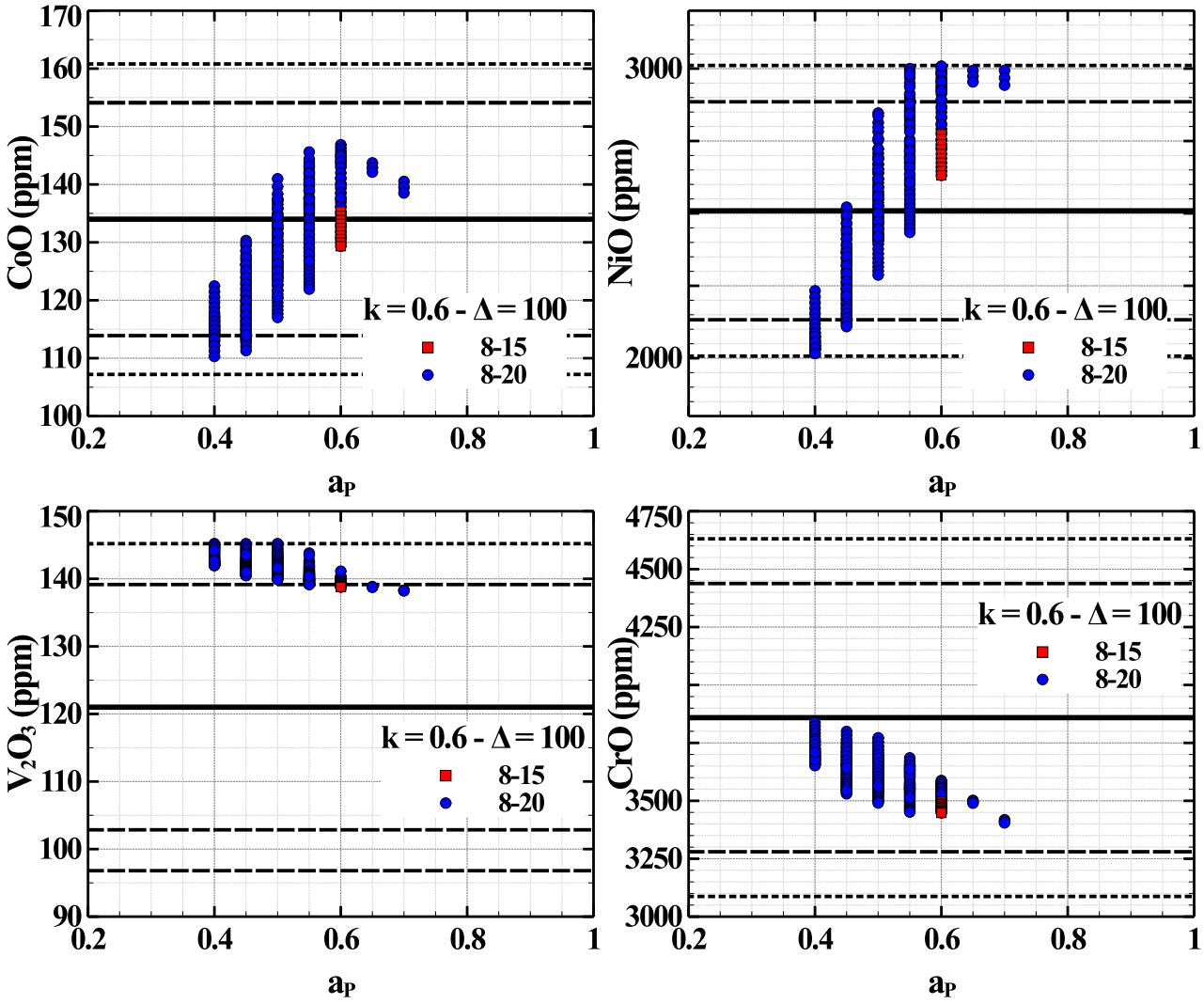

Figure S.11. Comparison of two models (8-15, red squares, and 8-20, blue circles) compositional outputs for trace elements (CoO, top left, NiO top right, V_2O_3 bottom left, and Cr_2O_3 bottom right) as a function of the corresponding values of a_P, for $\Delta = 100$ and $k = 0.6$. The black full line is the expected BSE concentration as defined in McDonough and Sun (1995), the dashed line are the 15 and 20% maximum variation threshold.

S.4 EFFECT OF SAMPLING DENSITY ON THE MODEL'S OUTPUTS

One parameter that could alter the results is the initial number of scenarios tested. In the main text we tested 20 values of a_P, 20 values of f_c and 50 values of λ with all values combined leading to 20 000 scenarios being tested, while several more could be added, which would change the overall ratio between number of solutions presented in Figure 4 of the main text and the outputs of the model. In this section, we performed some tests with a higher number of parameter: 40 values of a_P (between 0.025 and 1, by steps of 0.025), 40 values of f_c (between 0.025 and 1, by steps of 0.025) and 50 values of λ (same as in the main text, as this parameter already span a very large range). The number of scenarios tested is 4 times the one presented in the main text (80 000), which tends to increase the time of calculation by 2.6. We calculated the number of solutions for k = 0.6, 0.75 and 1, and Δ= 5, 10, 20, 50, 70 and 100; and did

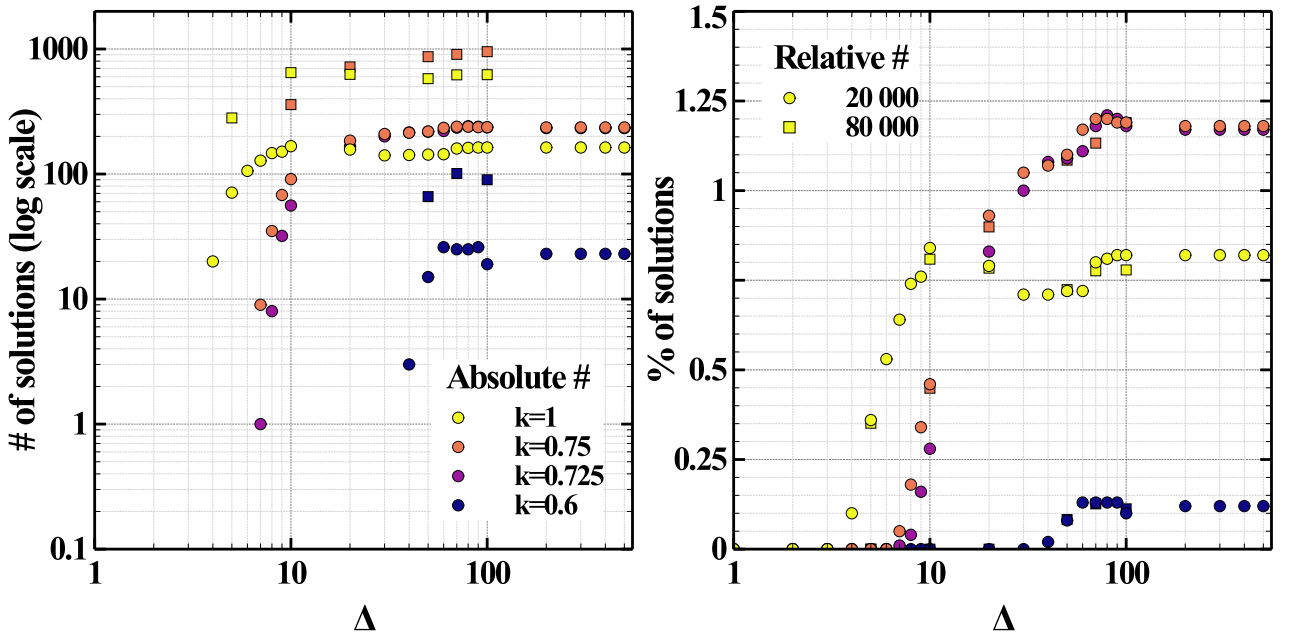

Figure S.12. Absolute number of solutions (left) and relative success rate (right) as a function of Δ for different values of k. The color scale in both panel represents the value of k (key in left panel). The square in both panel represent the bigger sampling range (80 000 scenarios tested) and the circles the sampling range used in the main text (20 000)

a specific calculation for the maximum number of solutions from Figure 4: $k = 0.725$ and $\Delta = 80$. The number of solutions normalized by the number of of the calculations for variable Δ and k are presented in Figure S.12, along with the same ratio from Figure 4 in the main text. The difference the two sampling methods have on the selections of input parameters is compared in Figure S.13.

If we focus only on the maximum highlighted in Figure 4, we found 913 solutions with the new sampling of a_P and f_c. The solution rate is therefore $913/80000 \sim 1.14\%$, compared to the $241/20000 \sim 1.21$ in the initial figure, which is to say roughly the same.

As shown in Figures S.12 the absolute number of solution increases when increasing the number of scenarios, but the ratio are comparable (barely visible squares in the right panel of the Figure S.12). The mean values and ranges of the input parameters (a_P, f_c,λ and $\overline{P_{eq}}$, Figure S.13) are comparable to the one in the main text, thus yielding similar compositions and temperatures in similar conditions.

All said and done, the model is not very sensitive to the number of scenarios tested, as long as the range a_P and f_c tested correctly spans the total values possible: a_P must be positive (a magma ocean must exist) and below 1 (the magma ocean maximum extent must not be higher than the CMB); f_c must be comprised between 0 and 1 as matter cannot accrete before the planet starts to grow, or after the planet has grown.

S.5 ERROR ESTIMATION ON THE TEMPERATURE MODEL

The model is dependent of several parameters, measured or calculated more or less precisely. The error induced by the number of steps used in the numerical integration is considered to be negligible, increasing the number of steps changes the temperature only for the second decimal, i.e. the order of magnitude of the relative error is $10^{-3}\%$ (~ 0.00003 K in absolute value variation). However, there are three main

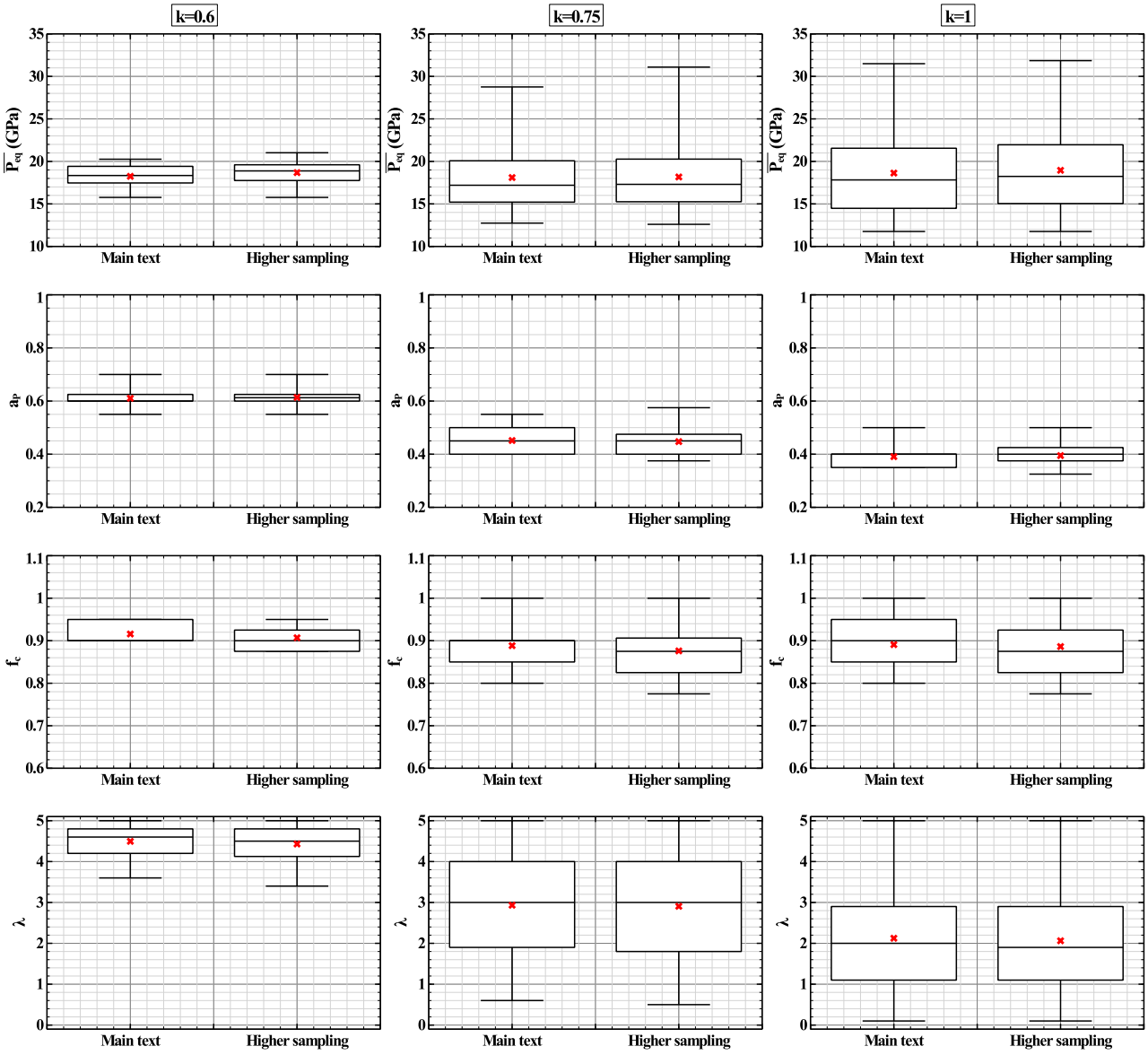

Figure S.13. Comparison of the results for a larger sampling distribution with the main text results for $\Delta = 100$. First row: $\overline{P_{eq}}$ (GPa) for k=0.6 (left), 0.75 (middle) and 1 (right). Second row: a_P solutions range for the same values of k. Third row: f_c solution range. Bottom row: λ solution range.

sources of relative error for the final temperature. The first one is the error on the liquidus temperature as given by equation (1) of the main text. The second source of error is the error on K_s in Equation (2) of the main text and the third one is the error on γ in that same equation. The initial liquidus temperature carries a maximal error of 150 K for the maximum temperature of 4750 K (Andrault et al., 2011). This translates to a relative error $\varepsilon_{T_{eq}}$ of 3.17 % that will be carried to the end. The main variation of temperature is due to compression, which depends on the K_s and γ. For the K_s as defined by this study, the values of K_0 and K' where obtained by fitting a Murnaghan equation of state to a PREM based model (Clesi and Deguen, 2023). Therefore, the error on this parameters is the same error as the overall error on the PREM model (Dziewonski and Anderson, 1981), which is given between 2 and 4%. To be conservative, we use a relative

error for K_s of 4% (hereafter $\varepsilon_{K_s} = 0.04$), which yields the absolute errors on K_0 and K' as given in the main text. For γ, we used the results of a previously published sensitivity study (Clesi and Deguen, 2024b) for the Al'Tshuler et al. (1987) formalism. Using the χ^2 given in Clesi and Deguen (2024b), we calculated the relative error induced by the Grüneisen parameter to be 6%, in the following calculations $\varepsilon_\gamma = 0.06$. Then combining these three relative errors ($\varepsilon_{T_{eq}}$, ε_{K_s} and ε_γ), the final relative error on temperature ε_{total} is therefore:

$$\varepsilon_{total} = \sqrt{(\varepsilon_{T_{eq}})^2 + (\varepsilon_{K_s})^2 + (\varepsilon_\gamma)^2} = 7.22\% \tag{S.2}$$

This 7.22 % relative error is applied uniformly throughout the main text. The error for $T^{is}_{CMB} = 4200K$ is $\pm 300K$ (maximum value and maximum error) and the error for $T^{is}_{CMB} = 3800K$ is $\pm 274K$ (minimum value and minimum error). Finally, the error on the trend given for Figure 9 arises from the fit of temperature. From Table 2 in the main text and the same propagation of relative error in Equation S.2 applied to the formula of Equation (23) in the main text we get:

- $\varepsilon_{\Delta T} = 1.3 \times 10^{18}\%$ for the model of variation with T^{is}_{CMB} min values. This high error is due to the lack of Δ dependency yielding a poor fit.
- $\varepsilon_{\Delta T} = 3.85\%$ for the model of variation of the $\overline{T^{is}_{CMB}}$ values. The absolute errors on the effect of disequilibrium is therefore comprised between 2 and 4 K.
- $\varepsilon_{\Delta T} = 15\%$ for the model of variation of T^{is}_{CMB} max values. The absolute error on the maximum variation is therefore 38 K for $\Delta T(k, \Delta) = 250K$

REFERENCES

Allegre, C. J., Poirier, J.-P., Humler, E., and Hofmann, A. W. (1995). The chemical composition of the earth. *Earth and Planetary Science Letters*, 134(3-4):515–526.

Al'Tshuler, L., Brusnikin, S., and Kuz'Menkov, E. (1987). Isotherms and Grüneisen functions for 25 metals. *Journal of Applied Mechanics and Technical Physics*, 28(1):129–141.

Andrault, D., Bolfan-Casanova, N., Nigro, G. L., Bouhifd, M. A., Garbarino, G., and Mezouar, M. (2011). Solidus and liquidus profiles of chondritic mantle: Implication for melting of the Earth across its history. *Earth and planetary science letters*, 304(1-2):251–259.

Boujibar, A., Andrault, D., Bouhifd, M., Bolfan-Casanova, N., Devidal, J.-L., and Trcera, N. (2014). Metal–silicate partitioning of sulphur, new experimental and thermodynamic constraints on planetary accretion. *Earth and Planetary Science Letters*, 391:42–54.

Canup, R. M. (2004). Simulations of a late lunar-forming impact. *Icarus*, 168(2):433–456.

Canup, R. M., Righter, K., Dauphas, N., Pahlevan, K., Ćuk, M., Lock, S. J., Stewart, S. T., Salmon, J., Rufu, R., Nakajima, M., et al. (2023). Origin of the moon. *Reviews in Mineralogy and Geochemistry*, 89(1):53–102.

Clesi, V. and Deguen, R. (2023). Linking the core heat content to earth's accretion history. *Geochemistry, Geophysics, Geosystems*, 24(5):e2022GC010661.

Clesi, V. and Deguen, R. (2024a). Effect of discretization choices when modeling the thermo-chemical history of the accreting core. *Chemical Geology*, 657:122104.

Clesi, V. and Deguen, R. (2024b). Grüneisen parameter formalism in the study of the earth's core formation: a sensitivity study. *Geophysical Journal International*, 237(3):1275–1284.

Deguen, R., Landeau, M., and Olson, P. (2014). Turbulent metal–silicate mixing, fragmentation, and equilibration in magma oceans. *Earth and Planetary Science Letters*, 391:274–287.

Dziewonski, A. M. and Anderson, D. L. (1981). Preliminary reference Earth model. *Physics of the earth and planetary interiors*, 25(4):297–356.

Fiquet, G., Auzende, A., Siebert, J., Corgne, A., Bureau, H., Ozawa, H., and Garbarino, G. (2010). Melting of peridotite to 140 gigapascals. *Science*, 329(5998):1516–1518.

Fischer, R. A., Nakajima, Y., Campbell, A. J., Frost, D. J., Harries, D., Langenhorst, F., Miyajima, N., Pollok, K., and Rubie, D. C. (2015). High pressure metal–silicate partitioning of Ni, Co, V, Cr, Si, and O. *Geochimica et Cosmochimica Acta*, 167:177–194.

Gu, J. T., Fischer, R. A., Brennan, M. C., Clement, M. S., Jacobson, S. A., Kaib, N. A., O'Brien, D. P., and Raymond, S. N. (2023). Comparisons of the core and mantle compositions of earth analogs from different terrestrial planet formation scenarios. *Icarus*, 394:115425.

Henningsen, E. L., Korenaga, J., and Marchi, S. (2025). Impact-driven redox stratification of earth's mantle. *Journal of Geophysical Research: Solid Earth*, 130(4):e2024JB030817.

Jacobson, S. A., Rubie, D. C., Hernlund, J., Morbidelli, A., and Nakajima, M. (2017). Formation, stratification, and mixing of the cores of Earth and Venus. *Earth and Planetary Science Letters*, 474:375–386.

Javoy, M., Kaminski, E., Guyot, F., Andrault, D., Sanloup, C., Moreira, M., Labrosse, S., Jambon, A., Agrinier, P., Davaille, A., et al. (2010). The chemical composition of the earth: Enstatite chondrite models. *Earth and planetary science letters*, 293(3-4):259–268.

Korenaga, J. (2009). A method to estimate the composition of the bulk silicate earth in the presence of a hidden geochemical reservoir. *Geochimica et Cosmochimica Acta*, 73(22):6952–6964.

Landeau, M., Aubert, J., and Olson, P. (2017). The signature of inner-core nucleation on the geodynamo. *Earth and Planetary Science Letters*, 465:193–204.

Landeau, M., Deguen, R., Phillips, D., Neufeld, J. A., Lherm, V., and Dalziel, S. B. (2021). Metal-silicate mixing by large Earth-forming impacts. *Earth and Planetary Science Letters*, 564:116888.

Landeau, M., Olson, P., Deguen, R., and Hirsh, B. H. (2016). Core merging and stratification following giant impact. *Nature Geoscience*, 9(10):786–789.

McDonough, W. (2003). Compositional model for the earth core. *Treatise on geochemistry*, pages 547–568.

McDonough, W. and Sun, S.-S. (1995). The composition of the Earth. *Chemical geology*, 120(3-4):223–253.

Nakajima, M., Golabek, G. J., Wünnemann, K., Rubie, D. C., Burger, C., Melosh, H. J., Jacobson, S. A., Manske, L., and Hull, S. D. (2021). Scaling laws for the geometry of an impact-induced magma ocean. *Earth and Planetary Science Letters*, 568:116983.

Nimmo, F., O'brien, D., and Kleine, T. (2010). Tungsten isotopic evolution during late-stage accretion: constraints on earth–moon equilibration. *Earth and Planetary Science Letters*, 292(3-4):363–370.

Rubie, D., Jacobson, S., Morbidelli, A., O'Brien, D., Young, E., de Vries, J., Nimmo, F., Palme, H., and Frost, D. (2015). Accretion and differentiation of the terrestrial planets with implications for the compositions of early-formed Solar System bodies and accretion of water. *Icarus*, 248:89–108.

Rudge, J. F., Kleine, T., and Bourdon, B. (2010). Broad bounds on earth's accretion and core formation constrained by geochemical models. *Nature Geoscience*, 3(6):439–443.

Zhou, Y., Liu, Y., Reinhardt, C., and Deng, H. (2022). The core-merging giant impact in earth's accretion history and its implications. *Acta Geochimica*, 41(4):553–567.

ADDITIONAL FIGURES CITED IN THE MAIN TEXT

In this section are presented the Figures cited in the main text which are not related to the additional sections in the present document.

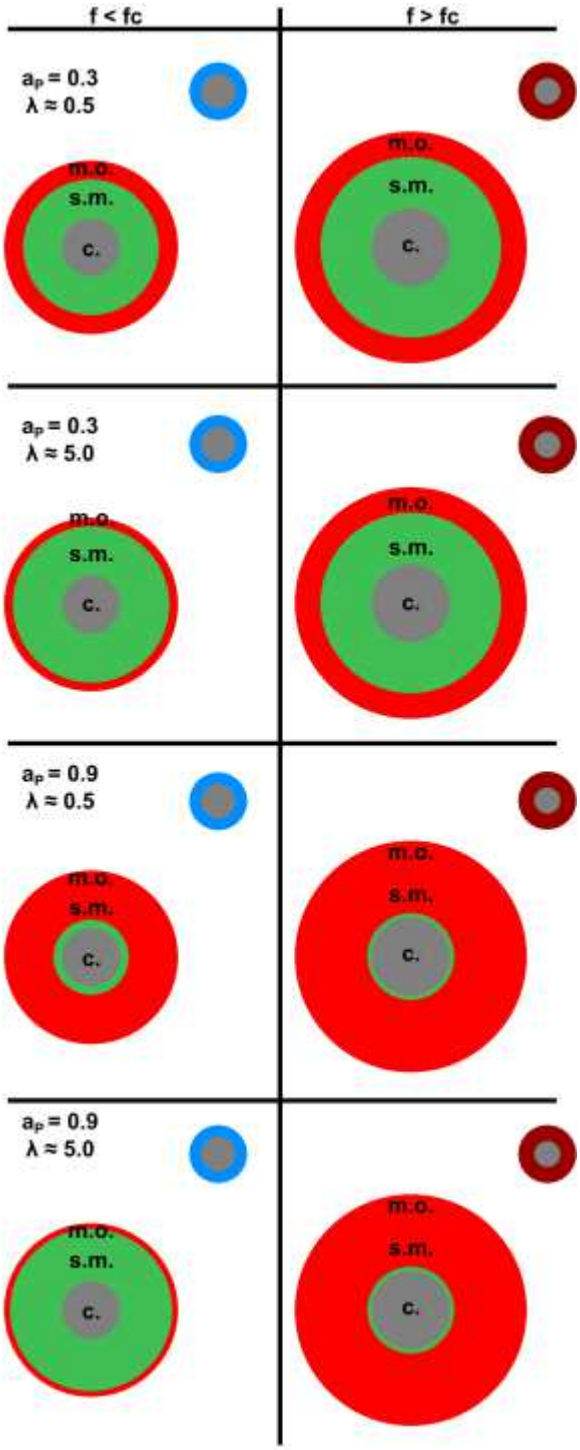

Figure S.14. Schematics of the physical meaning of the parameters a_P, f_c and λ used to parameterize the models of accretion. This Figure has been published in Clesi and Deguen (2024a) and is reproduced here with the authorization of authors. The left column shows the early part of accretion ($f < f_c$, more reduced impactor in blue). The right column how the later stage of accretion ($f > f_c$, more oxidized impactor in dark red). The two first lines show the effect of λ for a low values of a_P on the depth of the magma ocean throughout accretion. The two bottom lines show the effect of λ for high values of a_P on the evolution of the depth of the magma ocean during accretion. m.o. = magma ocean (red), s.m. = solid mantle (green) and c. = core (grey).

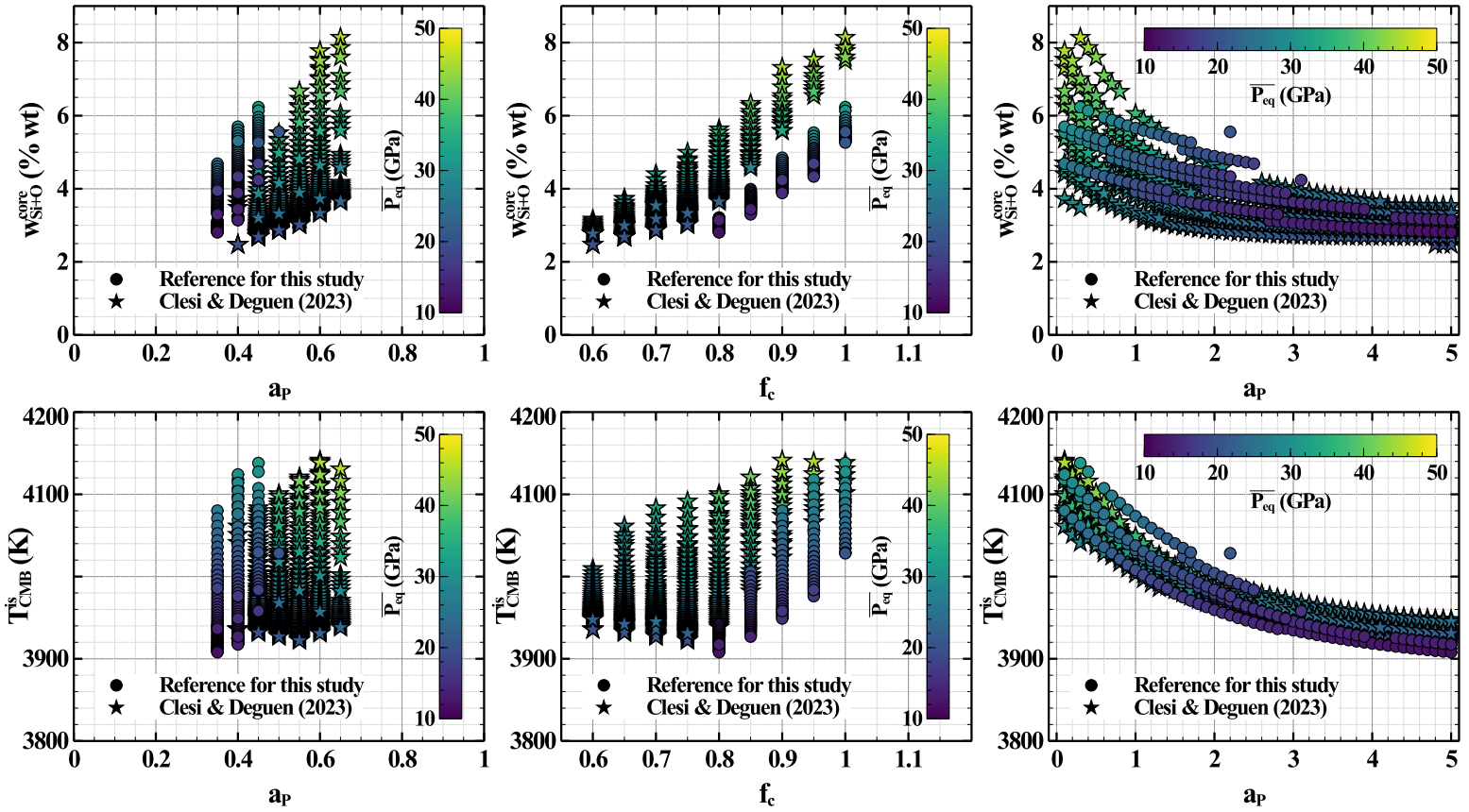

Figure S.15. Comparison of the reference solutions that are used in this study (round symbols) with the solutions obtained in Clesi and Deguen (2023) with another filter (stars). The format of this figure is the derived from Figure 8 of Clesi and Deguen (2023) to better highlight the differences between the solutions. The overall correlations are the same, with the weighted mean filter selecting for higher pressures models. The first row shows the correlation between light elements in the core with the three input parameters on each column: w^{core}_{Si+O} vs a_P on the left panel, w^{core}_{Si+O} vs f_c on the middle panel, w^{core}_{Si+O} vs λ on the right panel. The second row shows the correlation between the isentropic temperature at the CMB (T^{is}_{CMB} with the three input parameters presented in the same order. The color scale in all panel is the composite input parameter $\overline{P_{eq}}$ in GPa.

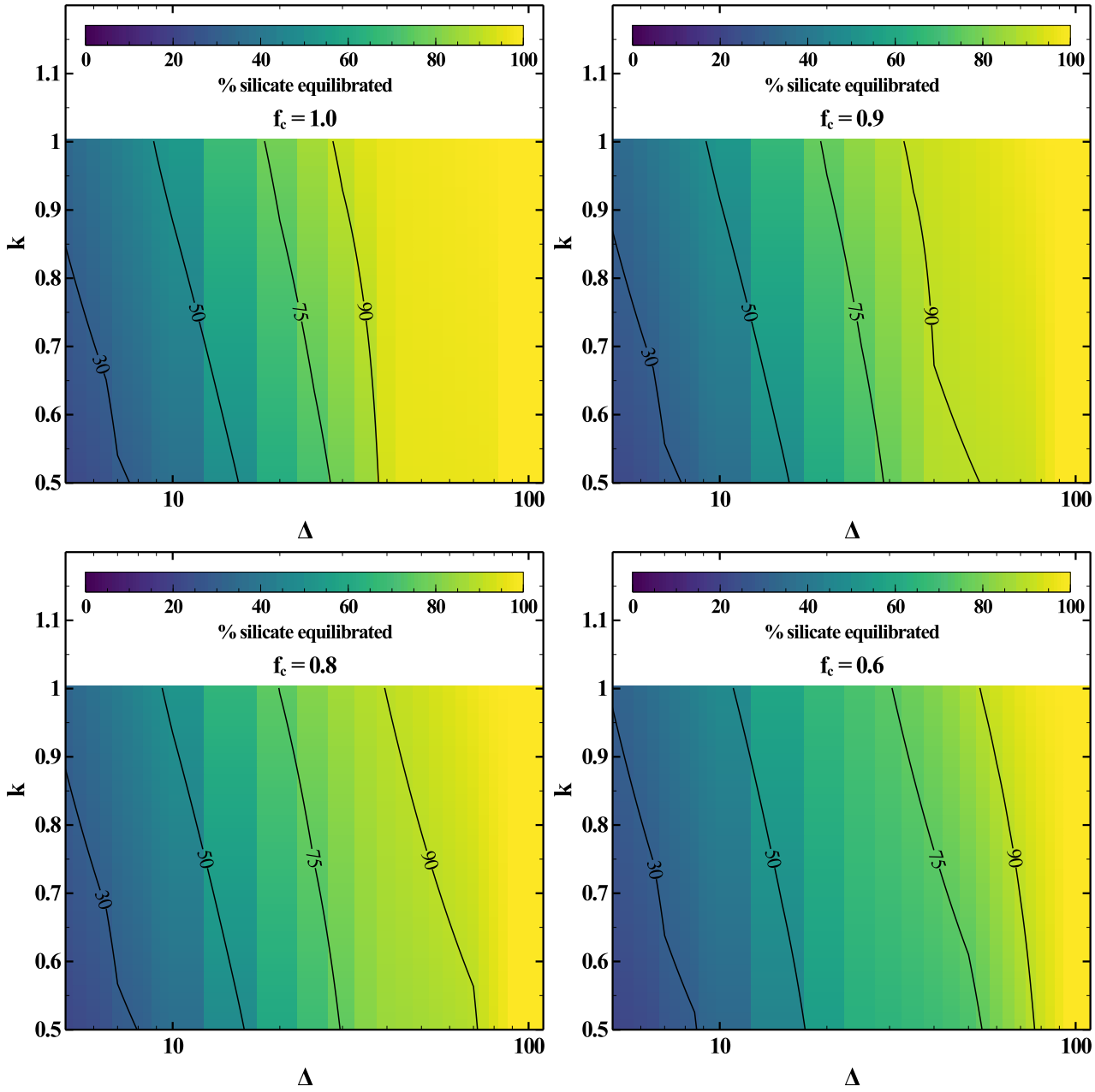

Figure S.16. Percentage of equilibrated mantle (color map) as a function of k (y-axis) and Δ (x-axis) for $f_c = 1$ (top left), $f_c = 0.9$ (top right), $f_c = 0.8$ (bottom left), $f_c = 0.8$ (bottom right). Full equilibrium is reached for $\Delta > 100$ in all relevant cases.

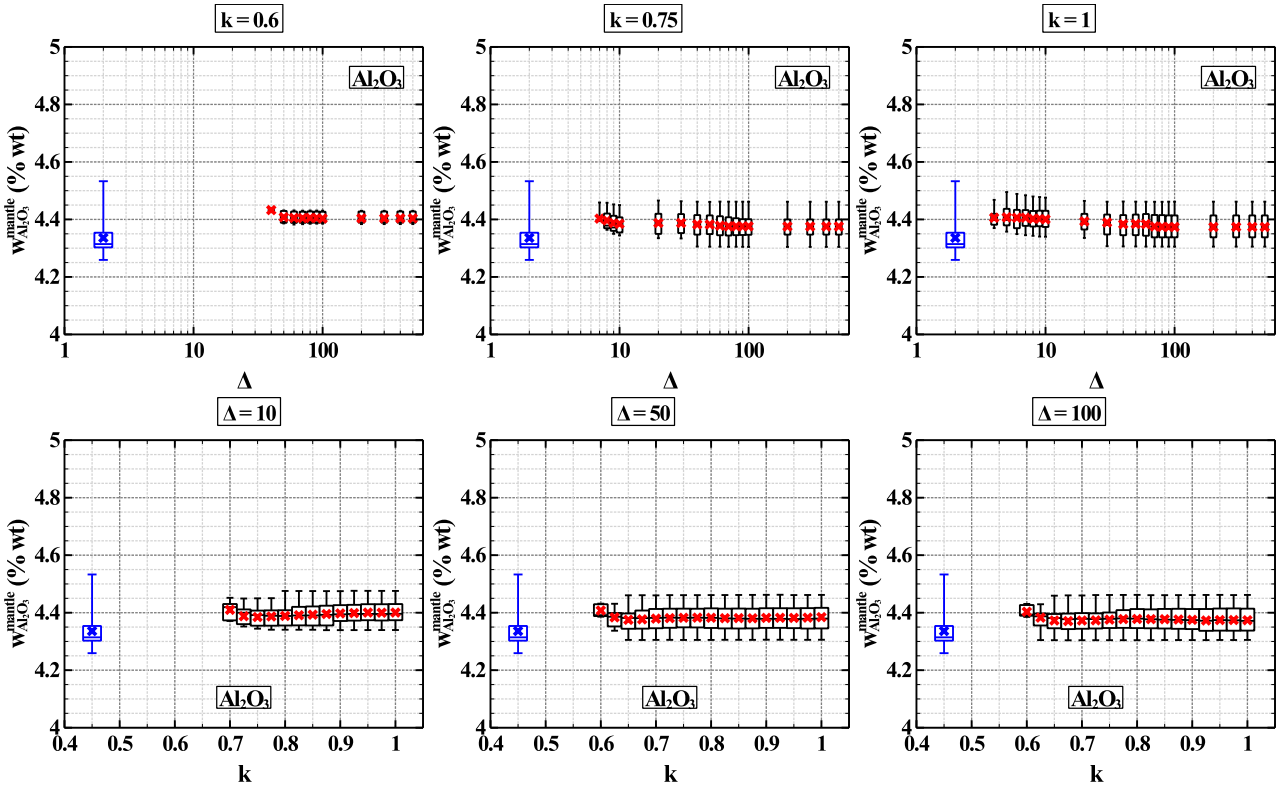

Figure S.17. Evolution of Al_2O_3 concentrations (% wt) in the mantle as a function of Δ for fixed values of k (top row), and as a function of k for fixed values of Δ (bottom row). In each panel the entire solutions range are presented as boxplots, with the red cross being the mean value of the parameter, the white box delimiting the 1st and 3rd quartile, the horizontal line the median value and the vertical lines the minimum and maximum values. The reference model dataset is presented in blue with the same type of plot for comparison.

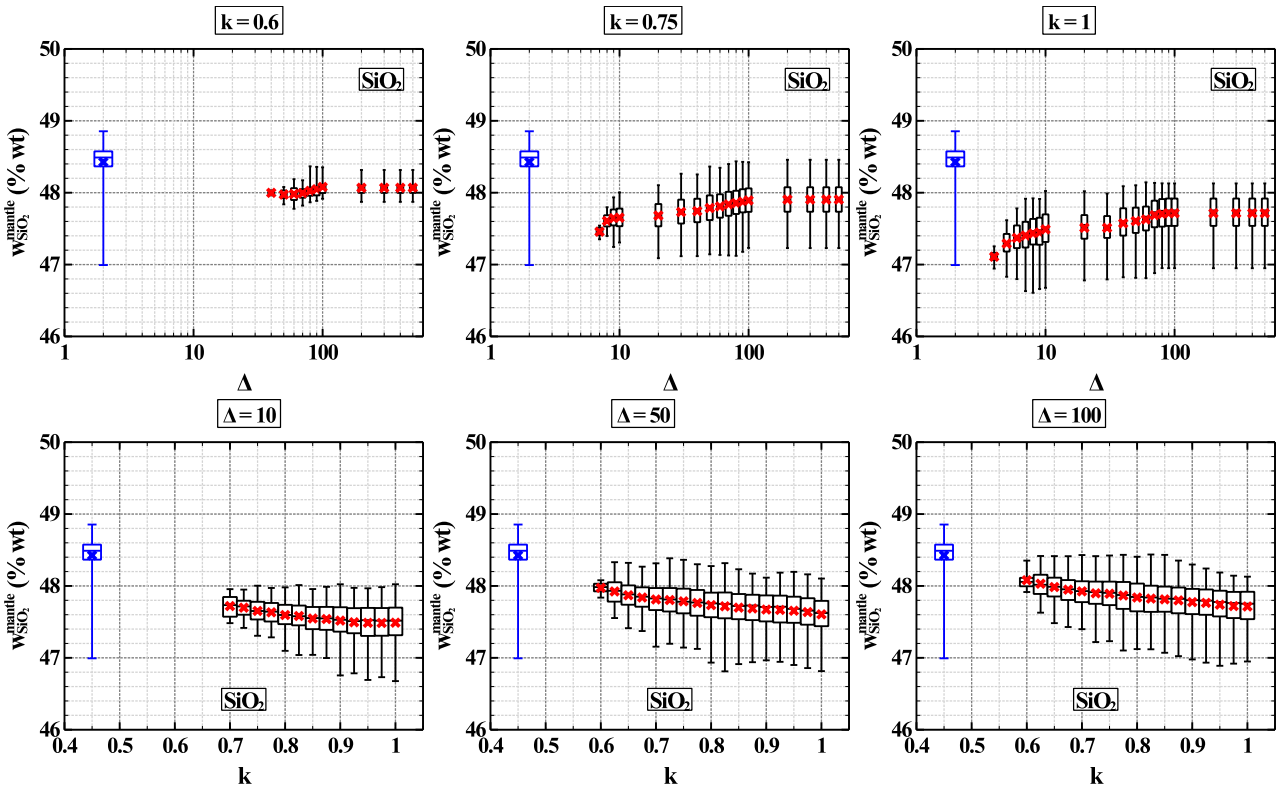

Figure S.18. Evolution of SiO_2 concentrations (% wt) in the mantle as a function of Δ for fixed values of k (top row), and as a function of k for fixed values of Δ (bottom row). In each panel the entire solutions range are presented as boxplots, with the red cross being the mean value of the parameter, the white box delimiting the 1st and 3rd quartile, the horizontal line the median value and the vertical lines the minimum and maximum values. The reference model dataset is presented in blue with the same type of plot for comparison.

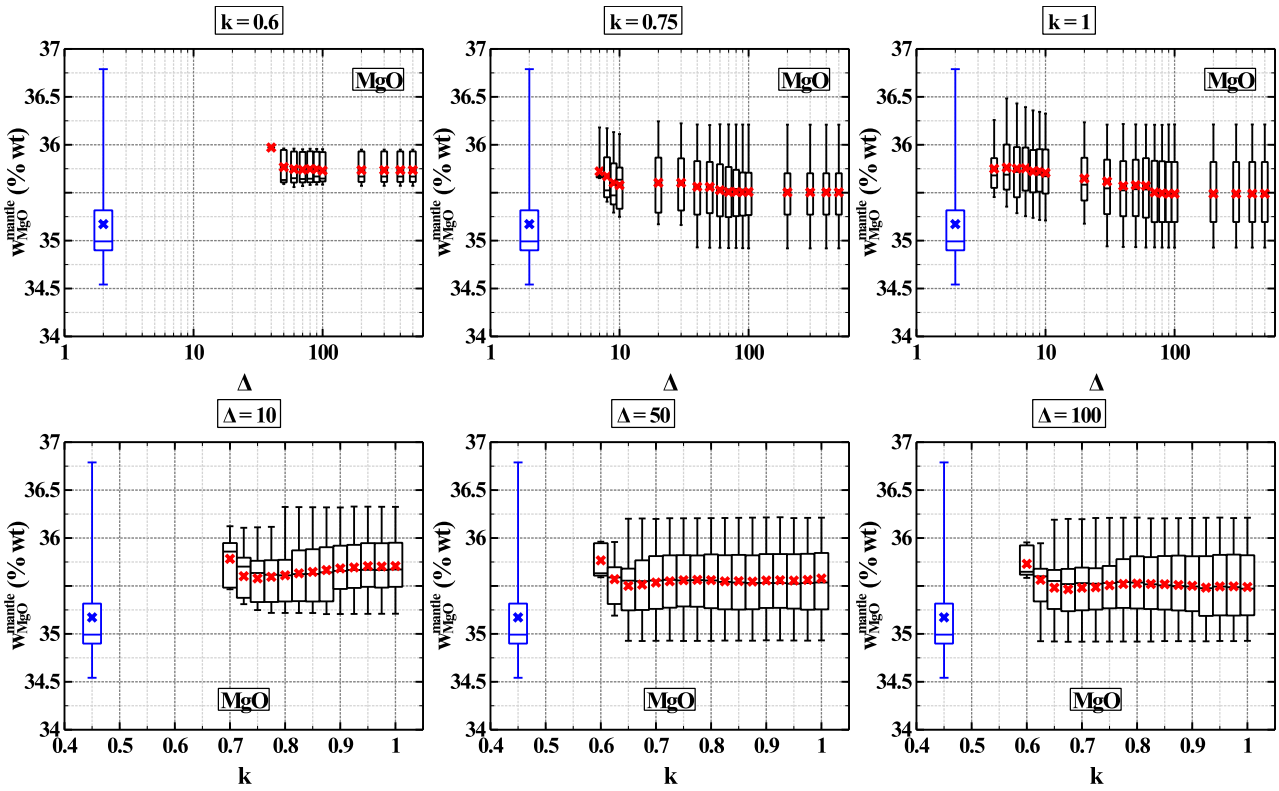

Figure S.19. Evolution of MgO concentrations (% wt) in the mantle as a function of Δ for fixed values of k (top row), and as a function of k for fixed values of Δ (bottom row). In each panel the entire solutions range are presented as boxplots, with the red cross being the mean value of the parameter, the white box delimiting the 1st and 3rd quartile, the horizontal line the median value and the vertical lines the minimum and maximum values. The reference model dataset is presented in blue with the same type of plot for comparison.

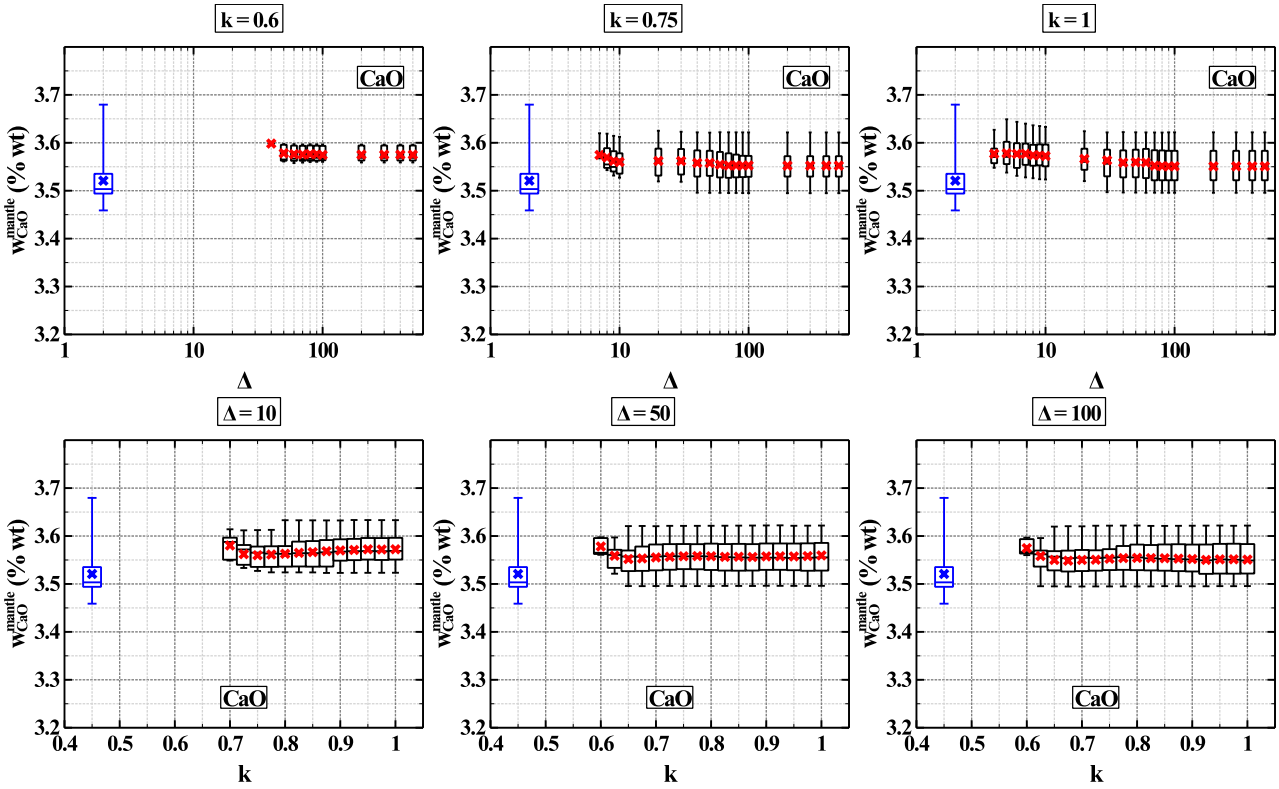

Figure S.20. Evolution of CaO concentrations (% wt) in the mantle as a function of Δ for fixed values of k (top row), and as a function of k for fixed values of Δ (bottom row). In each panel the entire solutions range are presented as boxplots, with the red cross being the mean value of the parameter, the white box delimiting the 1st and 3rd quartile, the horizontal line the median value and the vertical lines the minimum and maximum values. The reference model dataset is presented in blue with the same type of plot for comparison.

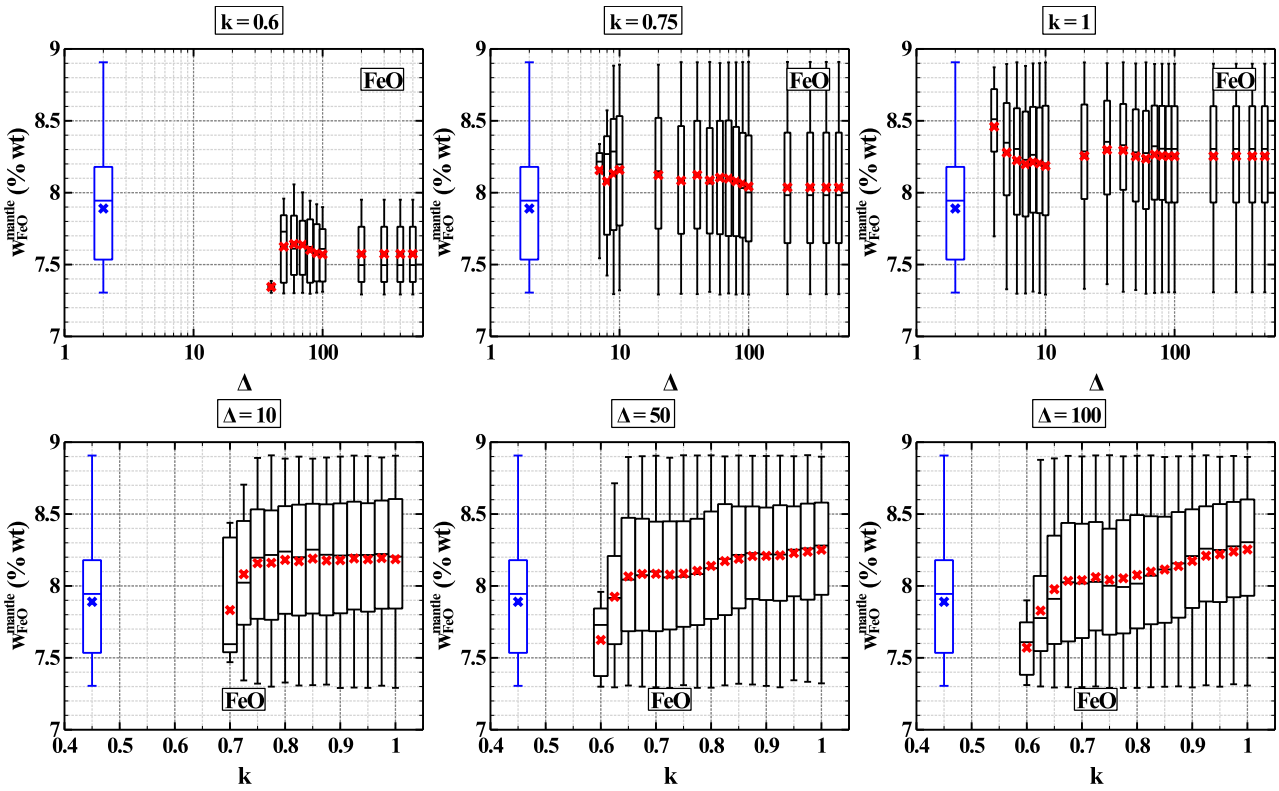

Figure S.21. Evolution of FeO concentrations (%wt) in the mantle as a function of Δ for fixed values of k (top row), and as a function of k for fixed values of Δ (bottom row). In each panel the entire solutions range are presented as boxplots, with the red cross being the mean value of the parameter, the white box delimiting the 1st and 3rd quartile, the horizontal line the median value and the vertical lines the minimum and maximum values. The reference model dataset is presented in blue with the same type of plot for comparison.

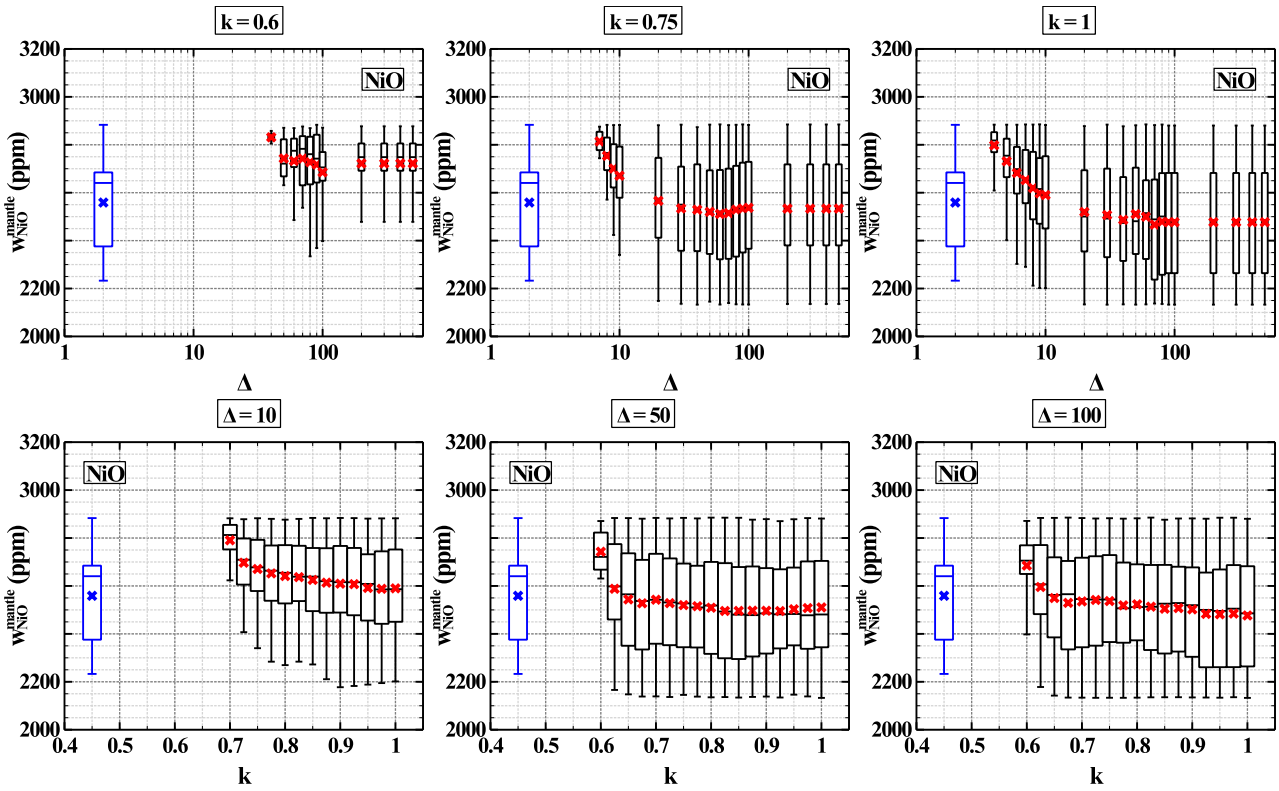

Figure S.22. Evolution of NiO concentrations (ppm) in the mantle as a function of Δ for fixed values of k (top row), and as a function of k for fixed values of Δ (bottom row). In each panel the entire solutions range are presented as boxplots, with the red cross being the mean value of the parameter, the white box delimiting the 1st and 3rd quartile, the horizontal line the median value and the vertical lines the minimum and maximum values. The reference model dataset is presented in blue with the same type of plot for comparison.

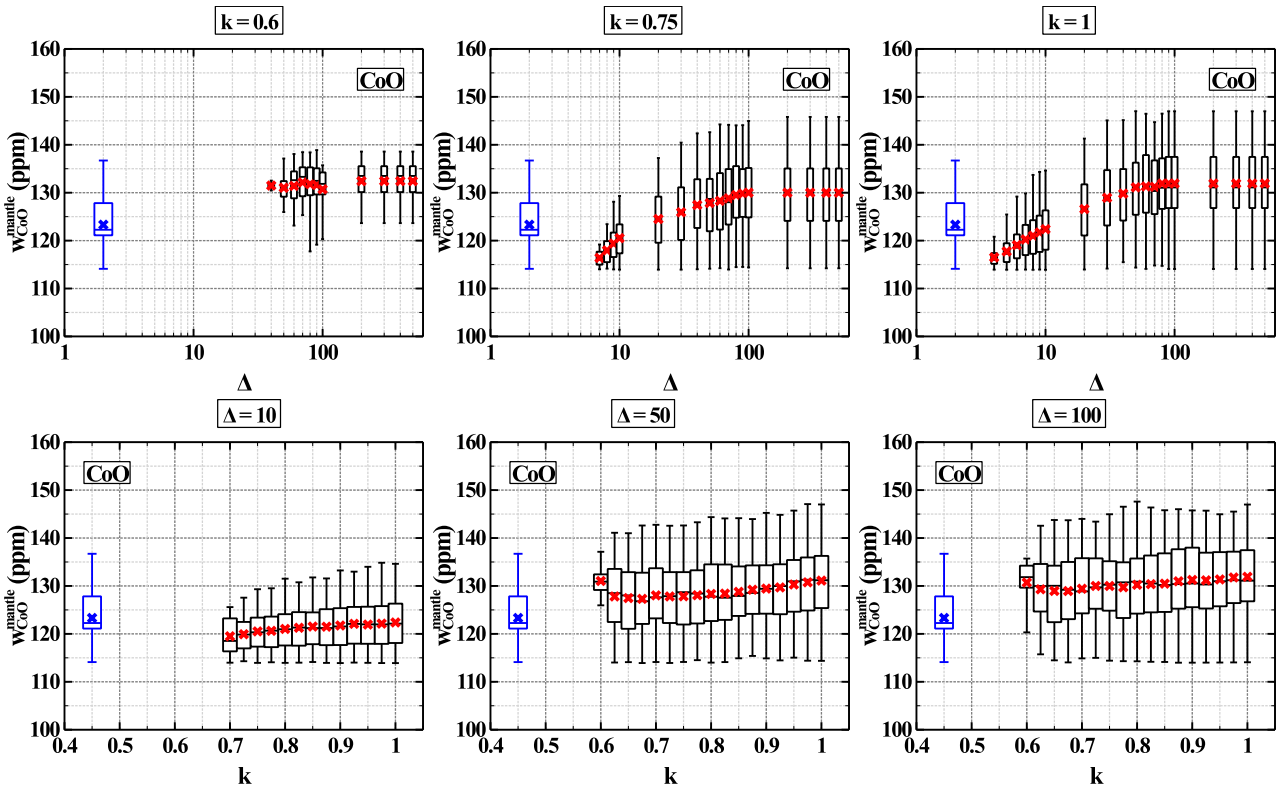

Figure S.23. Evolution of CoO concentrations (ppm) in the mantle as a function of Δ for fixed values of k (top row), and as a function of k for fixed values of Δ (bottom row). In each panel the entire solutions range are presented as boxplots, with the red cross being the mean value of the parameter, the white box delimiting the 1st and 3rd quartile, the horizontal line the median value and the vertical lines the minimum and maximum values. The reference model dataset is presented in blue with the same type of plot for comparison.

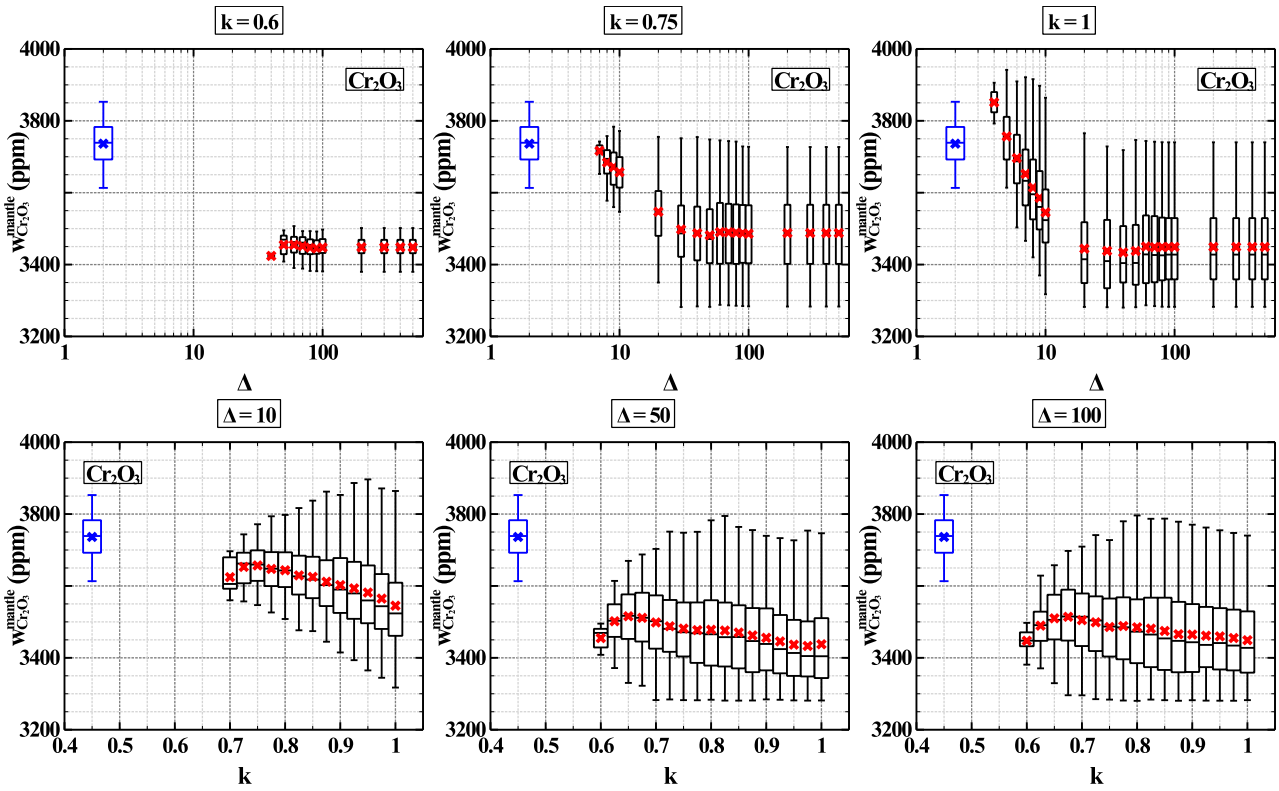

Figure S.24. Evolution of Cr_2O_3 concentrations (ppm) in the mantle as a function of Δ for fixed values of k (top row), and as a function of k for fixed values of Δ (bottom row). In each panel the entire solutions range are presented as boxplots, with the red cross being the mean value of the parameter, the white box delimiting the 1st and 3rd quartile, the horizontal line the median value and the vertical lines the minimum and maximum values. The reference model dataset is presented in blue with the same type of plot for comparison.

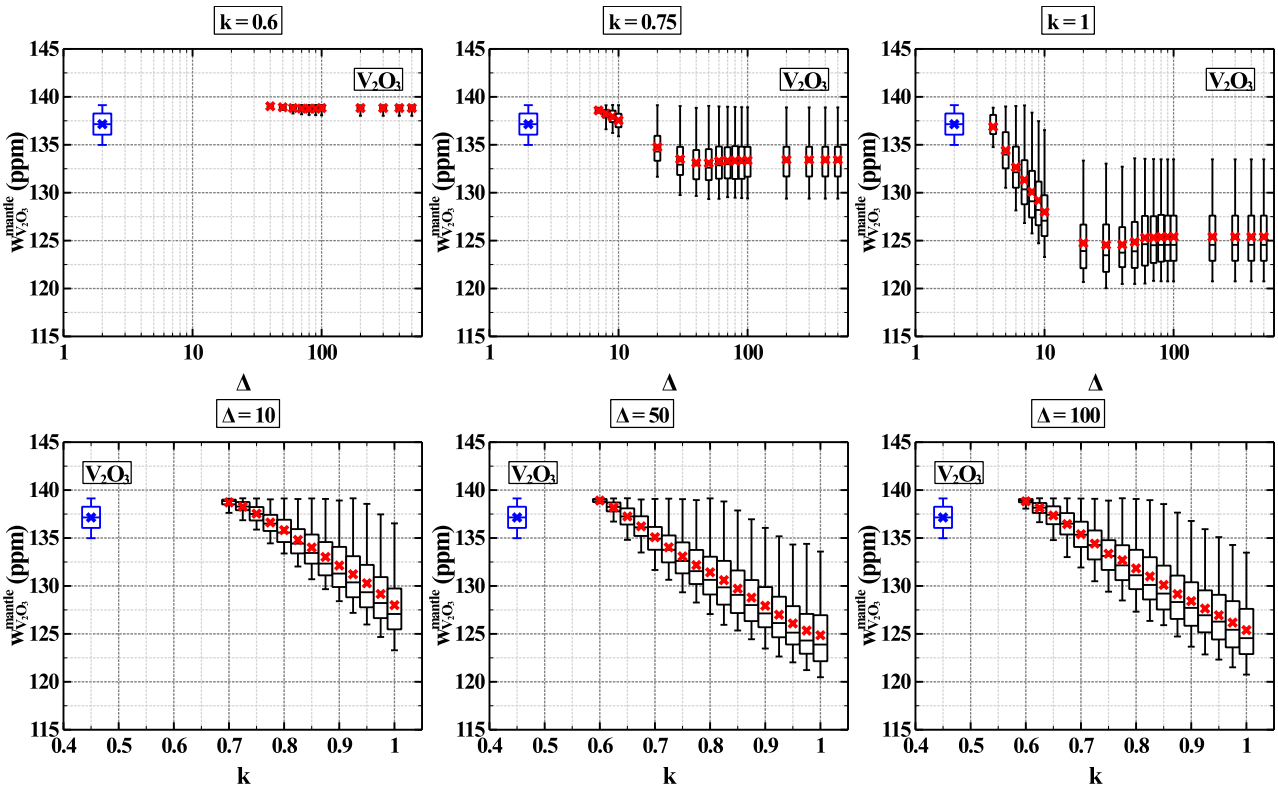

Figure S.25. Evolution of V_2O_3 concentrations (ppm) in the mantle as a function of Δ for fixed values of k (top row), and as a function of k for fixed values of Δ (bottom row). In each panel the entire solutions range are presented as boxplots, with the red cross being the mean value of the parameter, the white box delimiting the 1st and 3rd quartile, the horizontal line the median value and the vertical lines the minimum and maximum values. The reference model dataset is presented in blue with the same type of plot for comparison.

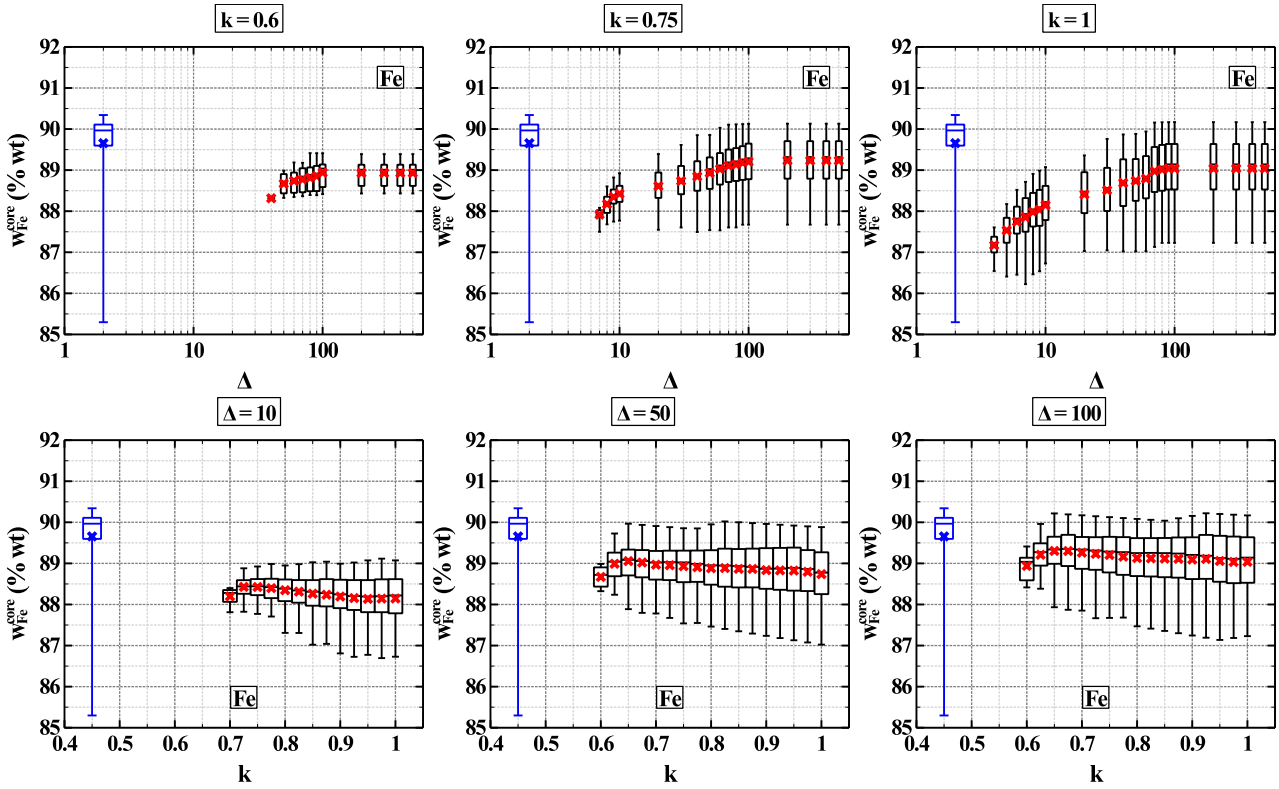

Figure S.26. Evolution of Fe concentrations (% wt) in the core as a function of Δ for fixed values of k (top row), and as a function of k for fixed values of Δ (bottom row). In each panel the entire solutions range are presented as boxplots, with the red cross being the mean value of the parameter, the white box delimiting the 1st and 3rd quartile, the horizontal line the median value and the vertical lines the minimum and maximum values. The reference model dataset is presented in blue with the same type of plot for comparison.

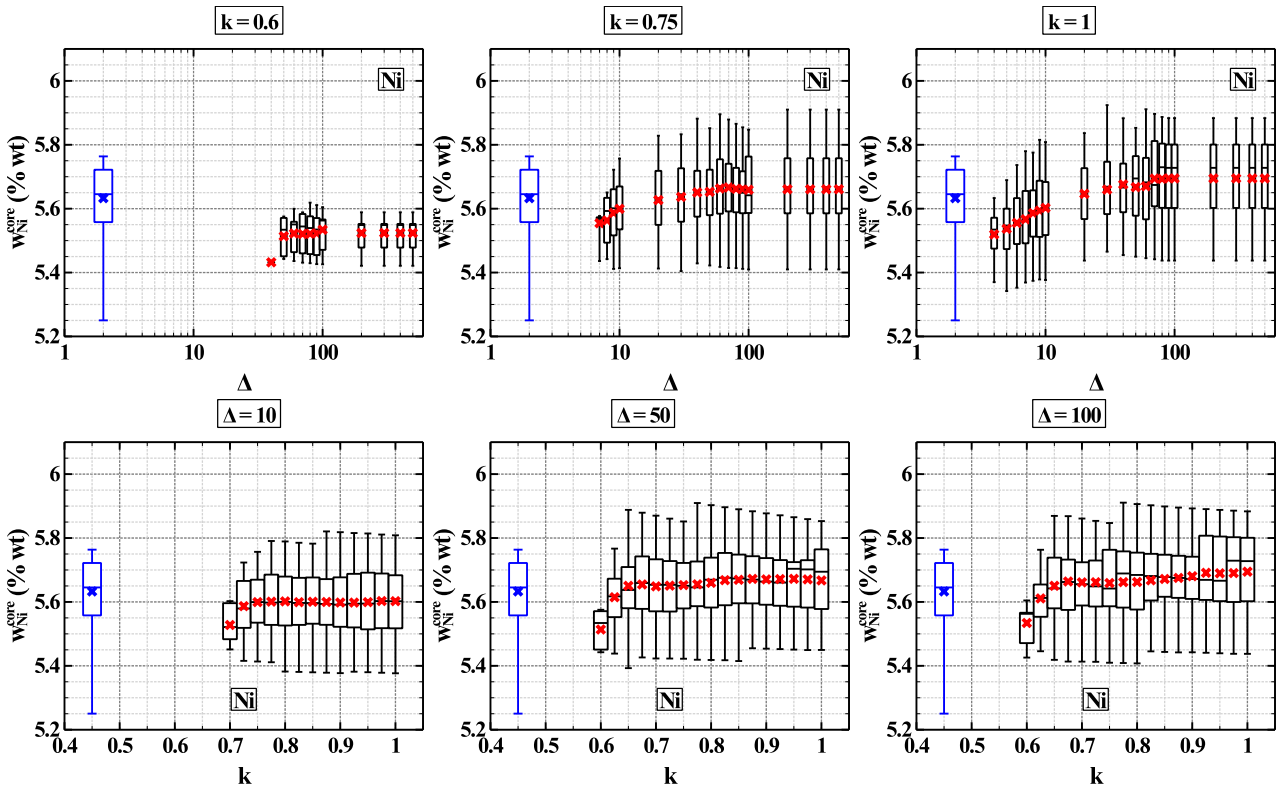

Figure S.27. Evolution of Ni concentrations (% wt) in the core as a function of Δ for fixed values of k (top row), and as a function of k for fixed values of Δ (bottom row). In each panel the entire solutions range are presented as boxplots, with the red cross being the mean value of the parameter, the white box delimiting the 1st and 3rd quartile, the horizontal line the median value and the vertical lines the minimum and maximum values. The reference model dataset is presented in blue with the same type of plot for comparison.

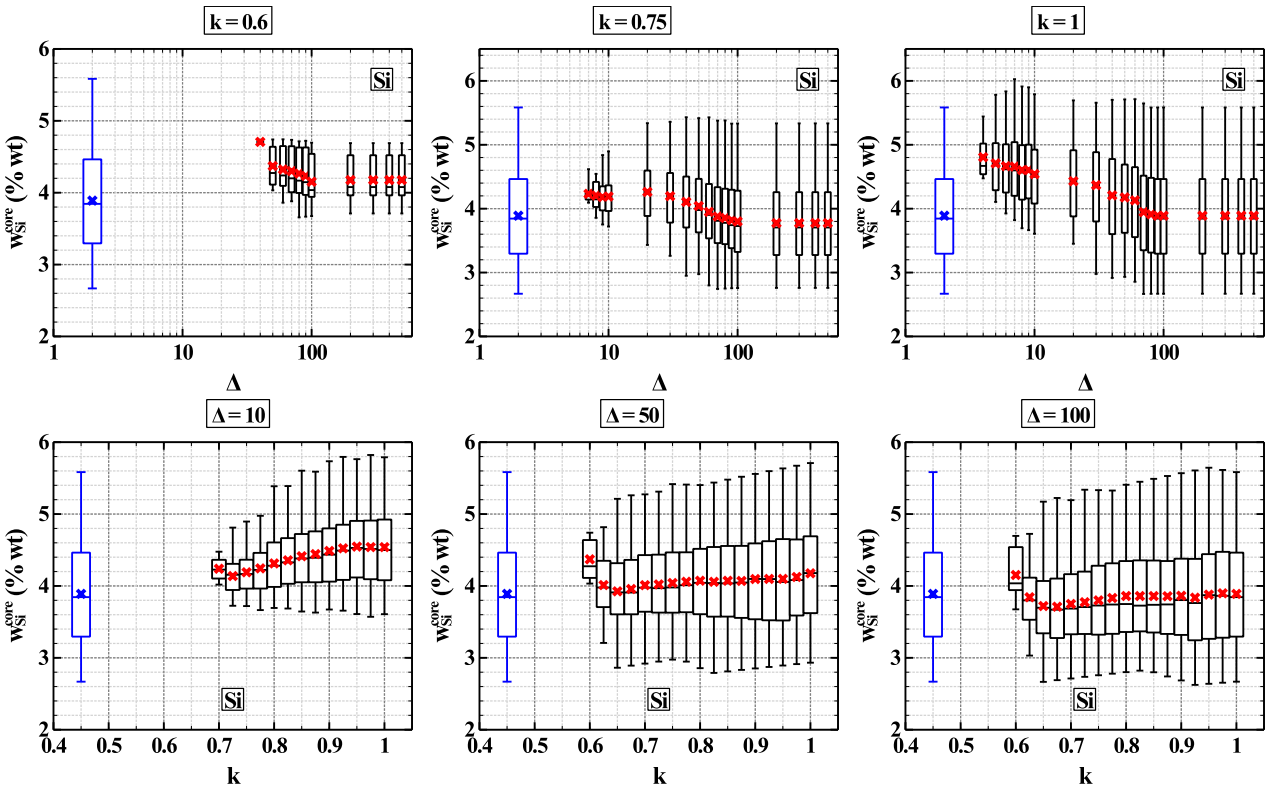

Figure S.28. Evolution of Si concentrations (% wt) in the core as a function of Δ for fixed values of k (top row), and as a function of k for fixed values of Δ (bottom row). In each panel the entire solutions range are presented as boxplots, with the red cross being the mean value of the parameter, the white box delimiting the 1st and 3rd quartile, the horizontal line the median value and the vertical lines the minimum and maximum values. The reference model dataset is presented in blue with the same type of plot for comparison.

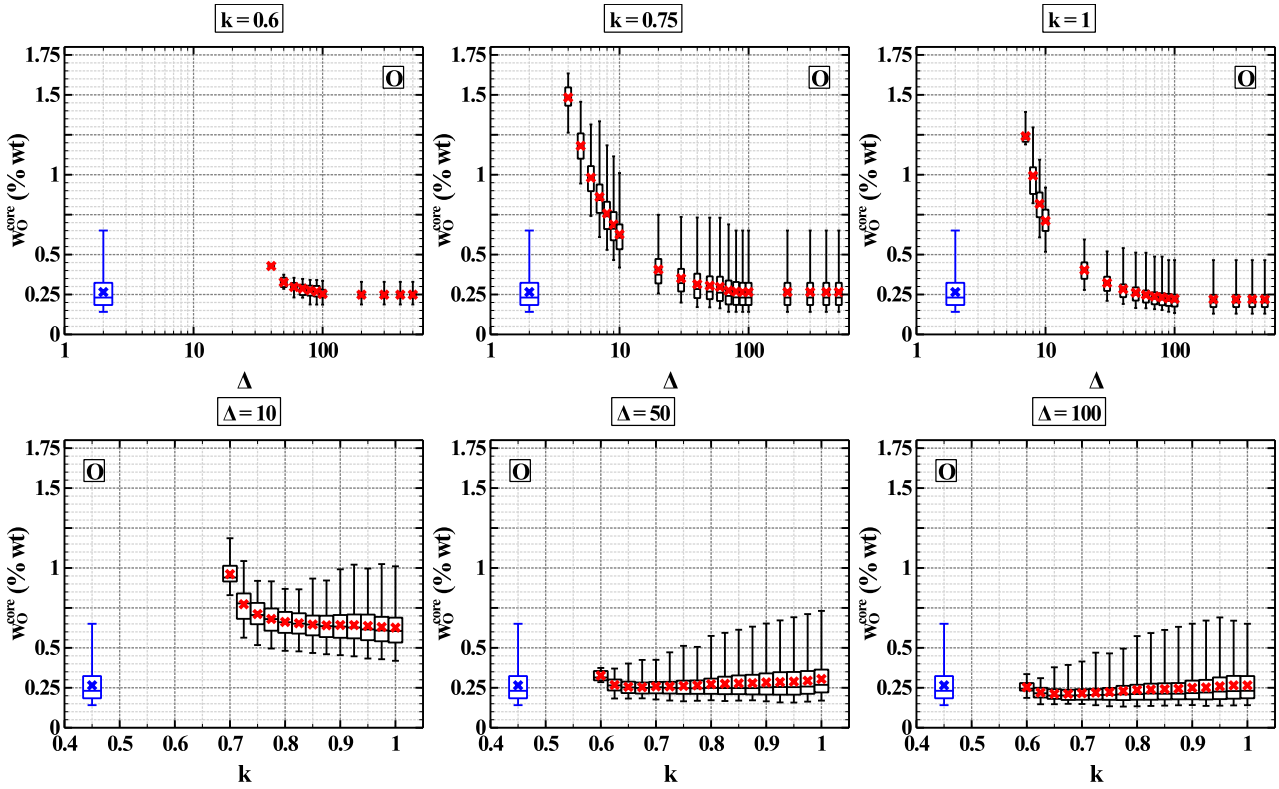

Figure S.29. Evolution of O concentrations (% wt) in the core as a function of Δ for fixed values of k (top row), and as a function of k for fixed values of Δ (bottom row). In each panel the entire solutions range are presented as boxplots, with the red cross being the mean value of the parameter, the white box delimiting the 1st and 3rd quartile, the horizontal line the median value and the vertical lines the minimum and maximum values. The reference model dataset is presented in blue with the same type of plot for comparison.

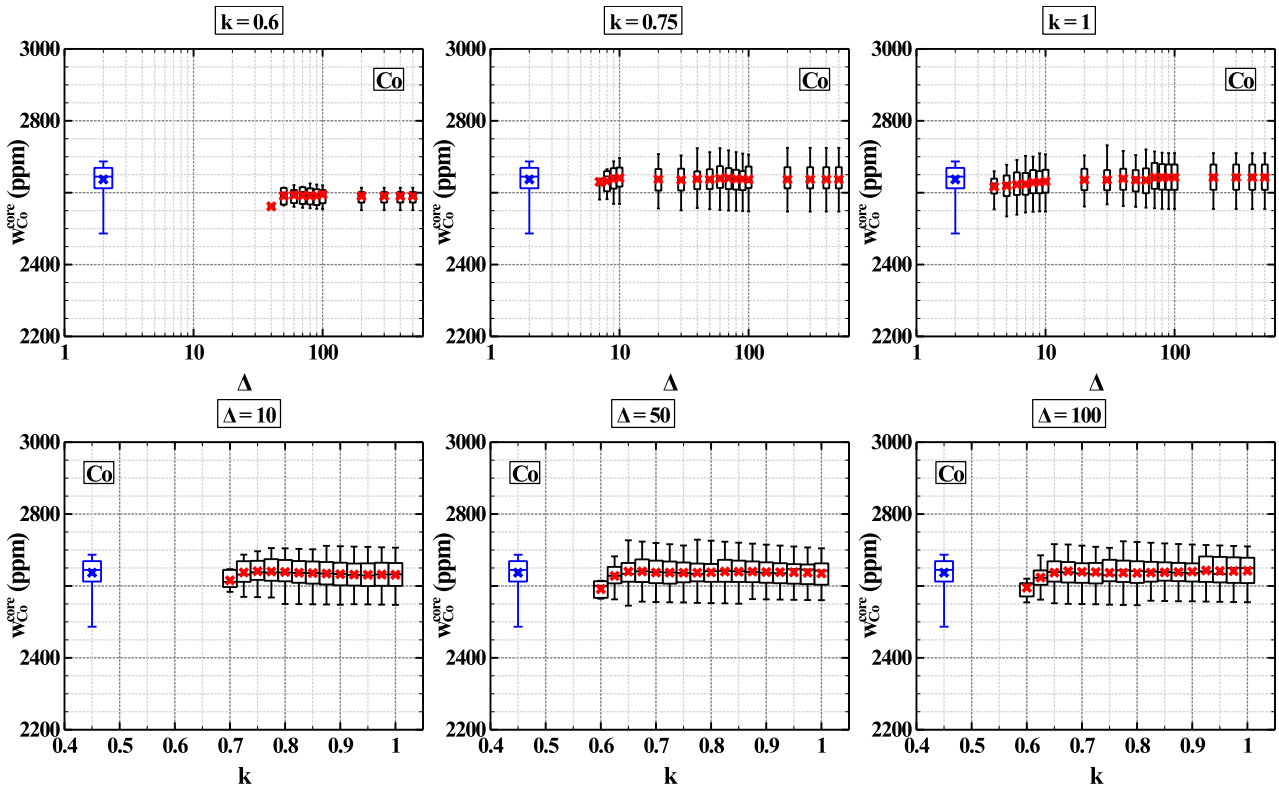

Figure S.30. Evolution of Co concentrations (ppm) in the core as a function of Δ for fixed values of k (top row), and as a function of k for fixed values of Δ (bottom row). In each panel the entire solutions range are presented as boxplots, with the red cross being the mean value of the parameter, the white box delimiting the 1st and 3rd quartile, the horizontal line the median value and the vertical lines the minimum and maximum values. The reference model dataset is presented in blue with the same type of plot for comparison.

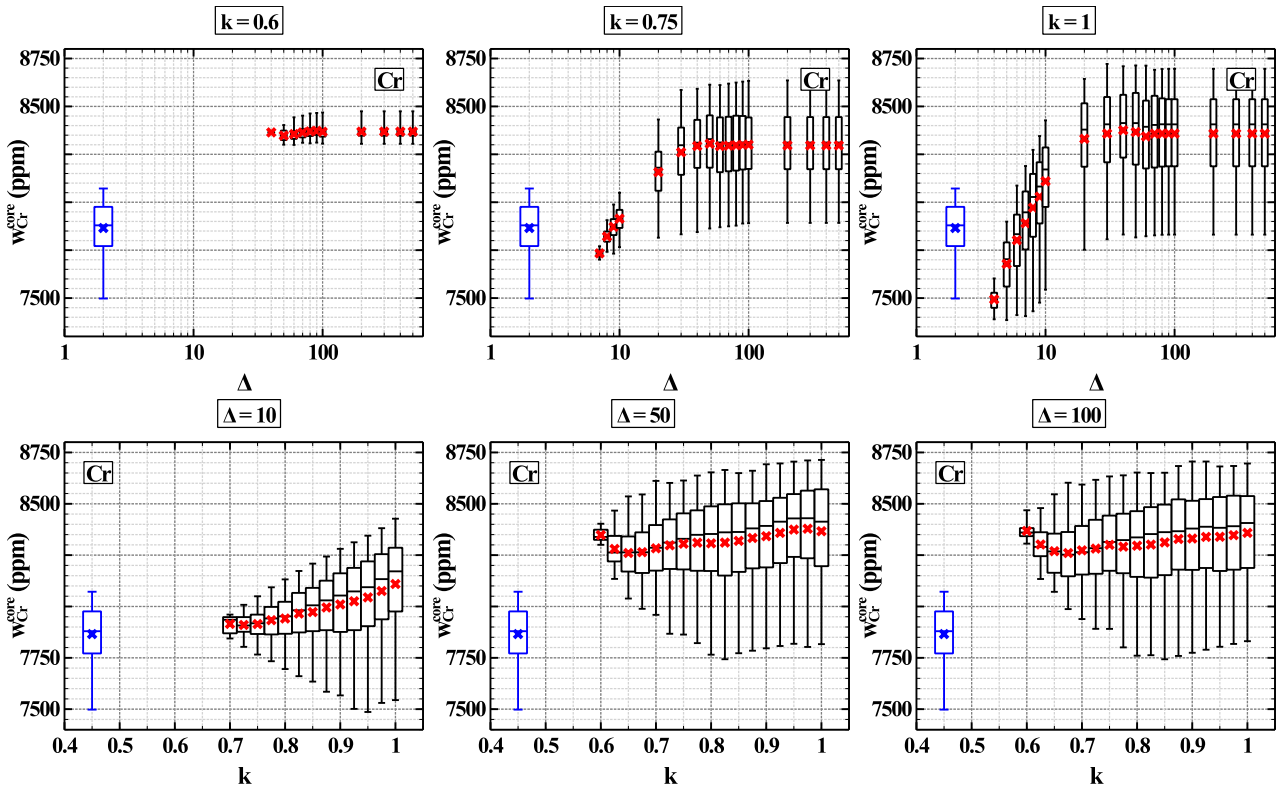

Figure S.31. Evolution of Cr concentrations (ppm) in the core as a function of Δ for fixed values of k (top row), and as a function of k for fixed values of Δ (bottom row). In each panel the entire solutions range are presented as boxplots, with the red cross being the mean value of the parameter, the white box delimiting the 1st and 3rd quartile, the horizontal line the median value and the vertical lines the minimum and maximum values. The reference model dataset is presented in blue with the same type of plot for comparison.

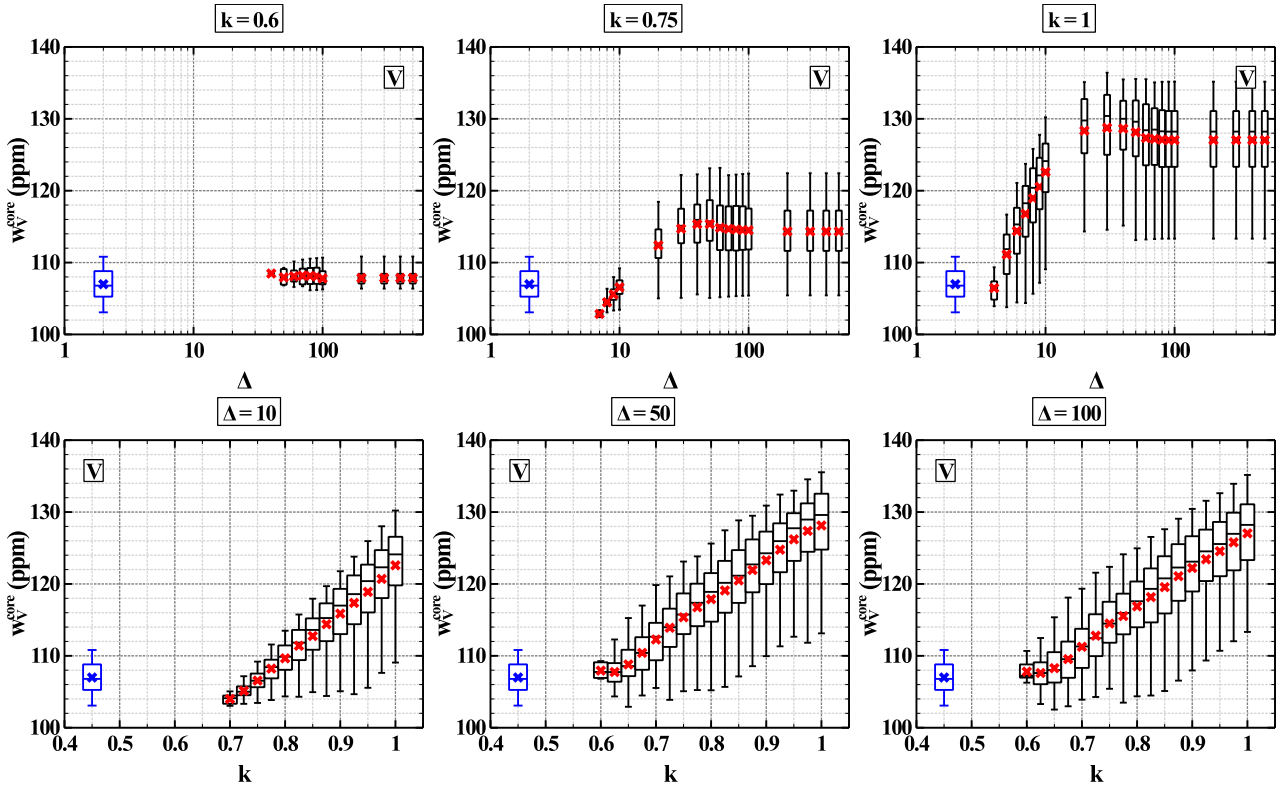

Figure S.32. Evolution of V concentrations (ppm) in the core as a function of Δ for fixed values of k (top row), and as a function of k for fixed values of Δ (bottom row). In each panel the entire solutions range are presented as boxplots, with the red cross being the mean value of the parameter, the white box delimiting the 1st and 3rd quartile, the horizontal line the median value and the vertical lines the minimum and maximum values. The reference model dataset is presented in blue with the same type of plot for comparison.